

AD A049084

18
REPORT NADC 76201-3p
19

12

6

AN EXPERIMENTAL AND ANALYTICAL INVESTIGATION OF
THE HOVERING AND FORWARD FLIGHT CHARACTERISTICS
OF THE AEROCRANE HYBRID HEAVY LIFT VEHICLE.

AD NO.

DDC FILE COPY

10

W. F. Putman
H. C. Curtiss, Jr.

Department of Aerospace and Mechanical Sciences
Princeton University
Princeton, N.J. 08540

11

Sep 1977

12 132p.

14 AMS-TR-1351

9 FINAL REPORT,

15 N62267-76-C-Q464

Approved for Public Release; Distribution Unlimited

16 F 41-411

17 WF 41-411-PPP

Prepared for:

Naval Air Development Center
Code 30P3
Warminster, Pa. 18974

DDC
RECEIVED
JAN 24 1978
D

288 475

mt

UNCLASSIFIED

SECURITY CLASSIFICATION OF THIS PAGE (When Data Entered)

REPORT DOCUMENTATION PAGE		READ INSTRUCTIONS BEFORE COMPLETING FORM
1. REPORT NUMBER NADC-76201-30 ✓	2. GOVT ACCESSION NO.	3. RECIPIENT'S CATALOG NUMBER
4. TITLE (and Subtitle) AN EXPERIMENTAL AND ANALYTICAL INVESTIGATION OF THE HOVERING AND FORWARD FLIGHT CHARACTERISTICS OF THE AEROCRANE HYBRID HEAVY LIFT VEHICLE		5. TYPE OF REPORT & PERIOD COVERED FINAL REPORT
7. AUTHOR(s) W. F. Putman H. C. Curtiss, Jr.		6. PERFORMING ORG. REPORT NUMBER AMS TR-1351 ✓
8. PERFORMING ORGANIZATION NAME AND ADDRESS Princeton University ✓ Department of Aerospace and Mechanical Sciences Princeton, N. J. 08540		9. CONTRACT OR GRANT NUMBER(s) N 62269-76-C-0464 <i>new</i>
11. CONTROLLING OFFICE NAME AND ADDRESS Naval Air Development Center ✓ Code 30P3 Warminster, PA 18974		10. PROGRAM ELEMENT, PROJECT, TASK AREA & WORK UNIT NUMBERS AIRTASK NO. A03P-03P3/001B/ 7WF41-411-000 Work Unit No. DH816
14. MONITORING AGENCY NAME & ADDRESS (if different from Controlling Office)		12. REPORT DATE September 1977
		13. NUMBER OF PAGES 121
		15. SECURITY CLASS. (of this report) UNCLASSIFIED
		15a. DECLASSIFICATION/DOWNGRADING SCHEDULE
16. DISTRIBUTION STATEMENT (of this Report) Approved for Public Release; Distribution Unlimited		
17. DISTRIBUTION STATEMENT (of the abstract entered in Block 20, if different from Report)		
18. SUPPLEMENTARY NOTES		
19. KEY WORDS (Continue on reverse side if necessary and identify by block number) AEROCRANE DYNAMIC STABILITY VTOL HEAVY LIFT HOVER HYBRID		
20. ABSTRACT (Continue on reverse side if necessary and identify by block number) Results of an analytical and experimental investigation of an AEROCRANE hybrid heavy lift vehicle are discussed. The experimental program involved free-flight investigations of the trim and dynamic stability characteristics of the AEROCRANE in hovering and forward flight using a Froude-scaled model. The effects of a simple feedback system on the dynamic stability of the model and the ability of a remote pilot to control the model are discussed. Analytical predictions of the model characteristics showed very good agreement with the experimental data.		

DD FORM 1 JAN 73 1473

EDITION OF 1 NOV 68 IS OBSOLETE
S/N 0102-LF-014-6601

UNCLASSIFIED

SECURITY CLASSIFICATION OF THIS PAGE (When Data Entered)



SUMMARY

This report discusses a combined analytical and experimental research program to evaluate the trim conditions and dynamic stability characteristics of a proposed AEROCRANE heavy lift vehicle in hovering and forward flight, using a free-flight Froude scale model.

Pursuant to the conclusions and recommendations of previous analytical and experimental hovering investigations reported in Reference 1, the model and model systems were revised and modified to allow safe and well-controlled experimental investigations in hover and forward flight. The principal modifications and revisions involved implementation of a stability augmentation system and provision for achieving a fully buoyant non-rotating state for flight safety.

Prior to actual flight testing a theoretical model for prediction of aircraft trim conditions in forward flight was developed. Linearized equations of motion for dynamic stability were extended to include forward flight, and the influence of a sling load as well as the umbilical cable associated with the free-flight model.

Hovering and forward flight experiments were conducted in Hangar No. 1 at the Naval Air Engineering Center, Lakehurst, N. J., and the data from these investigations were used to corroborate the analytical models for trim and dynamic stability. The results of this comparison indicate that the analytical models provide very good predictions of the trim and dynamic stability characteristics of the AEROCRANE model.

ACCESSION #	
DTIC	<input checked="" type="checkbox"/>
DOC	<input type="checkbox"/>
UNANNOUNCED	<input type="checkbox"/>
JUSTIFICATION	
BY	
DISTRIBUTION/AVAILABILITY CODES	
Doc.	AVAIL. AND/OR SPECIFIC
	

D D C
RECEIVED
JAN 24 1978
D

TABLE OF CONTENTS

	<u>Page</u>
LIST OF ILLUSTRATIONS.....	iii
NOMENCLATURE.....	v
INTRODUCTION.....	1
ANALYTICAL MODEL FOR TRIM AND DYNAMIC STABILITY.....	3
EXPERIMENTAL APPARATUS.....	41
EXPERIMENTAL FLIGHT TEST PROGRAM.....	46
COMPARISON OF ANALYSIS AND EXPERIMENT.....	50
CONCLUSIONS.....	55
REFERENCES.....	56
TABLES.....	57
FIGURES.....	60
APPENDIX A: Hovering Transient Response Data.....	82
APPENDIX B: Umbilical Cable Contributions to Dynamic Stability.....	91
APPENDIX C: Determination of AEROCRANE Model Physical Parameters and Numerical Results of Dynamic Stability Analysis.....	109
APPENDIX D: Modification of Trim Equations to Include Sling Load and Umbilical Cable.....	120

LIST OF ILLUSTRATIONS

<u>Figure</u>		<u>Page</u>
1	Axis Systems Used for Analytical Model.....	60
2	AEROCRANE Model with Jettisonable Ballast Package.....	64
3	General Arrangement Drawing of AEROCRANE Model.....	65
4	Schematic Drawing of Model Structural Modifications.....	66
5	Schematic of Attitude Stability Augmentation System.....	67
6	Schematic of Angular Rate Stability Augmentation System.....	68
7	AEROCRANE Model in Hovering Flight.....	69
8	Test Crew Arrangement.....	70
9	Hovering Transient Responses, Run No. 8	71
10	Arrangement of Test Apparatus for Forward Flight Experiments; Beginning of Run.....	72
11	Arrangement of Test Apparatus for Forward Flight Experiments; End of Run.....	73
12	Typical Transition Time History.....	74
13	Typical Forward Flight Transient Response Time Histories.	75
14	Trim Force Conditions, Comparison of Experiment and Theory: Sphere Drag	76
15	Trim Force Conditions, Comparison of Experiment and Theory: Magnus Lift Force.....	77
16	Trim Conditions, Comparison of Experiment and Theory: Longitudinal and Lateral Cyclic Pitch.....	78
17	Period and Damping of Hovering Retrograde Oscillation, Comparison of Theory and Experiment.....	79
18	Hovering Transient Response, Low Center of Gravity, Comparison of Theory and Experiment.....	80

<u>Figure</u>		<u>Page</u>
19	Hovering Transient Response, High Center of Gravity, Comparison of Theory and Experiment.....	81
A-1	Hovering Transient Responses, Run No. 10.....	83
A-2	Hovering Transient Responses, Run No. 11	84
A-3	Hovering Transient Responses, Run No. 15.....	85
A-4	Hovering Transient Responses, Run No. 17.....	86
A-5	Hovering Transient Responses, Run No. 36.....	87
A-6	Hovering Transient Responses, Run No. 52.....	88
B-1	Coordinates and Geometry for Cable Analysis.....	106
B-2	Approximations Used in Cable Dynamics.....	107
B-3	Umbilical Cable Geometry in Hovering.....	108
C-1	Numerical Values of Matrix Elements for Run No. 11	116
C-2	Numerical Values of Matrix Elements for Run No. 17	117
C-3	Numerical Values of Matrix Elements for Run No. 36	118
C-4	Numerical Values of Matrix Elements for Run No. 15	119

NOMENCLATURE

A	angle of attack rotation matrix
a	rotor blade lift curve slope, per rad.
\bar{a}	acceleration vector
A ₁₈	longitudinal cyclic pitch, referenced to gondola axes, deg or rad.
B	sideslip rotation matrix
b	number of blades, b = 4
B ₁₈	lateral cyclic pitch, referenced to gondola axes, deg or rad.
c	blade chord, ft, c = 2.3 ft.
C	damping matrix
C _D	drag coefficient of centerbody, $C_D = \frac{D}{\frac{1}{2} \rho V^2 \pi R_g^2}$
C _H	rotor in-plane force coefficient, $C_H = \frac{H}{\rho \pi R^2 (\Omega R)^2}$
C _L	rolling moment coefficient, $C_L = \frac{L}{\rho \pi R^2 (\Omega R)^2 R}$
C _{LM}	magnus force coefficient of centerbody, $C_{LM} = \frac{L_M}{\frac{1}{2} \rho V^2 \pi R_g^2}$
C _M	pitching moment coefficient, $C_M = \frac{M}{\rho \pi R^2 (\Omega R)^2 R}$
C _T	thrust coefficient, $C_T = \frac{T}{\rho \pi R^2 (\Omega R)^2}$
C _V	rotor lateral force coefficient, $C_V = \frac{Y}{\rho \pi R^2 (\Omega R)^2}$

D	sphere drag force, lbs.
F	control matrix
F_B	buoyant force, lbs.
F_M	Magnus force, lbs.
f_N	rotor radial station factors, $f_N = 1 - \chi^n$
H	rotor in-plane force, rotor axis system, positive to the rear, lb.
H_u, M_u	stability derivatives divided by m' and I' respectively
I'	vehicle moment of inertia about x_s and y_s axes, including apparent mass contribution, slug ft ²
I_z	vehicle moment of inertia about z_s axis, slug ft ²
J	proportionality constant between harmonic inflow and rotor aerodynamic moment
K	spring matrix
K_A	attitude feedback gain, rad/rad/ or deg/deg
L	rotor hub rolling moment, rotor axes, ft-lb.
L_s	total rolling moment, shaft axes, positive right side down, ft-lb.
m'	sum of mass of vehicle and apparent mass, slugs
m_A	apparent mass of vehicle, calculated for centerbody only, slugs
m_{ce}	effective mass of umbilical cable, slugs
m_L	sling load mass, slugs
m_o	vehicle mass, slugs
M_s	total pitching moment, shaft axes, positive nose up, ft-lb.

M	rotor hub pitching moment, rotor axes, ft-lb., mass matrix
\bar{P}_A	load attachment point position vector
\bar{P}_L	load center of gravity position vector
p	roll rate, positive right side down, rad/sec
q	pitch rate, positive nose up, rad/sec
r_o	distance between center of buoyancy and center of gravity, positive for center of gravity below center of buoyancy, ft.
R	rotor radius, ft.
\bar{R}	load reaction force vector
R_s	centerbody radius, ft.
s	Laplace operator
SAS	stability augmentation system
t	time
T	rotor thrust, rotor axis system, positive up, lbs.
U_o	horizontal velocity (along x_o axis), positive forward, ft/sec.
u	component velocity along x axis, ft/sec.
\bar{V}	velocity vector
V	trim flight velocity, fps, $V = \sqrt{U_o^2 + W_o^2}$
v	component velocity along y axis, or induced velocity, ft/sec.
\bar{V}	volume of centerbody, ft ³
w	component of velocity along z axis, ft/sec.
W	total lifted weight of model including sling load and umbilical cable weight, lb, $W = W_o + W_{sl} + W_c$
W_o	vertical velocity (along z_o axis), positive downward, or model weight, lbs.

X	rotor wake angle measured from vertical, column vector
Y	rotor side force, rotor axis system, positive right
Y_s	lateral force, body axes, positive to right, lb.
Z_A	distance from load attachment point to vehicle center of gravity, ft.
α	rotor angle-of-attack
β	gondola sideslip angle, positive for vehicle motion to the right
γ	phase angle for stability augmentation, positive clockwise from top
θ	rotor blade pitch angle. Referenced to wind axes, $\theta = \theta_0 - A_{1W} \cos \psi_R - B_{1W} \sin \psi_R .$ Referenced to gondola axes, $\theta = \theta_0 - A_{1s} \cos \psi_s - B_{1s} \sin \psi_s$
θ	vehicle pitch angle, positive nose up, rad
θ_0	rotor collective pitch, rad
Θ	pitch rotation matrix
λ_s	rotor inflow ratio, positive for flow up through rotor
λ_s	cosine component of dimensionless induced velocity due to blow back, $\lambda_s = \lambda_1 x$
λ_m, λ_l	harmonic inflow components due to rotor aerodynamic pitching and rolling moments, $\lambda_m = j \frac{2C_m}{a \sigma}, \lambda_l = -j \frac{2C_l}{a \sigma}$
λ_1	rate of change of cosine component of induced velocity with radius due to "blow back", dimensionless

μ	rotor advance ratio
ρ	density of air, slugs/ft ³
σ	rotor solidity $\sigma = \frac{bc}{\pi R}$
ϕ	vehicle roll angle, positive right side down, rad
Φ	roll rotation matrix
ψ	blade azimuth angle, ψ_s is measured from downwind, ψ_g is measured from gondola reference axes, positive in direction of rotor rotation, or yaw rotation matrix
ω_n	nutation frequency, $\omega_n = \frac{I_z}{I'} \Omega$, rad/sec
ω_p^2	square of pendulous frequency, $\omega_p^2 = \frac{F_s r_o}{I'}$, rad ² /sec ²
ω_{sl}	uncoupled sling load pendulous frequency, $\omega_{sl} = \sqrt{\frac{g}{Z_L}}$, rad/sec
Ω	rotor/centerbody angular velocity, RPM or rad/sec
χ	ratio of centerbody radius to rotor radius, $\chi = \frac{R_s}{R}$

Subscripts

() _A	referenced to attachment axis system
() _B	referenced to body axis system
() _G	referenced to gravity axis system
() _R	referenced to rotor axis system
() _S	referenced to shaft axis system
() _W	referenced to wind axis system
([.])	differentiation with respect to time
()', ()''	intermediate axis systems

INTRODUCTION

This report presents the results of a combined analytical and experimental research effort to investigate the dynamic stability and trim characteristics of a Froude scale model of the AEROCRANE heavy lift vehicle. The research described herein is intended to quantify the aircraft's transfer functions to control inputs and its trim conditions in hovering and forward flight operation in still air.

An analytical and experimental investigation of the hovering dynamics of a 0.1 Froude scale model was conducted and reported in Reference 1. During these investigations it was determined that the model exhibited a lightly damped retrograde precessional motion, that under certain conditions of rotor thrust and center of gravity positions, could become unstable. Although piloted analog simulations indicated that with proper motion cues a pilot could stabilize this mode with a reasonable level of effort, it was also demonstrated that a remote pilot, with inadequate motion cues, would have great difficulty in controlling the model. Theoretical investigations considering a coupled four-degree-of-freedom hovering analytical model showed that a relatively simple azimuthally-phased attitude feedback would readily stabilize this mode at very low levels of feedback gain. Accordingly it was recommended in Reference 1 that such a feedback control system be incorporated in the model control system for future experimental investigations.

It was further recommended in Reference 1 that the analytical model of the vehicle be extended to include forward flight. It was considered that this extension of the analytical model would provide insight into

the dynamic behavior of the vehicle in forward flight that would be valuable in planning and conducting forward flight experiments with the model. This extended analytical model would also provide the basis for corroboration of both hover and forward flight experimental results in quantifying the vehicle transfer functions to control inputs.

Finally, it was concluded in Reference 1 that certain aspects of the model and model control system could be modified to increase the safety of experimental flight operations. In particular it was deemed advisable to incorporate a means for rapidly achieving a buoyant state at any flight condition and simultaneously arresting the model's rotational motion so as to lessen the probability of model damage in the event of model control or power loss, etc.

The research efforts reported herein incorporated the above-cited recommendations and implemented the conclusions of Reference 1 by measuring the hover and forward flight trim and dynamic stability characteristics of the AEROCRANE heavy lift vehicle using a Froude scale dynamic model in free-flight. The experimental results are compared with the results obtained from the analytical model.

ANALYTICAL MODEL FOR TRIM AND DYNAMIC STABILITY

This section presents the analytical model to predict the forward flight trim conditions and the dynamic response characteristics of the AEROCRANE. The formulation is complicated by the fact that the rotating centerbody produces lateral force owing to the Magnus effect, and thus forward flight trim involves a vehicle roll angle as well as a pitch angle. Further, owing to the comparatively large drag and Magnus force developed by the centerbody, the trim roll and pitch angles are relatively large and consequently small angle assumptions are not made. In order to make the presentation more compact the development is presented in matrix notation and then expanded to produce the trim equations. The dynamic response equations are obtained by a perturbation analysis about the trim condition. The perturbations are assumed to be small angles; however, the large angle formulation is retained for the trim or equilibrium condition.

I. TRIM ANALYSIS

1.) Axis Systems

The following axis systems are defined:

a.) Gravity Axis Systems, X_g (x_g, y_g, z_g)

This axis system is oriented such that z_g is parallel to the local gravity vector and points downward. x_g points forward in the direction of flight of the vehicle. The flight velocity of the vehicle lies in the plane of x_g, z_g and in general is composed of a horizontal velocity U_0 along the x_g axis and a vertical velocity W_0 along the z_g axis. Thus U_0 and W_0 describe the velocity of the vehicle with respect to the earth.

b.) Gondola or Body Axes, $X_g (x_g, y_g, z_g)$

This axis system is aligned with the body or gondola of the vehicle. The body axis x_g lies along the longitudinal axis of the gondola pointing forward, and the axis z_g lies along the shaft or vehicle axis of rotation. The orientation of this axis system with respect to the gravity axis system is given by three rotations; θ , the body pitch angle; ϕ , the body roll angle; and ψ , the body yaw angle. These rotations are performed in the following order: ϕ is a rotation about the x_g axis; θ is the second rotation performed about the deflected y axis (y'), and ψ is then rotation about the further deflected z axis (z''). The cyclic control is referenced with respect to the orientation of the body or gondola axis system, i.e., the azimuth angle for cyclic is measured with respect to the negative x_g axis and is positive in the direction of rotor rotation.

c.) Rotor Axis System, $X_R (x_R, y_R, z_R)$

This axis system is employed in the derivation of the rotor forces and moments. The z_R axis lies along the rotor shaft or axis of rotation and the x_R axis lies in the plane of the relative wind. The orientation of this axis system is obtained by rotation of the body axis system, X_g , about the z_g axis by the sideslip angle, β such that the x_R axis lies in the plane of the relative wind. That is, by definition in this axis system, the velocity component along the y_R axis is equal to zero in equilibrium flight. In the derivation of rotor forces and moments, the azimuth angle is measured with respect to the negative x_R direction, positive in the direction of rotor rotation.

d.) Wind Axis System, $X_w (x_w, y_w, z_w)$

The centerbody drag and Magnus forces are defined in this axis system. The x_w axis points in the direction of the relative wind. The orientation of this axis system is obtained by rotation of the rotor axis system, X_r , about the y_r axis by the angle-of-attack, α , such that x_w points into the relative wind. That is, by definition the resultant flight velocity is along x_w and the velocity components along the y_w and z_w axes are zero.

e.) Shaft Axis System, $X_s (x_s, y_s, z_s)$

One further axis system is employed for force and moment resolution and this is referred to as a shaft axis system, which involves only rotation of the gravity axis system through the first two rotations, ϕ , the vehicle roll angle and, θ , the vehicle pitch angle. This is convenient owing to the fact that the two rotations, the body or gondola yaw angle, ψ , and sideslip angle, β , will appear as a sum.

These then are the five axis systems employed in the development. They are shown schematically in Figure 1. To proceed with the development we employ the following compact notation. The symbol X with a subscript refers to a particular axis system as well as the three components of any vector defined with respect to the particular axis system, for example, the three velocity components in that system or the forces or moments with respect to that axis system. Further, the various rotation matrices are denoted by single symbols,

$$\begin{array}{l} \text{roll} \\ \Phi = \end{array} \begin{bmatrix} 1 & 0 & 0 \\ 0 & \cos \phi & \sin \phi \\ 0 & -\sin \phi & \cos \phi \end{bmatrix}$$

$$\begin{array}{l} \text{pitch} \\ \Theta = \end{array} \begin{bmatrix} \cos \theta & 0 & -\sin \theta \\ 0 & 1 & 0 \\ \sin \theta & 0 & \cos \theta \end{bmatrix}$$

(1)

$$\begin{array}{l} \text{yaw} \\ \Psi = \end{array} \begin{bmatrix} \cos \psi & \sin \psi & 0 \\ -\sin \psi & \cos \psi & 0 \\ 0 & 0 & 1 \end{bmatrix}$$

$$\begin{array}{l} \text{sideslip} \\ B = \end{array} \begin{bmatrix} \cos \beta & \sin \beta & 0 \\ -\sin \beta & \cos \beta & 0 \\ 0 & 0 & 1 \end{bmatrix}$$

$$\begin{array}{l} \text{angle-of-attack} \\ A = \end{array} \begin{bmatrix} \cos \alpha & 0 & \sin \alpha \\ 0 & 1 & 0 \\ -\sin \alpha & 0 & \cos \alpha \end{bmatrix}$$

Note also that since all of these matrices correspond to rotations, the inverse of any of these matrices is equal to the transpose of the matrix. Further it may be noted that when the matrix product $B\psi$ appears it can be expressed as

$$B\psi = \begin{bmatrix} \cos(\beta + \psi) & \sin(\beta + \psi) & 0 \\ -\sin(\beta + \psi) & \cos(\beta + \psi) & 0 \\ 0 & 1 & 1 \end{bmatrix} \quad (2)$$

thus $B\psi$ is a function of $(\beta + \psi)$ only.

Transformations among the various axes are given by

$$\begin{aligned} X_g &= \psi \oplus X_a \\ X_n &= B X_g \\ X_w &= A X_n \\ X_s &= \Theta \oplus X_a \end{aligned} \quad (3)$$

2.) Forces

The various forces acting on the vehicle are defined in various of these axis systems as follows:

a.) Gravity and Buoyant Forces

The weight of the vehicle, W , acts in the positive z_a direction at the center of gravity of the vehicle, and the buoyant force, F_b , acts in the negative z_a direction at the center of buoyancy of the vehicle. Thus the vector of forces produced by gravity and buoyancy is,

$$X_a = \begin{pmatrix} 0 \\ 0 \\ W - F_b \end{pmatrix} \quad (4)$$

b.) Rotor Forces

The rotor produces aerodynamic forces consisting of thrust, T , in-plane force H , and side force, Y , defined with respect to the rotor axis system (X_n). The thrust is positive in the negative z_n direction, the in-plane

force is positive in the negative x_r direction, and the side force is positive in the positive y_r direction. These forces act at the rotor hub. Thus the vector of forces produced by the rotor is,

$$X_r = \begin{pmatrix} -H \\ Y \\ -T \end{pmatrix} \quad (5)$$

c.) Centerbody Forces

The influence of forward speed in combination with centerbody rotation produces a drag force and a magnus force which are defined in the wind axis system (X_w). The drag force, D , is defined as positive in the negative x_w direction and the magnus force, F_m , is defined as positive in the positive y_w direction. These forces are assumed to act at the center of the centerbody. The vector of forces produced by the centerbody is thus

$$X_w = \begin{pmatrix} -D \\ F_m \\ 0 \end{pmatrix} \quad (6)$$

It is assumed that the gondola produces no aerodynamic forces owing to its small size.

The contributions of these forces can be summed to determine the resultant force acting on the vehicle. In matrix notation summing forces in the direction of the shaft axes, the three force equilibrium equations are, using the transformation relationships given by equation (3),

$$X_s = (ABV)^T X_w + (BV)^T X_R + G_s X_g \quad (7)$$

The first term represents the centerbody forces, the second term the rotor forces, and the third term the gravity and buoyancy forces. Equilibrium flight is given by the condition $X_s = 0$. Equation (7) can be expanded using the rotation matrices given by equation (1) and (2) and the forces given by equations (4), (5) and (6) to yield,

$$\begin{aligned} & (-W + F_g) \sin \theta \cos \phi - H \cos (\beta + \psi) - D \cos (\beta + \psi) \cos \alpha \\ & - (Y + F_R) \sin (\beta + \psi) = 0 \\ & (W - F_g) \sin \phi - H \sin (\beta + \psi) - D \sin (\beta + \psi) \cos \alpha \\ & + (Y + F_R) \cos (\beta + \psi) = 0 \\ & (W - F_g) \cos \theta \cos \phi - T - D \sin \alpha = 0 \end{aligned} \quad (8)$$

3.) Moments

The rotor is the only component of the vehicle assumed to produce direct moments. The rotor produces a rolling moment, L , which acts about the positive x_R axis and is thus a vector in the positive x_R direction. Similarly the rotor pitching moment M is represented by a vector in the positive y_R direction. Thus the rotor moments expressed as a vector are

$$\tilde{L}_R = \begin{pmatrix} L \\ M \\ 0 \end{pmatrix} \quad (9)$$

Since the rotor is propelled by tip propulsion the net rotor torque is zero. It is assumed that the rotor RPM is constant and consequently the balance of yawing moments is not considered further.

Moments are taken about the center of gravity of the vehicle which is assumed to lie on the axis of rotation a distance r_o below the rotor hub. It is also assumed as noted above that the center of buoyancy is coincident with the rotor hub and that the drag and magnus forces act at the center of the centerbody. Thus taking moments in the shaft system

$$\bar{L}_s = (\beta + \psi)^T \bar{L}_R + \bar{H} \times \bar{X}_s^* \quad (10)$$

X_s^* includes all of the forces acting at the rotor hub and consequently includes all of the forces contained in X_s with the exception of the gravity force. The vector \bar{H} is defined in the shaft axis system

$$\bar{H} = -r_o \bar{k}_s$$

where \bar{k}_s is a unit vector along the z_s axis.

In vector form

$$\bar{X}_s^* = \begin{pmatrix} X_s^* \bar{i}_s \\ Y_s^* \bar{j}_s \\ Z_s^* \bar{k}_s \end{pmatrix} \quad (11)$$

Consequently

$$\bar{H} \times \bar{X}_s^* = \begin{pmatrix} r_o Y_s^* \bar{i}_s \\ -r_o X_s^* \bar{j}_s \\ 0 \end{pmatrix} \quad (12)$$

Therefore the summation of moments using relationships (9), (10) and (12) is

$$\Sigma L_s = L \cos (\beta + \psi) - M \sin (\beta + \psi) + r_o Y_s^* \quad (13)$$

$$\Sigma M_s = L \sin (\beta + \psi) + M \cos (\beta + \psi) - r_o X_s^*$$

where from equations (8)

$$X_S^* = F_g \sin \theta \cos \phi - H \cos (\beta + \psi) - D \cos (\beta + \psi) \cos \alpha - (Y + F_M) \sin (\beta + \psi) \quad (14)$$

$$Y_S^* = -F_g \sin \phi - H \sin (\beta + \psi) - D \sin (\beta + \psi) \cos \alpha + (Y + F_M) \cos (\beta + \psi) \quad (15)$$

Moment equilibrium in trimmed flight is given by $\Sigma L_S = 0$, $\Sigma M_S = 0$ which can be expanded using equations (13) and (14) as

$$L \cos (\beta + \psi) - M \sin (\beta + \psi) + r_O \{-F_g \sin \phi - H \sin (\beta + \psi) - D \sin (\beta + \psi) \cos \alpha + (Y + F_M) \cos (\beta + \psi)\} = 0 \quad (16)$$

$$L \sin (\beta + \psi) + M \cos (\beta + \psi) + r_O \{-F_g \sin \theta \cos \phi + H \cos (\beta + \psi) + D \cos (\beta + \psi) \cos \alpha + (Y + F_M) \sin (\beta + \psi)\} = 0$$

These equations may be written in a somewhat simpler form using the force equilibrium conditions ($X_S = 0$, $Y_S = 0$) as

$$X_S^* = W \sin \theta \cos \phi \quad (17)$$

$$Y_S^* = -W \sin \phi$$

Equations (16) take the somewhat simpler form

$$L \cos (\beta + \psi) - M \sin (\beta + \psi) - r_O W \sin \phi = 0$$

$$L \sin (\beta + \psi) + M \cos (\beta + \psi) - r_O W \sin \theta \cos \phi = 0 \quad (18)$$

Thus the trim conditions of the vehicle are given by solution of equations (8) taken either with equations (16) or (18). To solve the trim problem

the forces and moments appearing in these equations must now be related to the flight velocity and control positions. The initial flight condition is specified in terms of horizontal and vertical flight velocities with respect to the earth, and the gondola yaw angle with respect to this flight path and then the five equilibrium equations given above are solved to determine the equilibrium values of the pitch attitude, roll attitude, collective pitch and cyclic pitch from these five equations. The sixth equation, the yawing moment equations has not been included since it would be used to determine the power required. It is assumed in the trim calculation that the rotor RPM is known.

4.) Velocity Components

First, the velocity components must be expressed in various axis systems. The flight condition is specified in the gravity axis system by the horizontal velocity U_0 and the vertical velocity W_0 , thus the vector of velocity components in the gravity axis system is

$$V_g = \begin{pmatrix} U_0 \\ 0 \\ W_0 \end{pmatrix} \quad (19)$$

The transformations given by equations (3) are employed to find the velocity components in various axis systems.

$$\begin{aligned} V_B &= Y \Theta \Phi V_g \\ V_R &= B V_B \\ V_W &= A V_R \\ V_S &= \Theta \Phi V_g \end{aligned} \quad (20)$$

The sideslip angle is defined by the fact that the velocity component v_R is equal to zero, i.e.,

$$V_R = \begin{pmatrix} u_R \\ 0 \\ w_R \end{pmatrix} \quad (21)$$

The angle-of-attack is defined by the fact that the velocity components v_W and w_W are equal to zero, i.e.,

$$V_W = \begin{pmatrix} V \\ 0 \\ 0 \end{pmatrix} \quad (22)$$

where V is the resultant flight velocity. From equation (20)

$$V_R = B \Psi \Theta \Phi V_0 \quad (23)$$

Expanding equation (23) the following results are obtained for the velocity components in the rotor axis system, expressed in terms of the horizontal and vertical velocity, U_0 and W_0 .

$$\begin{aligned} u_R &= U_0 \cos (\beta + \psi) \cos \theta + W_0 \{- \cos (\beta + \psi) \sin \theta \cos \phi \\ &\quad + \sin (\beta + \psi) \sin \phi\} \\ v_R &= - U_0 \sin (\beta + \psi) \cos \theta + W_0 \{\sin (\beta + \psi) \sin \theta \cos \phi \\ &\quad + \cos (\beta + \psi) \sin \phi\} \end{aligned} \quad (24)$$

$$w_R = U_0 \sin \theta + W_0 \cos \theta \cos \phi$$

The sideslip angle is determined from the condition that $v_n = 0$, so that the following relationship exists

$$- U_0 \sin (\beta + \psi) \cos \theta + W_0 \{ \sin (\beta + \psi) \sin \theta \cos \phi + \cos (\beta + \psi) \sin \phi \} = 0 \quad (25)$$

In the case of level flight ($W_0 = 0$) this relationship simplifies to

$$U_0 \sin (\beta + \psi) \cos \theta = 0 \quad (26)$$

and therefore in level flight,

$$\beta = - \psi \quad (27)$$

In general, equation (25) must be included with the trim conditions to determine the sideslip angle. Once the sideslip angle is determined, the angle-of-attack is given by the condition

$$\alpha = \tan^{-1} \frac{w_R}{u_R} \quad (28)$$

where w_R and u_R are determined by equations (24). Again in the level flight case ($W_0 = 0$), using equation (27), the following relationship exists

$$\alpha = \theta \quad (29)$$

The magnitude of the velocity in various axis systems is given by

$$V = \sqrt{U_0^2 + W_0^2} = \sqrt{u_R^2 + w_R^2}$$

5.) Cyclic Pitch

The expressions for the rotor forces and moments are developed in a wind axis system and consequently the cyclic pitch included in these equations is

referenced to the azimuth angle measured from the negative x_R axis called ψ_R . The physical system on the vehicle uses the negative direction of longitudinal gondola or body axis, x_S , as a reference. This azimuth angle is denoted ψ_S . Therefore

$$\psi_S = \psi_R + \beta \quad (30)$$

The rotor or wind referenced cyclic is therefore

$$\Delta\theta = -A_{1W} \cos \psi_R - B_{1W} \sin \psi_R \quad (31)$$

The physical or shaft referenced cyclic is therefore

$$\Delta\theta = -A_{1S} \cos \psi_S - B_{1S} \sin \psi_S \quad (32)$$

Substituting equation (30) and (31)

$$\begin{aligned} \Delta\theta = & -[A_{1W} \cos \beta - B_{1W} \sin \beta] \cos \psi_S \\ & - [B_{1W} \cos \beta + A_{1W} \sin \beta] \sin \psi_S \end{aligned} \quad (33)$$

Therefore the relationships between the actual cyclic pitch controls of the vehicle A_{1S} and B_{1S} and the wind referenced controls appearing in the rotor equations are

$$\begin{aligned} A_{1S} &= A_{1W} \cos \beta - B_{1W} \sin \beta \\ B_{1S} &= B_{1W} \cos \beta + A_{1W} \sin \beta \end{aligned} \quad (34)$$

In particular these equations must be noted when calculating stability derivatives.

6.) Analytical Models For Forces and Moments

The expressions for the various forces and moments described above

must now be expressed in terms of the various flight condition variables.

a.) Gravity and Buoyant Forces

The weight, W , is the weight of the vehicle including the weight of the helium in the centerbody. The buoyant force, F_b , is equal to the density of the air times the displaced volume

$$F_b = \rho g V \quad (35)$$

b.) Rotor Forces

A detailed derivation of the rotor forces is given in Reference 1. They are based on the assumption that the rotor blades do not flap and can be assumed to be infinitely rigid. The rigidity of the rotor is accounted for in the aerodynamic model by assuming that harmonic inflow components λ_L and λ_M are developed proportional to the aerodynamic hub moments developed by the rotor such that

$$\begin{aligned} \lambda_M &= j \frac{2C_M}{a\sigma} \\ \lambda_L &= j \frac{2C_L}{a\sigma} \end{aligned} \quad (36)$$

Further an harmonic component of the rotor inflow arises from the "blow back" of the wake. The magnitude of this effect is taken to be twice that given in Reference 2.

$$\lambda_1 = -2 \frac{V}{\Omega R} \tan \frac{X}{2} \quad (37)$$

where

$$X = \tan^{-1} \left(\frac{\mu_s}{-\lambda_s} \right) \quad (38)$$

Twice the value given in Reference 2 was chosen for reasons discussed in Reference 1.

The total rotor inflow is given by

$$\lambda = \lambda_s - (\lambda_1 + \lambda_M) \cos \psi_R - \lambda_L \sin \psi_R \quad (39)$$

where

$$\lambda_s = \frac{w_R - v}{\Omega R}$$

and the rotor induced velocity is given by momentum theory (Ref. 3)

$$v = \frac{C_T}{2f_s \sqrt{\left(\frac{w_R - v}{\Omega R}\right)^2 + \left(\frac{u_R}{\Omega R}\right)^2}} \quad (40)$$

The rotor advance ratio is $\mu_s = \frac{u_R}{\Omega R}$. The various f factors account for the fact that the rotor root is at the radius of the centerbody, R_s .

Define

$$\chi = \frac{R_s}{R}, \quad f_n = 1 - \chi^n$$

The expressions for the rotor forces in coefficient form are:

$$\begin{aligned} \frac{2C_T}{a\sigma} &= \frac{\theta_0}{3} \left[f_3 + \frac{3\mu_s^2}{2} f_1 \right] + \left(\frac{\lambda_s - \mu_s B_{1M}}{2} \right) f_3 + \frac{1}{2} \lambda_L \mu_s f_1 \\ \frac{2C_M}{a\sigma} &= -\frac{\theta_0}{2} \left[\frac{\lambda_L f_3}{2} + \mu_s \lambda_s f_1 \right] + \frac{B_{1M}}{4} \left[\lambda_s f_3 + \frac{3}{2} \mu_s \lambda_L f_1 \right] \\ &\quad + \frac{\mu_s A_{1M}}{8} \left[\lambda_M f_1 + \frac{\lambda_1}{2} f_3 \right] - \lambda_s \lambda_L f_1 + \frac{\delta}{2a} \mu f_3 \\ \frac{2C_Y}{a\sigma} &= -\frac{\theta_0}{2} \left[\frac{\lambda_1 f_3}{3} + \frac{\lambda_M f_3}{2} \right] + \frac{A_{1M}}{4} \left[\lambda_s f_3 + \frac{\mu}{2} \lambda_L f_1 \right] \\ &\quad + \frac{\mu B_{1M}}{8} \left[\lambda_M f_1 + \frac{\lambda_1}{2} f_3 \right] - \lambda_s \left[\lambda_M f_1 + \frac{\lambda_1}{2} f_3 \right] \end{aligned} \quad (41)$$

c.) Rotor Moments

The hub moments produced by the rotor were also developed in Reference 1, and are given by

$$\frac{2C_M}{a\sigma} = \frac{\frac{A_{1W}}{8} \left[f_4 + \frac{\mu_s^2}{2} f_2 \right] - \frac{1}{8} \lambda_1 f_4}{1 + \frac{1}{6} f_3} - \frac{\frac{1}{8} \frac{q_w}{\Omega} f_4}{1 + \frac{1}{6} f_3} \quad (42)$$

$$\frac{2C_L}{a\sigma} = \left\{ -\frac{B_{1W}}{8} \left[f_4 + \frac{3}{2} \mu_s^2 f_2 \right] + \mu_s \left[\frac{\theta_0}{3} f_3 + \frac{\lambda_s}{4} f_2 \right] \right\} \\ \times \left\{ \frac{1}{1 + \frac{1}{6} f_3} \right\} - \frac{\frac{1}{8} \frac{P_w}{\Omega} f_4}{1 + \frac{1}{6} f_3}$$

d.) Centerbody Forces

The drag and Magnus forces acting on the centerbody are given by the expressions

$$D = \frac{1}{2} \rho (U_0^2 + W_0^2) S C_D \quad (43)$$

and

$$F_M = \frac{1}{2} \rho (U_0^2 + W_0^2) S C_{LM} \quad (44)$$

The drag and Magnus force coefficients are assumed to be independent of centerbody advance ratio based on limited data presented in Reference 4.

This completes the development required for prediction of the trim conditions with the exception of the sling load and umbilical cable effects. These effects are considered in a later section.

To summarize the trim calculation, the physical parameters of the

vehicle are specified and the flight condition chosen. The flight condition implies that the horizontal and vertical velocities, U_0 and W_0 , are chosen as well as the body or gondola yaw angle, ψ . The gondola yaw angle physically reflects the orientation of the gondola with respect to the trimmed flight direction. Then the following equations must be solved simultaneously in the general case,

Balance of Forces, equations (8)

Balance of Moments, equations (16) or (18)

Velocity Component Relationships, equations (24)

with the conditions

$$v_R = 0$$

$$\alpha = \tan^{-1} \frac{w_R}{u_R}$$

Vehicle control, wind referenced control relationship,
equations (34)

Rotor and Centerbody Forces and Moments in terms of

Flight Condition, equations (41), (42), (43), and (44)

The solution of these equations yields trim values of the rotor cyclic and collective pitch, the vehicle pitch and roll angles, and the angle-of-attack and sideslip angle.

The velocity relationships are considerably simplified in the case of level flight reducing to the conditions $\beta = -\psi$, and $\alpha = \theta$.

It should be noted that this equilibrium solution does not include the effects of the sling load and umbilical cable. Appendix D discusses incorporation of these effects into equations (8) and (16).

Level flight was characteristic of all the flight conditions examined in the experimental program. Further, in the flight program, the gondola orientation was always selected such that $\psi = 0$ and therefore from (27), $\beta = 0$.

Consequently the simplified trim equations for initially level flight are, placing condition (27) on equations (8) and (16) level flight equations are as follows:

$$\begin{aligned} (-W + F_g) \sin \theta \cos \phi - H - D \cos \theta &= 0 \\ (W - F_g) \sin \phi + (Y + F_M) &= 0 \\ (W - F_g) \cos \theta \cos \phi - T - D \sin \theta &= 0 \\ L + r_o \{-F_g \sin \phi + (Y + F_M)\} &= 0 \\ M + r_o \{-F_g \sin \theta \cos \phi + H + D \cos \theta\} &= 0 \end{aligned} \tag{45}$$

The last two equations may also be written alternatively using equations (18) as

$$\begin{aligned} L - r_o W \sin \phi &= 0 \\ M - r_o W \sin \theta \cos \phi &= 0 \end{aligned} \tag{46}$$

These equations are then solved using the rotor and centerbody force and moment relationship given by equations (41) and (42). Note also that since the initial sideslip is zero

$$\begin{aligned} A_{1s} &= A_{1w} \\ B_{1s} &= B_{1w} \end{aligned} \tag{47}$$

The equations given by (45) were programmed on a digital computer and

solved for the trim condition. The method of approach was to initially solve the three force equations neglecting the rotor in-plane and side forces to determine initial values of the roll and pitch attitude and then the moment equations can be solved for the cyclic pitch required. Once an initial trim solution is obtained the rotor in-plane and side forces are calculated, added to the equations and a new trim condition calculated. Typically this procedure converges rapidly as the rotor in-plane and side forces have only a small influence on the trim attitudes.

II. DYNAMIC STABILITY ANALYSIS

This section develops equations of motion for the AEROCRANE incorporating a sling load. The attachment point of the load on the vehicle is taken to be an arbitrary point located on the axis of rotation. The load is assumed to be a point mass and has two-degrees-of-freedom with respect to the body. Aerodynamic forces on the sling load are neglected.

The forces and moments acting on the vehicle were resolved into a shaft axis system (X_s) in section I. The shaft system orientation is obtained by rotating the gravity axis system (X_g) through the vehicle roll and pitch angles. We now introduce two additional axis systems as necessary to proceed with the development of the vehicle-sling load equations:

a. Attachment Point Axes X_A (x_A, y_A, z_A)

These axes are always parallel to the shaft axes X_s . The origin of this axis system is located at the attachment point.

b. Load Axes X_L (x_L, y_L, z_L)

This axis system is a body axis system attached to the load with its origin at the load center of gravity. The z_L axis points downward and is

parallel to the support cable. These axes are shown schematically in Figure 1(c) and Figure 1(d) shows the freebody diagram employed in the analysis.

\bar{X}_s and \bar{L}_s are the force and moment vectors acting on the vehicle formulated in Part I given by equations (7) and (10). \bar{R}_L is the force vector which represents the force applied to the vehicle produced by the load and acts at the attachment point.

The equations of motion for the vehicle-load system can be written in vector form using Newton's Laws as

$$\begin{aligned}\dot{\bar{H}}_{c_g|F} + \bar{\Omega}_s \times \bar{H}_{c_g|F} &= \bar{P}_A \times \bar{R}_L + \bar{L}_s \\ m' \bar{a}_{c_g|F} &= \bar{R}_L + \bar{X}_s \\ m_L \bar{a}_{c_g|L} &= -\bar{R}_L + \bar{F}_{aL} \\ \dot{\bar{H}}_{c_g|L} + \bar{\Omega}_L \times \bar{H}_{c_g|L} &= (-\bar{P}_L) \times (-\bar{R}_L)\end{aligned}\tag{48}$$

The first two equations are the equations of motion of the vehicle where \bar{X}_s and \bar{L}_s were calculated in a previous section. The third and fourth equations are the load equations of motion. It has been assumed that there are no external forces acting on the load with the exception of the gravity forces. This assumption is quite reasonable owing to the high density of the load employed in the experiments. The sign of the moment term in the last equation arises from the fact that moments are taken about the load center of gravity. $\bar{H}_{c_g|F}$ is the moment of momentum of the vehicle with respect to the center of gravity of the vehicle and $\bar{\Omega}_s$ is the angular rate of the X_s axis system. $\bar{H}_{c_g|L}$ is the moment of momentum of the load with respect to the load center of gravity and $\bar{\Omega}_L$ is the angular velocity of the

load axis system with respect to space. The support cable has been assumed to be a massless rod. It is further assumed that the load is a point mass that is, that its moments of inertia are zero with respect to its center of gravity and consequently $\bar{H}_{c|L} = 0$. Therefore the fourth of equations (48) becomes

$$\bar{P}_L \times \bar{R}_L = 0$$

This implies that the reaction force \bar{R}_L always lies along the support cable direction. The reaction force can therefore be eliminated from the third of equations (48) by taking the cross product with \bar{P}_L so that the third equation becomes

$$m_L (\bar{P}_L \times \bar{a}_{c|L}) = \bar{P}_L \times \bar{F}_{aL}$$

\bar{R}_L is then eliminated from the first and second equations using the third equation

$$\bar{R}_L = \bar{F}_{aL} - m_L \bar{a}_{c|L}$$

so that equations (48) can be written as

$$\dot{\bar{H}}_{c|F} + \bar{\Omega}_S \times \bar{H}_{c|F} = \bar{P}_A \times (\bar{F}_{aL} - m_L \bar{a}_{c|L}) + \bar{L}_S$$

$$m' \bar{a}_{c|F} = (\bar{F}_{aL} - m_L \bar{a}_{c|L}) + \bar{X}_S \quad (49)$$

$$m_L (\bar{P}_L \times \bar{a}_{c|L}) = \bar{P}_L \times \bar{F}_{aL}$$

the last equation can also be written as

$$\bar{P}_L \times (m_L \bar{a}_{c|L} - \bar{F}_{aL}) = 0 \quad (49a)$$

Now the individual terms in equations (49) and (49a) are developed. $\bar{i}, \bar{j}, \bar{k}$ denote unit vectors with subscripts indicating their axis orientation.

The various accelerations involved in the equations of motion may be written as

$$\begin{aligned}\bar{a}_{c|L} &= \bar{a}_A + \bar{\Omega}_L \times (\bar{\Omega}_L \times \bar{P}_L) + \dot{\bar{\Omega}}_L \times \bar{P}_L \\ \bar{a}_{c|r} &= \dot{u}_s \bar{i}_s + \dot{v}_s \bar{j}_s\end{aligned}\tag{50}$$

The attachment point acceleration is

$$\bar{a}_A = \bar{a}_{c|r} + \bar{\Omega}_s \times (\bar{\Omega}_s \times \bar{P}_A) + \dot{\bar{\Omega}}_s \times \bar{P}_A$$

The various terms in equations (49) and (50) are given by

$$\begin{aligned}\bar{P}_A &= Z_A \bar{k}_s \\ \bar{P}_L &= Z_L \bar{k}_L \\ \bar{\Omega}_s &= p_s \bar{i}_s + q_s \bar{j}_s \\ \bar{\Omega}_L &= p_s \bar{i}_s + q_s \bar{j}_s + p_L \bar{i}_L + q_L \bar{j}_L \\ \bar{F}_{cL} &= m_L g \bar{k}_s\end{aligned}\tag{51}$$

p_L and q_L are the angular velocities of the load relative to the vehicle which has angular velocities p_s and q_s .

The angular displacements of the load axes with respect to the shaft axes are given by a roll angle ϕ_L and a pitch angle θ_L so that the relationships among the various axes are

$$\begin{aligned}X_s &= \theta \phi X_e \\ X_L &= \theta_L \phi_L X_s\end{aligned}$$

Thus

$$\begin{Bmatrix} \bar{i}_s \\ \bar{j}_s \\ \bar{h}_s \end{Bmatrix} = \begin{bmatrix} \cos \theta & \sin \theta \sin \phi & -\sin \theta \cos \phi \\ 0 & \cos \phi & \sin \phi \\ \sin \theta & -\sin \phi \cos \theta & \cos \theta \cos \phi \end{bmatrix} \begin{Bmatrix} \bar{i}_e \\ \bar{j}_e \\ \bar{k}_e \end{Bmatrix} \quad (52)$$

and

$$\begin{Bmatrix} \bar{i}_l \\ \bar{j}_l \\ \bar{h}_l \end{Bmatrix} = \begin{bmatrix} \cos \theta_l & \sin \theta_l \sin \phi_l & -\sin \theta_l \cos \phi_l \\ 0 & \cos \phi_l & \sin \phi_l \\ \sin \theta_l & -\sin \phi_l \cos \theta_l & \cos \theta_l \cos \phi_l \end{bmatrix} \begin{Bmatrix} \bar{i}_s \\ \bar{j}_s \\ \bar{k}_s \end{Bmatrix}$$

The development is specialized for hovering flight by assuming that the initial vehicle and load attitude angles are zero such that θ , ϕ , θ_l and ϕ_l represent perturbations from trim. It is further assumed that these perturbations are small so that equations (52) can be expressed as

$$\begin{aligned} \bar{i}_s &= \bar{i}_e - \theta \bar{k}_e \\ \bar{j}_s &= \bar{j}_e + \phi \bar{k}_e \\ \bar{k}_s &= \theta \bar{i}_e - \phi \bar{j}_e + \bar{k}_e \\ \bar{i}_l &= \bar{i}_s - \theta_l \bar{k}_s \\ \bar{j}_l &= \bar{j}_s + \phi_l \bar{k}_s \\ \bar{k}_l &= \theta_l \bar{i}_s - \phi_l \bar{j}_s + \bar{k}_s \end{aligned} \quad (53)$$

For the load equation, it is desirable to express the gravity force in terms of components in the load axis directions. This is accomplished

by inverting transformation (52)

$$\begin{pmatrix} \bar{i}_e \\ \bar{j}_e \\ \bar{k}_e \end{pmatrix} = \begin{bmatrix} \cos \theta & 0 & \sin \theta \\ \sin \theta \sin \phi & \cos \phi & -\sin \phi \cos \theta \\ -\sin \theta \cos \phi & \sin \phi & \cos \theta \cos \phi \end{bmatrix} \begin{pmatrix} \bar{i}_s \\ \bar{j}_s \\ \bar{k}_s \end{pmatrix}$$

$$\begin{pmatrix} \bar{i}_s \\ \bar{j}_s \\ \bar{k}_s \end{pmatrix} = \begin{bmatrix} \cos \theta_L & 0 & \sin \theta_L \\ \sin \theta_L \sin \phi_L & \cos \phi_L & -\sin \phi_L \cos \theta_L \\ -\sin \theta_L \cos \phi_L & \sin \phi_L & \cos \theta_L \cos \phi_L \end{bmatrix} \begin{pmatrix} \bar{i}_L \\ \bar{j}_L \\ \bar{k}_L \end{pmatrix}$$

For small angles

$$\begin{aligned} \bar{i}_e &= \bar{i}_s + \theta \bar{k}_s \\ \bar{j}_e &= \bar{j}_s - \phi \bar{k}_s \\ \bar{k}_e &= -\theta \bar{i}_s + \phi \bar{j}_s + \bar{k}_s \\ \bar{i}_s &= \bar{i}_L + \theta_L \bar{k}_L \\ \bar{j}_s &= \bar{j}_L - \phi_L \bar{k}_L \\ \bar{k}_s &= -\theta_L \bar{i}_L + \phi_L \bar{j}_L + \bar{k}_L \end{aligned} \tag{54}$$

Substituting from the second set of relationships in (54) into the first

$$\bar{k}_e = \bar{i}_L (-\theta - \theta_L) + (\phi + \phi_L) \bar{j}_L + \bar{k}_L \tag{55}$$

where only first order terms have been retained as consistent with the small

angle approximation.

The load angular velocity expressed in load coordinates becomes

$$\bar{\Omega}_L = (\dot{p}_S + \dot{p}_L) \bar{i}_L + (\dot{q}_S + \dot{q}_L) \bar{j}_L$$

where only first order terms have been retained.

The load acceleration is given by

$$\bar{a}_{c_g|L} = \bar{a}_A + (\dot{q}_S + \dot{q}_L) Z_L \bar{i}_L - (\dot{p}_S + \dot{p}_L) Z_L \bar{j}_L \quad (56)$$

where again only first order terms have been retained. The acceleration at the attachment point \bar{a}_A is given by

$$\begin{aligned} \bar{a}_L = \bar{a}_{c_g|F} &+ \{\dot{q}_S Z_A \bar{i}_S\} \\ &- \{\dot{p}_S Z_A \bar{j}_S\} \end{aligned} \quad (57)$$

Converting equation (57) to the load axes reference using (54), retaining only first order terms and incorporating into (56),

$$\begin{aligned} \bar{a}_{c_g|L} = \bar{a}_{c_g|F} &+ \{\dot{q}_S (Z_A + Z_L) + \dot{q}_L Z_L\} \bar{i}_L \\ &- \{\dot{p}_S (Z_A + Z_L) + \dot{p}_L Z_L\} \bar{j}_L \end{aligned} \quad (58)$$

Equations (58) and (55) are now employed to express the reaction force \bar{R}_L in load coordinates

$$\bar{R}_L = \bar{F}_{eL} - m_L \bar{a}_{c_g|L}$$

$$\begin{aligned}
\bar{R}_L &= m_L g \{ \bar{k}_L - (\theta + \theta_L) \bar{i}_L + (\phi + \phi_L) \bar{j}_L \} \\
&- m_L \{ \bar{a}_{cs}|_L + [\dot{q}_s (Z_A + Z_L) + \dot{q}_L Z_L] \bar{i}_L \\
&- [\dot{p}_s (Z_A + Z_L) + \dot{p}_L Z_L] \bar{i}_L \}
\end{aligned} \tag{59}$$

Expressing the components of this vector as

$$\begin{aligned}
X_L &= - m_L g (\theta + \theta_L) - m_L [\dot{q}_s (Z_A + Z_L) + \dot{q}_L Z_L] - m_L \ddot{u}_s \\
Y_L &= m_L g (\phi + \phi_L) + m_L [\dot{p}_s (Z_A + Z_L) + \dot{p}_L Z_L] - m_L \ddot{v}_s \\
Z_L &= m_L g
\end{aligned} \tag{59a}$$

so that

$$(\bar{F}_{GL} - m_L \bar{a}_{cs}|_L) = X_L \bar{i}_L + Y_L \bar{j}_L + Z_L \bar{k}_L$$

The load equation of motion is obtained from (49a) as

$$\bar{P}_L \times (m_L \bar{a}_{cs}|_L - \bar{F}_{GL}) = 0$$

or

$$\bar{j}_L Z_L X_L - \bar{i}_L Z_L Y_L = 0$$

For the second of equations (49) the reaction \bar{R}_L is expressed in terms of shaft coordinates. This is obtained from the unit vector relationships given in (53) taken with equations (59a). Since X_L and Y_L are perturbation quantities the result is

$$\begin{aligned}
(\bar{F}_{GL} - m_L \bar{a}_{cs}|_L) &= (X_L + \theta_L Z_L) \bar{i}_s \\
&+ (Y_L - \phi_L Z_L) \bar{j}_s + Z_L \bar{k}_s
\end{aligned} \tag{60}$$

since $Z_L = m_L g$, equation (60) can be written as

$$\begin{aligned} \bar{F}_{GL} - m_L \bar{a}_{cG|L} &= (X_L + m_L g \theta_L) \bar{i}_s \\ &+ (Y_L - m_L g \phi_L) \bar{j}_s + m_L g \bar{k}_s \end{aligned} \quad (60a)$$

This is the form of the reaction force required for the second of equations (49). For the first of equations (49), the cross product $\bar{P}_A \times (\bar{F}_{GL} - m_L \bar{a}_{cG|L})$ must be calculated where $\bar{P}_A = Z_A \bar{k}_s$. Taking the cross product using equations (60a)

$$\begin{aligned} \bar{P}_A \times (\bar{F}_{GL} - m_L \bar{a}_{cG|L}) &= \bar{j}_s \{Z_A (X_L + m_L g \theta_L)\} \\ &- \bar{i}_s \{Z_A (Y_L - m_L g \phi_L)\} \end{aligned}$$

The equations of motion can be written as

$$\begin{aligned} \dot{\bar{H}}_{cG|F} + \bar{\Omega}_s \times \bar{H}_{cG|F} &= \bar{j}_s \{Z_A (X_L + m_L g \theta_L)\} \\ &- \bar{i}_s \{Z_A (Y_L - m_L g \phi_L)\} + \bar{L}_s \end{aligned} \quad (61)$$

$$\begin{aligned} m' \bar{a}_{cG|F} &= (X_L + m_L g \theta_L) \bar{i}_s \\ &+ (Y_L - m_L g \phi_L) \bar{j}_s + m_L g \bar{k}_s + \bar{X}_s \end{aligned}$$

$$\bar{j}_L Z_L X_L - \bar{i}_L Z_L Y_L = 0$$

where X_L and Y_L are given by equations (59a).

Equations (61) are the equations of motion for the AEROCRANE with a point mass sling load. These equations can be simplified by noting that the last of these equations reduces to

$$\begin{aligned} X_L &= 0 \\ Y_L &= 0 \end{aligned} \quad (62)$$

so that the first two equations become

$$\begin{aligned} \dot{\bar{H}}_{c_0|f} + \bar{\Omega}_s \times \bar{H}_{c_0|f} &= \bar{L}_s + \bar{J}_s (Z_A m_L g \theta_L) \\ &+ \bar{I}_s (Z_A m_L g \phi_L) \end{aligned} \quad (63)$$

$$m' \bar{a}_{c_0|f} = m_L g \theta_L \bar{I}_s - m_L g \phi_L \bar{J}_s + m_L g \bar{k}_s + X_s$$

Expanding equations (62) and (63)

$$I' \dot{p} + I_z \Omega q = L_s + Z_A m_L g \phi_L$$

$$I' \dot{q} - I_z \Omega p = M_s + Z_A m_L g \theta_L$$

$$m' \dot{u}_s = X_s + m_L g \theta_L$$

$$m' \dot{v}_s = Y_s - m_L g \phi_L$$

(64)

$$- m_L \dot{u}_s - m_L g (\theta + \theta_L) - m_L (\dot{q}_s (Z_A + Z_L) + \dot{q}_L Z_L) = 0$$

$$- m_L \dot{v}_s + m_L g (\phi + \phi_L) + m_L (\dot{p}_s (Z_A + Z_L) + \dot{p}_L Z_L) = 0$$

Equations (64) are equations of motion for the AEROCRANE including the effects of a sling load. They have been specialized for the hovering case by the assumption of zero initial attitudes. For the general case of forward flight the assumption of zero initial trim angles must be removed.

as a result of the small angle assumption

$$\dot{q}_L = \ddot{\theta}_L$$

$$\dot{p}_L = \ddot{\phi}_L$$

and

$$\dot{q}_s = \ddot{\theta}$$

$$\dot{p}_s = \ddot{\phi}$$

Substituting into equations (64)

$$\begin{aligned}
 I' \ddot{\phi} + I_z \Omega \dot{\theta} &= L_s + Z_A m_L g \phi_L \\
 I' \ddot{\theta} - I_z \Omega \dot{\phi} &= M_s + Z_A m_L g \theta_L \\
 m' \dot{u}_s &= X_s + m_L g \theta_L \\
 m' \dot{v}_s &= Y_s - m_L g \phi_L \\
 - m_L \dot{u}_s - m_L g (\theta + \theta_L) - m_L (\ddot{\theta} (Z_A + Z_L) + \ddot{\theta}_L Z_L) &= 0 \\
 - m_L \dot{v}_s + m_L g (\phi + \phi_L) + m_L (\ddot{\phi} (Z_A + Z_L) + \ddot{\phi}_L Z_L) &= 0
 \end{aligned} \tag{65}$$

The expansion of X_s , Y_s , L_s , and M_s in a Taylor series about the equilibrium flight condition has been treated in detail in Reference 1. There are additional aerodynamic terms which were developed in Reference 1 which depend upon the acceleration of the vehicle and arise from the fact that the center of gravity of the vehicle is not located at the center of buoyancy.

These terms are with signs for the right hand side of the equations

Rolling Moment equation

$$- r_o m_a \dot{v}_s$$

Pitching Moment equation

$$r_o m_a \dot{u}_s$$

Horizontal Force equation

$$r_o m_a \ddot{\theta}$$

Lateral Force equation

$$- r_o m_a \ddot{\phi}$$

(66)

Further the effects of the umbilical cable must be added. These are developed in detail in Appendix B and are given by the sum of equations (B-18) and (B-34) as

Rolling Moment equation

$$m_{ce} Z_A (-\dot{v}_s + Z_A \ddot{\phi}) - W_c Z_A (1 + \frac{d\beta}{d\phi} \frac{y}{\phi}) \phi$$

Pitching Moment equation

$$m_{ce} Z_A (\dot{u}_s + Z_A \ddot{\theta}) - W_c Z_A (1 + \frac{d\beta}{d\theta} \frac{x}{\theta}) \theta$$

Horizontal Force equation

$$m_{ce} (\dot{u}_s + Z_A \ddot{\theta}) - W_c (1 + \frac{d\beta}{d\theta} \frac{x}{\theta}) \theta$$

(67)

Lateral Force equation

$$m_{ce} (\dot{v}_s - Z_A \ddot{\phi}) + W_c (1 + \frac{d\beta}{d\phi} \frac{y}{\phi}) \phi$$

Combining equations (65), (66) and (67) gives the hovering equations of motion.

These equations may be written compactly in matrix notation as

$$M \{\ddot{q}\} + C \{\dot{q}\} + K \{q\} = F \{\delta\} \quad (68)$$

The mass, damping, spring, and control matrices, M, C, K, and F are given on the following pages. The motion variables {q} are

$$\{q\} = \begin{pmatrix} \phi \\ \theta \\ \phi_t \\ \theta_t \\ x \\ y \end{pmatrix}$$

The control matrix {δ} is

$$\{\delta\} = \begin{pmatrix} A_{1s} \\ B_{1s} \end{pmatrix}$$

These equations of motion were solved to determine the characteristic dynamics of the vehicle.

The moment equations are normalized by the inertia I' , the force equations by the mass m' , and the sling load equations are divided by the sling load mass times the sling load length. In order to make the notation more compact the following symbols were introduced.

$$\omega_p^2 = \frac{F_s r_o}{I'}$$

$$\omega_\phi = \frac{I_z}{I'} \Omega$$

$$\omega_{sl}^2 = \frac{g}{Z_l}$$

In addition, the symmetry properties of the aerodynamic derivatives were employed to eliminate the lateral derivatives, i.e.,

$$L_p = M_q$$

$$L_{s_{1s}} = -M_{A_{1s}}$$

$$L_v = -M_u$$

$$Y_{A_{1s}} = H_{s_{1s}}$$

$$L_u = M_v$$

$$Y_u = H_v$$

$$Y_v = H_u$$

$$Y_q = -H_p$$

The subscript notation for the aerodynamic derivatives implies that the moment derivatives have been divided by I' and the force derivatives by m' .

$$M =$$

$1 + \frac{m_{ce} z_p^2}{I'}$					$\frac{m_{ce} z_p}{I'}$ $-\frac{m_{ce} z_p}{I'}$
	$1 + \frac{m_{ce} z_p^2}{I'}$			$-\frac{m_{ce} z_p}{I'}$ $+\frac{m_{ce} z_p}{I'}$	
$1 + \frac{z_p^2}{I'}$		1			$-\frac{1}{I'}$
	$1 + \frac{z_p^2}{I'}$		1	$\frac{1}{I'}$	
	$-\frac{m_{ce} z_p}{m'}$ $+\frac{m_{ce} z_p}{m'}$			$1 + \frac{m_{ce}}{m'}$	
$\frac{m_{ce} z_p}{m'}$ $-\frac{m_{ce} z_p}{m'}$					$1 + \frac{m_{ce}}{m'}$

MASS MATRIX

$C =$

$-Mq$	ω_e			$-Mv$	Mu
$-\omega_e$	$-Mq$			$-Mu$	$-Mv$
$-H_p$				$-Hu$	$-Hv$
	H_p			Hu	Hu

DAMPING MATRIX

$K =$

ω_p^2 $+\frac{W_p^2}{T^2}\left(+\frac{d\theta}{d\theta}\right)$		$-\frac{W_c^2}{T^2}$			
	ω_p^2 $+\frac{W_p^2}{T^2}\left(+\frac{d\theta}{d\theta}\right)$		$-\frac{W_c^2}{T^2}$		
ω_{SL}^2		ω_{SL}^2			
	ω_{SL}^2		ω_{SL}^2		
	$\frac{W_0 - F_B}{m'}$ $+\frac{W_c}{T}\left(+\frac{d\theta}{d\theta}\right)$		$-\frac{W_L}{m'}$		
$-\frac{W_0 - F_B}{m'}$ $+\frac{W_c}{T}\left(+\frac{d\theta}{d\theta}\right)$		$\frac{W_L}{m'}$			

SPRING MATRIX

F =

	$-M_{ms}$
M_{ms}	
	H_{ex}
H_{ex}	

CONTROL MATRIX

The object of the experimental program was to determine the vehicle transfer functions, which can be obtained from equations (68) in the following fashion. First the Laplace transform of equations (68) is taken giving

$$[Ms^2 + Cs + K] \{Q\} = F \{\Delta\} \quad (69)$$

where $\{Q\}$ is the Laplace transform of the motion variables $\{q\}$ and $\{\Delta\}$ is the Laplace transform of the control variables $\{\delta\}$. Equations (69) become

$$\{Q\} = [Ms^2 + Cs + K]^{-1} F \{\Delta\} \quad (70)$$

There are twelve vehicle transfer functions, given by the elements of the matrix $[Ms^2 + Cs + K]^{-1} F$. The twelve elements of the matrix are shown symbolically in the next page. These elements characterize the response of the vehicle and sling load to the control inputs. Since there are six motion variables and two control variables, twelve transfer functions are required to characterize the dynamic motions of the vehicle.

The transient response experiments were designed to verify the analytically calculated transfer functions which describe mathematically the dynamic response of the model. Owing to the polar symmetry of the model and its aerodynamic characteristics in hovering flight, six of these transfer functions are simply related to the other six by the following relationships

$$\frac{\phi(s)}{A_{1\theta}(s)} = \frac{\theta(s)}{B_{1\phi}(s)}$$

$$\frac{\theta(s)}{A_{1\phi}(s)} = -\frac{\phi(s)}{B_{1\theta}(s)}$$

$$\frac{\phi_L(s)}{A_{1\theta}(s)} = \frac{\theta_L(s)}{B_{1\phi}(s)}$$

$$\frac{\theta_L(s)}{A_{1\phi}(s)} = -\frac{\phi_L(s)}{B_{1\theta}(s)}$$

$$\frac{X(s)}{A_{1s}(s)} = \frac{Y(s)}{B_{1s}(s)}$$

$$\frac{Y(s)}{A_{1s}(s)} = -\frac{X(s)}{B_{1s}(s)}$$

Owing to these relationships only a B_{1s} input was applied in hovering, as the response of the vehicle to A_{1s} inputs can be determined from the response to B_{1s} inputs.

The experimental verification of these transfer functions is discussed in a later section of the report.

$$[Ms^2 + Cs + K]^{-1} F = \begin{bmatrix} \frac{\phi(s)}{A_{1g}(s)} & \frac{\phi(s)}{B_{1g}(s)} \\ \frac{\theta(s)}{A_{1g}(s)} & \frac{\theta(s)}{B_{1g}(s)} \\ \frac{\phi_L(s)}{A_{1g}(s)} & \frac{\phi_L(s)}{B_{1g}(s)} \\ \frac{\theta_L(s)}{A_{1g}(s)} & \frac{\theta_L(s)}{B_{1g}(s)} \\ \frac{x(s)}{A_{1g}(s)} & \frac{x(s)}{B_{1g}(s)} \\ \frac{y(s)}{A_{1g}(s)} & \frac{y(s)}{B_{1g}(s)} \end{bmatrix}$$

MATRIX OF TRANSFER FUNCTIONS

EXPERIMENTAL APPARATUS

I. MODEL

The model employed for the experiments described in this report is a modification of the 0.107 Froude scale model of a proposed 50 ton payload AEROCRANE vehicle as described in Reference 1. The modifications consisted principally of an increase in the spherical centerbody diameter, provision of a dumpable water ballast package and incorporation of a stability augmentation system. According to the conclusions and recommendations made in Reference 1, these modifications were provided to increase flight safety by allowing positive buoyancy to be achieved at all times and to ease the remote pilot's task in controlling the lightly damped model motions with inadequate motion cues.

A photograph of the modified model in hovering flight and showing the dumpable water ballast sling load is shown in Figure 2, and a 2-view drawing is presented in Figure 3. Table I presents a summary of the model physical characteristics.

II. CENTERBODY MODIFICATIONS

To achieve the additional buoyancy required for flight safety considerations the gas-containing spherical centerbody was increased in diameter from 16 feet to 18 feet, providing an additional 60 lb of buoyant lift. The increased gas envelope size necessitated a revised internal structure consisting of longer frame members, addition of internal stress-relief cables and gas envelope stress-relief patches at the radial pass-through fittings

to accommodate the increased buoyant gas loads. These structural modifications are shown schematically in Figure 4.

III. WATER BALLAST SYSTEM

The jettisonable water ballast used to simulate a payload was carried in a special aluminum container with a trap-door type bottom and suspended from the model gondola as a sling load as shown in Figure 2. The water was contained in a plastic bag liner fitting within the aluminum container. The trapdoor latch was secured with light polyester fishing line which was in turn wrapped with a coil of high electrical resistance wire. Upon command from the truck-based operator an electric current would heat the high resistance wire, melt the polyester fishing line and allow the trapdoor to open, thereby jettisoning the water ballast. Electric power for the jettison was provided by a dedicated 24 volt battery, thereby assuring operation even with complete power loss from the truck generator systems.

IV. STABILITY AUGMENTATION SYSTEM

As a result of the flight test experience and analysis efforts reported in Reference 1, it was determined that a stability augmentation system (SAS) to stabilize the lightly-damped retrograde precessional mode would greatly ease the remote pilot's burden in controlling the model. Although it was demonstrated in analog simulator flights that the pilot, with adequate motion cues, could stabilize this mode, in the model flight operations the required cues were not available to the remote pilot, and controlled flight was nearly impossible. Further, it was shown in Reference 1 that a phased attitude feedback given by the expressions

$$A_{1s} = K_A [\phi \sin \gamma - \theta \cos \gamma] \quad (69)$$

$$B_{1s} = K_A [\phi \cos \gamma + \theta \sin \gamma] \quad (70)$$

would effectively stabilize the lightly-damped precessional mode. Accordingly, for the experiments reported herein, a stability augmentation system was implemented to accomplish this task.

In view of the exploratory nature of the research, the time constraints associated with the experimental operations and the test objective of forward flight experiments, a more general stability augmentation system was designed and installed in the model controller. This stability augmentation system, schematic representations of which are shown in Figures 5 and 6, allowed for selection of any desired feedback phasing angle, γ , in addition to $\gamma = 45^\circ$ as indicated by equations (69) and (70). Additionally, although the hovering analysis of Reference 1 indicated no specific need for angular rate feedbacks, these were allowed for in the implementation as diagrammed in Figure 6.

Model attitude and rate information was supplied to the SAS (stability augmentation system) by the three-axis integrating rate gyro package described in Reference 1. This instrumentation package, originally intended for flight dynamic data acquisition, was more than adequate for SAS inputs and performed faultlessly. The analog integrators required for determining model attitude from the rate gyro information were revised to virtually eliminate environmentally-produced drift errors.

V. AZIMUTH-HOLD LOOP

The azimuth-hold loop, driving the retrograde motor that allowed the gondola to be positioned azimuthally, was revised to provide greater torque capability and thereby eliminate the difficulties experienced in the flight tests report in Reference 1. The revised system possessed approximately 4 times the torque capability of the original system. Extensive laboratory testing of this vital loop closure was performed on a specifically-designed flight simulation set-up to insure satisfactory performance, and, although in-flight performance was adequate throughout the flight envelope, certain dynamic problems were encountered in flight, and loop compensation adjustments were required.

VI. RAPID DECELERATION SYSTEM

A necessary function in the flight safety systems that includes rapid achievement of a fully-buoyant state through ballast dump is the rapid deceleration of the model rotational motion. The model rpm control system operates through varying the speed of the four fixed-pitch propellers mounted on the model wings by adjusting the output of the main 400 Hz model-power alternator. In order to decelerate the model rotational motion rapidly it is necessary to actually reverse the propulsive motor voltage polarity and hence reverse the direction of rotation of the propellers. To accomplish this, reversing-current relays were installed on the model gondola electrically downstream of the rectifier package. A high sensitivity alternator field control potentiometer was incorporated to allow the operator to rapidly reduce the motor power to near zero, actuate the polarity reversing relays

and subsequently reactivate the alternator field to provide reversed thrust. The system in operation was capable of arresting the model rotation in approximately one revolution without exceeding model motor rated currents. Thus, in the event of an in-flight problem that threatened the flight safety of the model, the model rotational motion could be arrested and a fully-buoyant state achieved by ballast dump in approximately 3 seconds.

EXPERIMENTAL FLIGHT TEST PROGRAM

The experimental flight test program was conducted in Hangar No. 1 at the Naval Air Engineering Center, Lakehurst, N. J. in the time period from March 21, 1977 to May 2, 1977. A total of 56 data runs were performed and approximately 20 hours of flight time were accumulated. The principal test objectives were to quantify the model trim conditions and transfer functions as they varied with flight condition, model configuration and stability augmentation (SAS) for correlation with the theoretically predicted characteristics.

The flight testing efforts and procedures were divided into two principal types of tests, hovering and forward flight; each of these types will be discussed separately.

I. HOVERING FLIGHT

A photograph of the model in a typical hovering flight is presented in Figure 7 showing the model, water ballast sling load and umbilical. At the bottom of the photograph can be seen the parked truck which carries the crew, model control and power systems. A photograph of the flight crew arrangement is presented in Figure 8 showing the pilot, flight engineer and test director at the model system control and data consoles. Although the photograph of Figure 7 shows the bottom of the umbilical suspended from a tower mounted on the test truck, most of the hover runs were accomplished without the tower, and the umbilical ran downward from the model directly to the ground. This arrangement allowed hovering tests to be performed without any horizontal force or moment contribution from the umbilical cable

Other hover tests with the umbilical tower, as pictured in Figure 7, were performed with horizontal force and moment initial conditions imposed by the umbilical catenary shape. A summary of the hovering test conditions investigated is presented in Table II.

The hovering tests were performed by establishing a steady hover condition with the bottom of the model approximately 90 ft. above the ground and with the umbilical hanging directly downward. This zero-initial-condition hover was established with the SAS in operation at $\gamma = 45^\circ$ and with the gain $K_A \approx 0.3\%$. This SAS configuration has been established on the initial run as being a level of stability augmentation that was completely comfortable to the pilot and for which the undisturbed model motions were undetectable. At these initial conditions the SAS gain was reduced to the level desired for the particular test sequence, and a pulse input in cyclic pitch was applied by the test engineer by means of a switch on the engineer's console. After establishing the initial conditions and throughout the ensuing transient response, the pilot's controls were held fixed. Figure 9 shows typical hovering transient responses for the unstabilized model and with various level of SAS gain.

II. FORWARD FLIGHT EXPERIMENTS

Photographs of the model during forward flight experiments are presented in Figures 10 and 11. In these figures can be seen the relative position of the model, umbilical catenary and the truck carrying the crew and model support systems. The forward flight tests required additional instrumentation, not

necessary for the hovering experiments, consisting of a fifth wheel for measuring truck speed, and umbilical shape and position instrumentation. The fifth wheel is mounted under the rear of the truck as seen in Figure 11 and the umbilical shape and position instrumentation is mounted at the top of the umbilical support tower on the truck.

The test procedure for the forward flight runs commenced with establishing a steady hover in the northwest corner of the hangar immediately to the right of the center crack in the hangar doors visible in Figure 10. Owing to the presence of a fenced in storage area, also visible in the foreground of Figure 10, it was necessary to fly along a diagonal path towards the southeast corner of the hangar. Runs were made in one direction only, principally to eliminate the necessity of recompensating the rate gyro package for earth's rotational rate. Once a steady hover had been established with the model in a position relative to the truck that was acceptable with respect to altitude and umbilical shape, the pilot would apply the cyclic and collective pitch inputs required to transition the model to the desired forward flight condition. The truck driver was required to adjust the truck speed to stationkeep with the model. The desired forward flight trim conditions were established with a nominal SAS gain of approximately $0.3 \text{ }^{\circ}/\text{s}$ and $\gamma = 45^{\circ}$. For the initial forward flight runs the trim condition was maintained steadily with no additional control inputs in order to measure the model trim conditions. At a predetermined location along the line of flight the transition back to hovering flight was instituted and the end of run hover established. In general, excepting for the very lowest speed flights, transitions to and from the forward

flight trim conditions were made with the pilot operating in an open loop fashion. That is, there was inadequate space within the hangar for the pilot to perform a transition by a series of small perturbations to the controls and subsequent corrections to flight path errors. Instead, estimated trim control positions were predetermined and the pilot simply put the control at these values, at a prudent rate, to perform the transition. The SAS-augmented model stability level was such that no difficulty was experienced in transitioning in this manner. A typical transition time history is presented in Figure 12 showing the pilot's control inputs and the ensuing model pitch and roll angular motions.

The data required to determine the model transfer function to control inputs were obtained, as in hover, by applying an electrical pulse input to the cyclic controls by means of a switch. In forward flight, however, in order to obtain the unstabilized ($K_A = 0$) model transfer function and still maintain the required trim control settings, it was necessary to utilize track and hold networks on the model control signals. These networks held the trim controls required while the SAS gain was switched to zero to obtain the desired transient response time histories. Such a typical transient response time history at a forward flight trim condition is shown in Figure 13. Table III present a summary of the forward flight trim conditions.

COMPARISON OF ANALYSIS AND EXPERIMENT

The results of the flight test experiments and the theoretical developments have been compared on a run by run basis to corroborate the analytical models. Where necessary, adjustments have been made in the theoretical representations to obtain better agreement between theory and experiment. In general, only fractional adjustments in various coefficients were required to obtain excellent correlation between the experimental results and the analytical models.

I. TRIM CORRELATION

The correlation between theory and experiment for forward flight trim conditions is presented in Figures 14 through 16 which show comparisons of measured and predicted model longitudinal and lateral equilibrium conditions. The correlation demonstrated in these figures was obtained by adjusting the assumed value of C_D of the rotating spherical centerbody principally on the basis of the longitudinal equilibrium comparison. The resulting value of $C_D = 0.80$ is a 33% increase over the $C_D = 0.60$ value assumed in Reference 1, taken from Reference 4. No adjustment was required to the assumed value of Magnus lift coefficient, $C_{L_M} = 0.30$, and the rotor wake representations remain as developed in Reference 1.

1. Longitudinal and Lateral Force Equilibrium

The expressions for force equilibrium, equations (45), can be combined and solved directly for the Magnus lift and drag forces, giving:

$$F_M = -(W - F_g) \sin \phi - Y - SY \cos \phi$$

and

$$D = -\frac{H}{\cos \theta} - \left\{ \frac{(W - F_g)}{\cos \phi} + (Y + F_M) \tan \phi \right\} \tan \theta + SX$$

where the additional terms SX and SY represent the measured umbilical forces acting on the model, and level flight at zero sideslip has been assumed. These quantities have been evaluated using the experimentally-measured values for all terms excepting Y and H, the rotor in-plane forces, which were evaluated using the theoretical model at the experimental operating conditions. The resulting values are presented in Figures 14 and 15 and compared with the theoretical values for F_M and D employing the assumed force coefficients.

As can be seen in Figure 14, the original value of $C_D = 0.6$ seriously under predicts the values of centerbody drag extracted from the experimental data and a value of $C_D = 0.80$ is chosen as being a fair representation of the drag coefficient within the experimental scatter. The sources of the experimental scatter in the drag data, include, in probable order of importance, determination of model velocity from truck speed measurements, wind currents within the hangar and accuracy of measurement of umbilical shape and position.

The last source of error is particularly important in the determination of F_M since the umbilical lateral force term, SY, was not measured directly but was inferred from the beginning-of-run hover umbilical position. This uncertainty is reflected in the relatively-larger scatter shown in the experimental F_M data presented in Figure 15. The theoretical Magnus force, assuming a value of $C_{L_M} = 0.30$, is shown in Figure 15 in comparison with the experimental data. Due to the mentioned experimental uncertainties and the resulting data scatter it was concluded that it would be unjustified to attempt to refine the Magnus lift coefficient value any further.

2. Trim Control Requirements

The data presented in Figure 16 show comparisons of theoretical and experimental values for the longitudinal and lateral cyclic pitch required for trim. While the force equilibrium equations (8) used to express the centerbody aerodynamic forces are influenced by the assumed rotor aerodynamics through the H and Y terms, the cyclic pitch requirements for trim presented in Figure 16 are much more indicative of the accuracy of the rotor aerodynamics representation. In particular the good low speed agreement between theory and experiment shown in the A_{1s} data indicates the absence of significant sphere wake interference effects since they are not included in the theory. At higher speeds and inclination angles, where sphere wake interference would be expected to be less severe and not a factor, the experimental A_{1s} values are somewhat greater than those predicted by theory and the B_{1s} values are in very good agreement. A possible explanation for this may be in the less-than-perfect Coleman representation of the rotor wake longitudinal "blow back". The possibility of blade stall tends to be ruled out by the fact that the average blade lift coefficients are approximately the same value across the lateral axis as across the longitudinal axis.

In general, the predicted cyclic pitch requirements for trim are in good agreement with the experimental measurements, and it can be concluded that the rotor aerodynamic representations are acceptably accurate for the objectives of predicting force and moment equilibrium.

II. TRANSIENT RESPONSE CORRELATION

This section discusses the correlation between the experimentally measured transient response characteristics of the AEROCRANE model in various configurations and flight conditions and the theoretical predictions. Experimental measurements were made of the transient response to control inputs in hovering flight at two center of gravity positions with various sling loads and levels of automatic stabilization, Table II indicates various model configurations examined in hovering flight.

Figure 9 is typical of the data obtained. Additional measurements are presented in Figures A-1 through A-6 in Appendix A. It should be noted that the cyclic pitch trace includes the cyclic pitch applied by the automatic stabilization system as well as that applied by the operator. A pulse input of approximately two seconds duration with an amplitude of two degrees was employed to excite the transient motion of the model.

The transient response of the unstabilized model is characterized by a lightly damped mode with a period of the order of ten seconds and a damping ratio of less than 0.1. Figure 17 presents the frequency and damping characteristics of this mode as measured from the traces. These measurements should be viewed as approximations to the character of this mode as it can be seen from the measured time histories that the responses are not precisely damped sinusoids indicating the presence of some of the other modes of motion. Also shown is the comparison between the theoretically predicted characteristics of this mode as given in Appendix C with the measured values. The agreement between theory and experiment is excellent for the high center of gravity configuration. The damping agrees well for the low center of gravity configuration and the frequency agrees for run 11. A lower frequency is predicted

for run 36. The reason for this discrepancy is not clear, particularly in view of the excellent agreement for the other three runs.

Figures 18 and 19 show a direct comparison of the measured and calculated transient response characteristics for a cyclic pitch pulse input. The agreement in general is very good. In particular, the amplitude of the roll response predicted agrees very well with the measured value. The theoretical pitch response exhibits a smaller amplitude than the measured response, however, the overall agreement is very good. Thus, the theoretical approach presented here gives a good prediction of the vehicle transfer functions.

CONCLUSIONS

Based upon the analytical and experimental research program reported herein the following conclusions are made:

- 1.) The Froude scaled model of the AEROCRANE vehicle can be flown by a remote pilot in hovering with a reasonable level of effort. Remote piloting in hovering flight was made considerably easier by incorporation of a relatively simple attitude feedback system. This feedback system stabilizes or improves the damping of the unstable or lightly damped mode characteristic of the AEROCRANE in hovering.
- 2.) In forward flight the natural damping of this mode increases and no difficulties were encountered controlling the vehicle in trimmed forward flight without the stabilization system.
- 3.) Accurate quantitative data on the trim and dynamic stability characteristics of the model were obtained from remotely-piloted flight tests in a protected environment.
- 4.) The theoretical model for the forward flight trim characteristics of the AEROCRANE predicts the measured experimental data with a minor adjustment in the spherical centerbody drag coefficient.
- 5.) The analytical model of hover dynamic stability characteristics correlates very well with the measured model transient response indicating that the analytical model provides a good representation of the transfer functions of the vehicle.

REFERENCES

1. Putman, W. F. and Curtiss, H. C., Jr.: "An Analytical and Experimental Investigation of the Hovering Dynamics of the AEROCRANE Hybrid Heavy Lift Vehicle", Princeton University AMS Technical Report No. 1291, June 1976.
2. Coleman, R. P., et. al.: "Evaluation of the Induced Velocity Field of An Idealized Helicopter Rotor", NACA Wartime Report ARR No. 15E10, June 1945.
3. Gessow, A. and Myers, G. C.: AERODYNAMICS OF THE HELICOPTER. The MacMillan Company, New York, 1952.
4. Goldstein, S.: "Modern Developments in Fluid Dynamics", Vol. II, Dover Publications, New York, 1965.

TABLE I
SUMMARY OF MODEL PHYSICAL CHARACTERISTICS

ROTOR DIAMETER		39.9 ft.
SPHERE DIAMETER		18.2 ft.
MODEL WEIGHT (W_o)	Low c.g.	177 lbs.
	High c.g.	192 lbs.
CENTER OF GRAVITY		
POSITION (r_o)	Low c.g.	2.71 ft.
	High c.g.	1.83 ft.
MOMENTS OF INERTIA		
I' (pitch and roll)*	Low c.g.	521 slug-ft ²
	High c.g.	576 slug-ft ²
I_z		653 slug-ft ²
RUNNING WEIGHT OF UMBILICAL CABLE		0.61 lb/ft

* Determined by experiment and include virtual mass effects.

TABLE II

SUMMARY OF HOVER TEST CONDITIONS

RUN NO.	W_O lb.	r_O ft.	W_{SL} lb.	W_C lb.	W lb.	T lb.	F_B lb.	T/W	COMMENTS
8	177	2.71	41	49	267	52	215	0.19	Cyclic Inputs, $\gamma = 45^\circ$, Sling Load
9			67	49	293	76	217	0.26	
10				48	292	75	217	0.26	
11				55	299	89	210	0.30	
15	192	1.83	20	46	258	52	206	0.20	
16			42	46	280	80	200	0.29	
17				49	283	84	199	0.30	
18					283	84	199	0.30	
19	177	2.71	41		267	65	202	0.24	
24			41	53	271	63	208	0.23	Collective Inputs
36			51	37	265	64	201	0.24	Cyclic Inputs
52			44	52	273	65	208	0.24	" , $\gamma = 30^\circ$, 45° , & 60°
53*		4.23*	44*		273	63	208	0.30	Ballast Rigidly Attached, $\gamma = 45^\circ$
54		2.71	51		280	78	202	0.28	Sling Load, $\gamma = 45^\circ$, 180° , & 225°
55									" "
56									" $\gamma = 180^\circ$

*NOTE: Ballast is rigidly attached to gondola base. No sling load is used.

$$W = W_O + W_{SL} + W_C$$

TABLE III

SUMMARY OF FORWARD FLIGHT TRIM CONDITIONS

RUN NUMBER	TRIM SPEED ft./sec.	GROSS WEIGHT W, lbs.	SAS GAIN K_A , deg/deg. $W_C + W_{sl}$	LOAD lb.	PITCH ANGLE θ , deg.	ROLL ANGLE ϕ , deg.	LONG. CYCLIC A_{1s} , deg	LAT. CYCLIC B_{1s} , deg.	TYPE RUN
21	5.5	273	0.3	96	-8.5	-5.5	-3.1	2.6	Trim
22	5.8	273		96	-11.4	-3.9	-5.1	2.3	
26	5.6	281		104	-16.6	-4.7	-5.4	4.4	
28	7.2	257		80	-17.7	-6.2	-5.6	4.5	
31	10.8	263		86	-22.2	-4.9	-7.7	6.1	
32	10.5	272		95	-28.0	-5.8	-8.0	6.6	
33	11.8	267		90	-30.9	-10.8	-10.8	9.4	
34	6.3	293		116	-10.2	-4.5	-4.5	4.1	
35	12.5	287		110	-31.2	-17.2	-9.1	10.3	
37	8.5	279		102	-21.1	-8.5	-3.9	7.2	
42	5.4	282	0.3	105	-10.7	-6.4	-3.9	3.9	Transient Response
43	4.6	282	0	105	-9.1	-9.8	-4.1	3.5	
44	9.5	283	0.2	106	-20.2	-13.3	-5.1	9.3	
45	9.3	289	0	112	-18.3	-10.0	-6.0	7.1	
46	9.3	285	0	108	-17.2	-6.0	-4.8	5.4	
47	7.6	268	0.3	91	-12.1	-9.1	-4.5	5.6	
48	5.3	268	0	91	-10.0	-3.8	-4.0	3.4	
49	6.8	270	0.3	93	-14.2	-7.2	-5.3	5.2	
50	8.4	265	0	88	-13.4	-5.1	-6.1	3.8	
51	8.4	272	0	95	-15.0	-6.0	-5.8	4.8	

NOTE: r_o = 2.71 ft. all Forward Flight Runs. w_o = 177 lb. " " " " (W = $w_o + w_c + w_{sl}$) I' = 521 slug-ft² all Forward Flight Runs. I_z = 653 slug-ft² " " " "

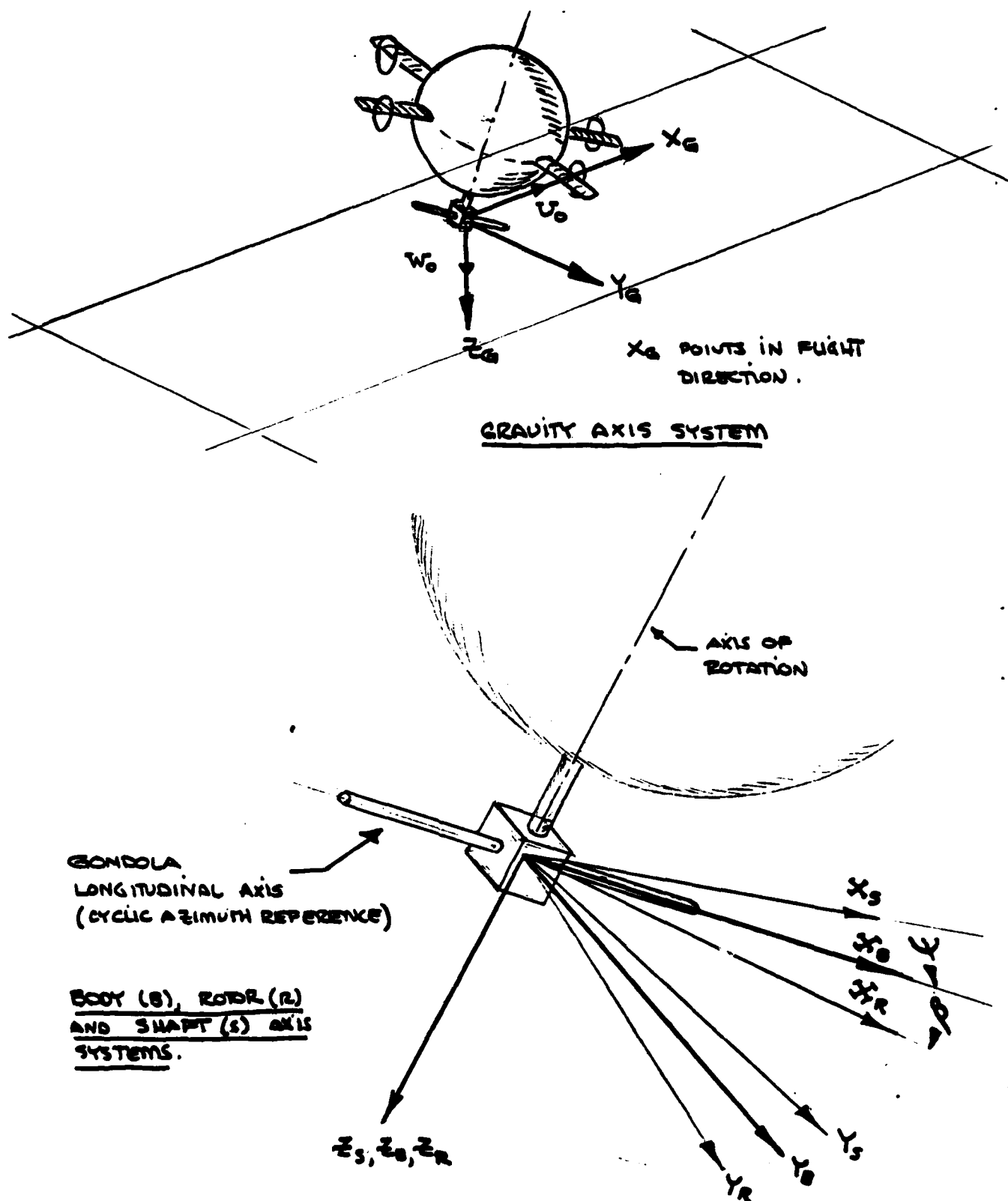


Figure 1. Axis Systems Used for Analytical Model.
(a) Gravity, Body, Rotor and Shaft Systems.

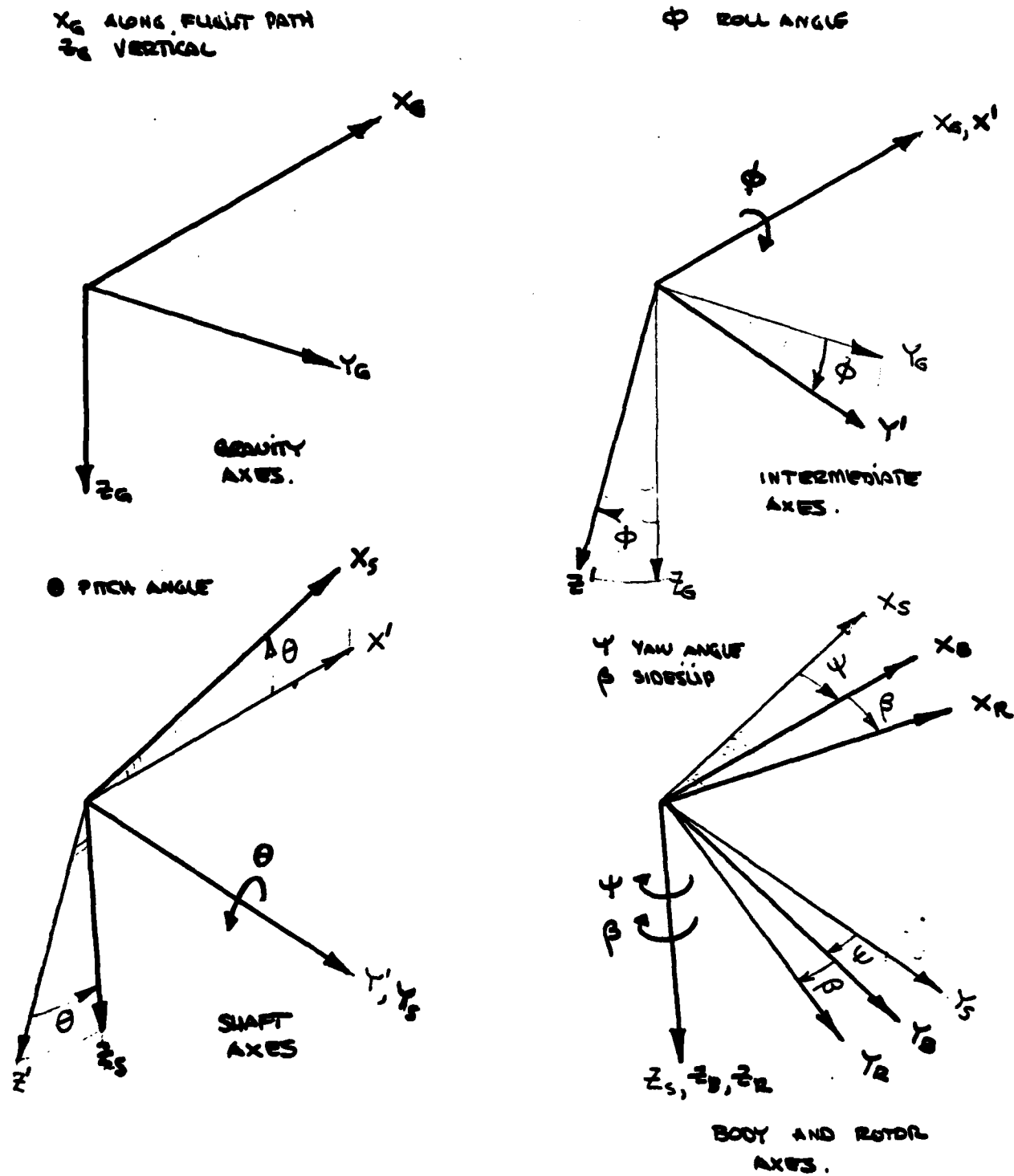


Figure 1. Continued.
(b) Ordered Rotations.

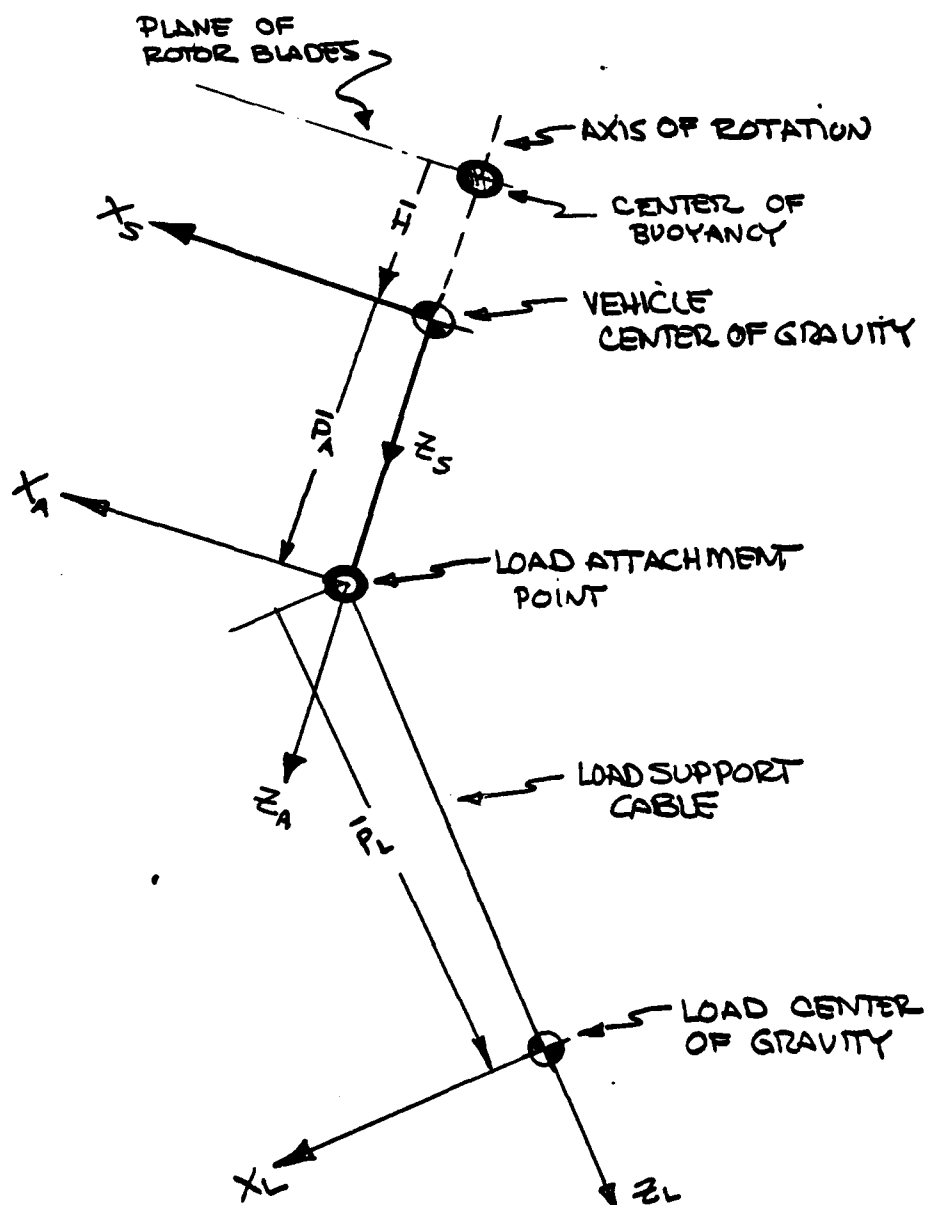


Figure 1. Continued.
(c) Load and Attachment Point Systems.

EXTERNAL
FORCES AND
MOMENTS
ACTING ON
VEHICLE

FORCE
APPLIED
TO
VEHICLE
BY LOAD

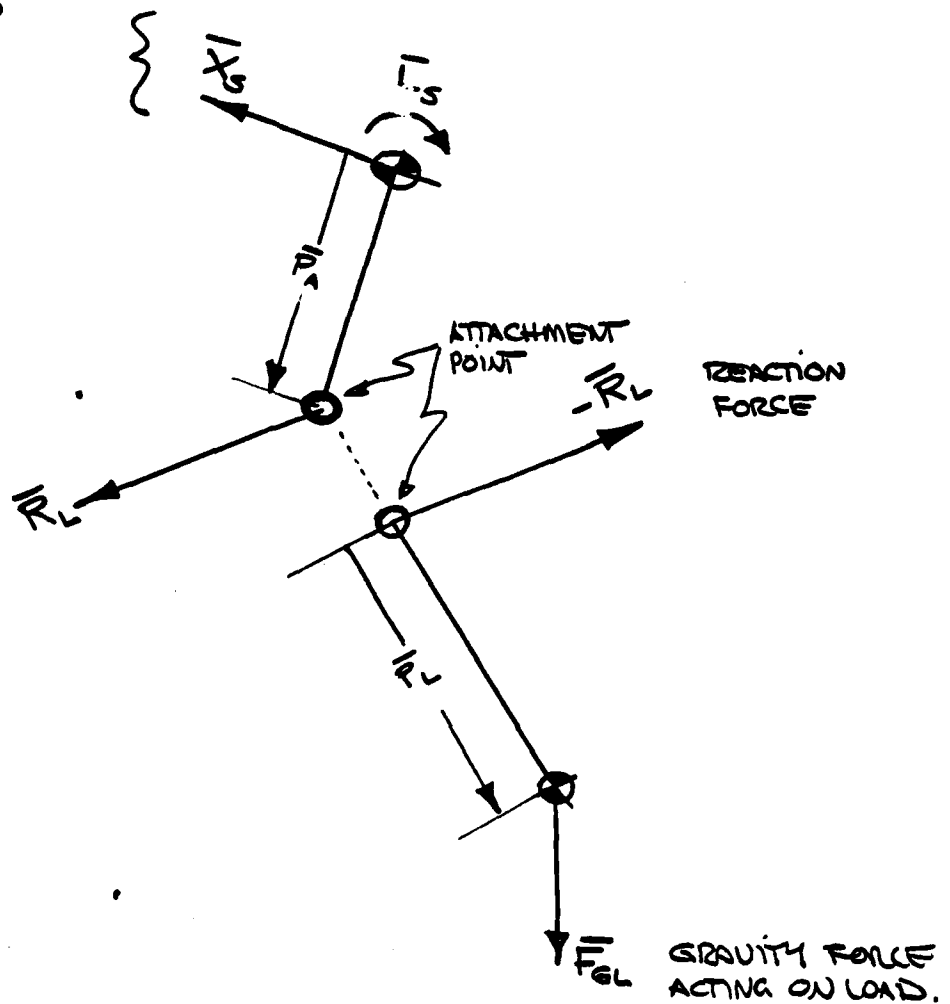


Figure 1. Continued.
(d) Model and Sling Load Free Body Diagram.



Figure 2. AEROCRANE Model with Jettisonable Ballast Package.

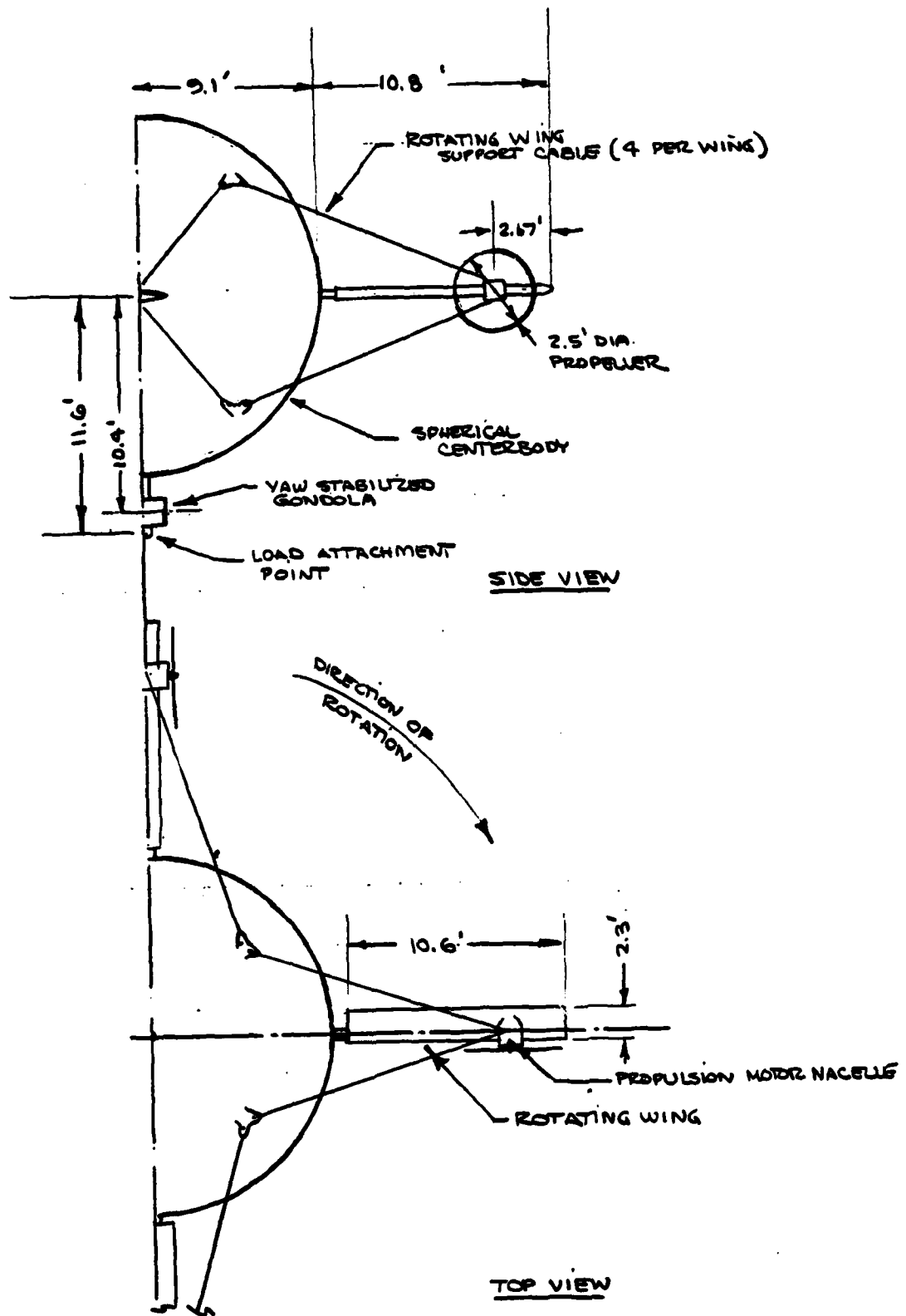


Figure 3. General Arrangement Drawing of AEROCRANE Model.

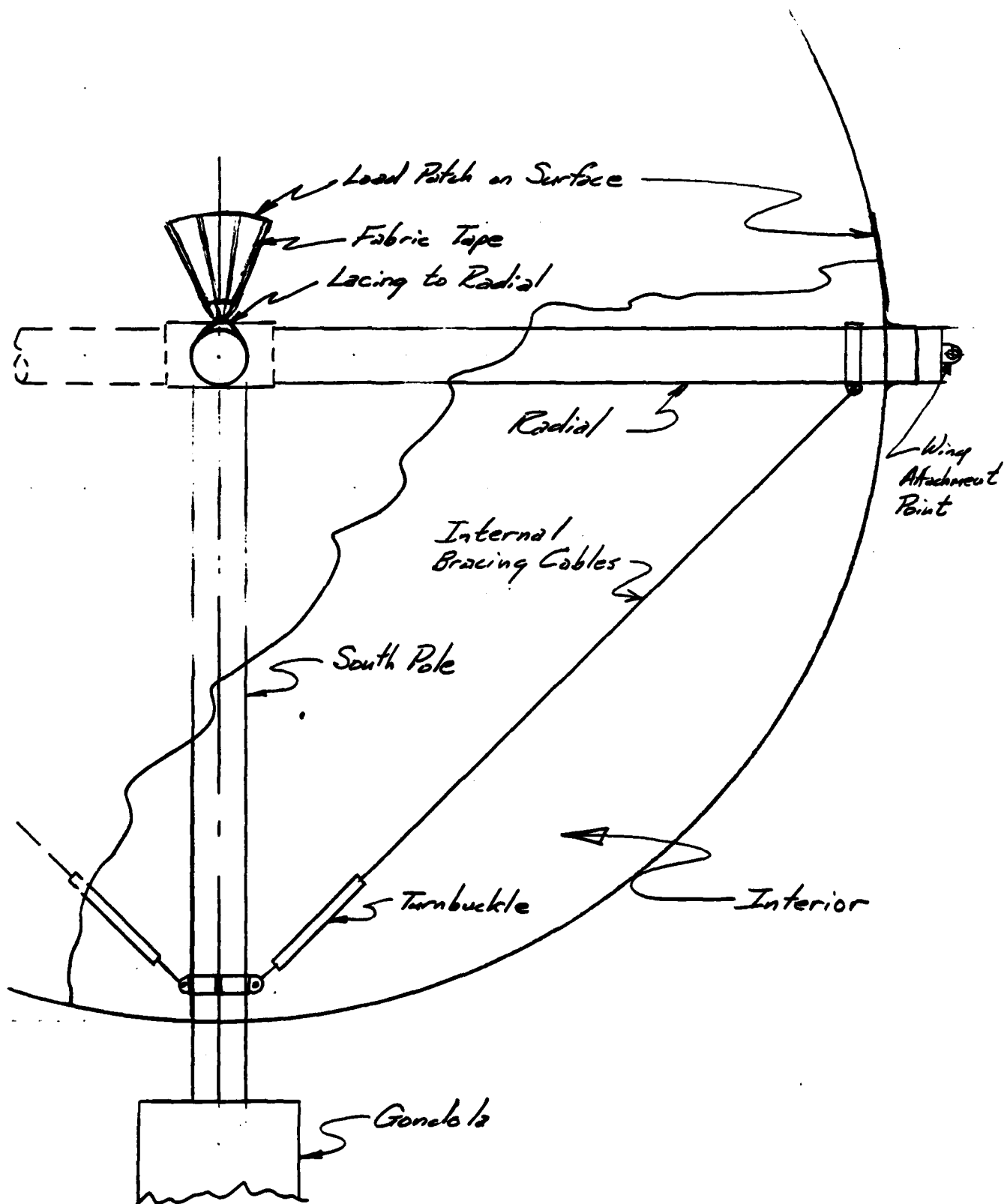


Figure 4. Schematic Drawing of Model Structural Modifications.

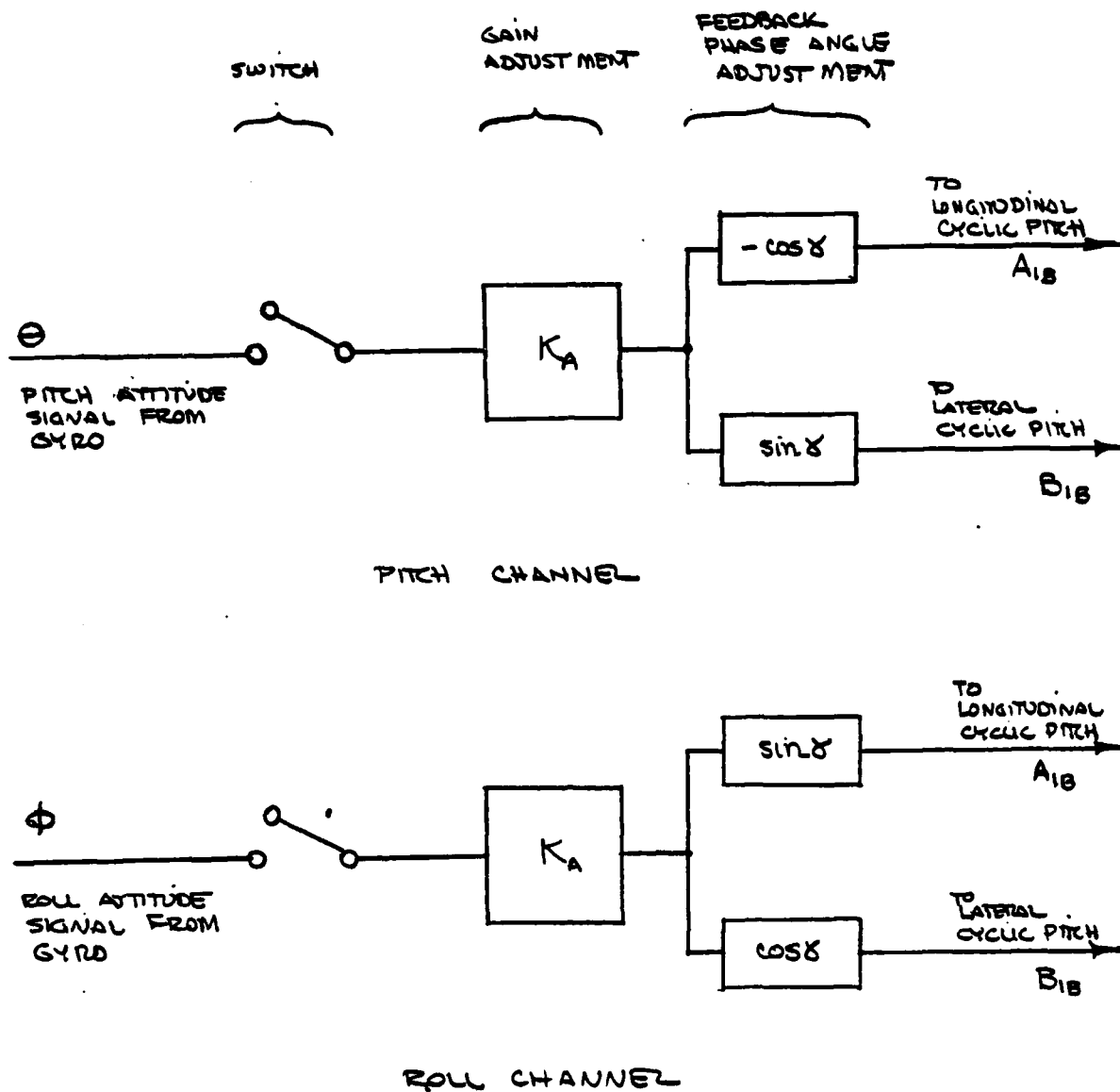
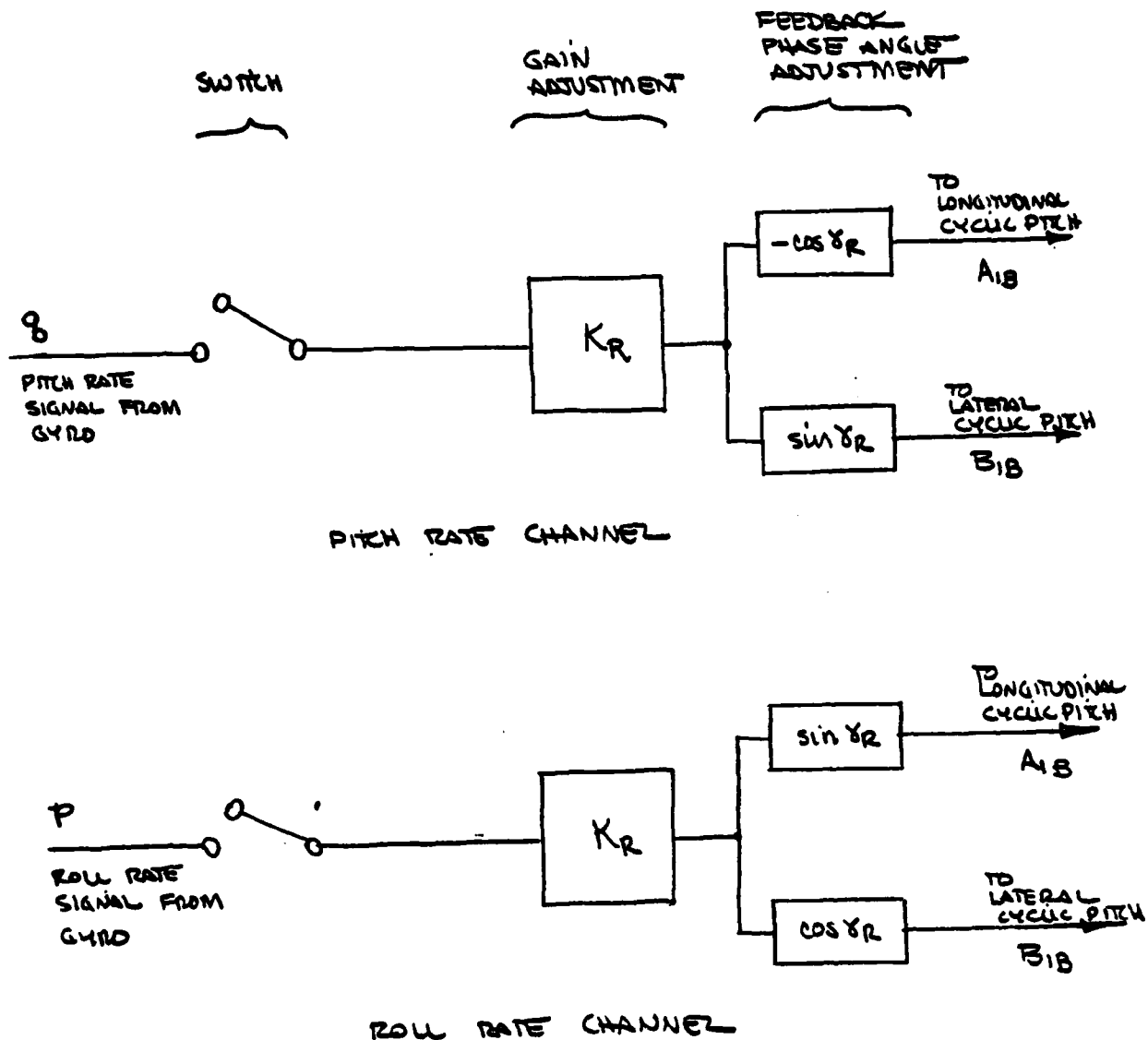


Figure 5. Schematic of Attitude Stability Augmentation System.



NOTE: SYSTEM INSTALLED IN
MODEL BUT NOT
USED IN EXPERIMENTS

Figure 6. Schematic of Angular Rate Stability Augmentation System.

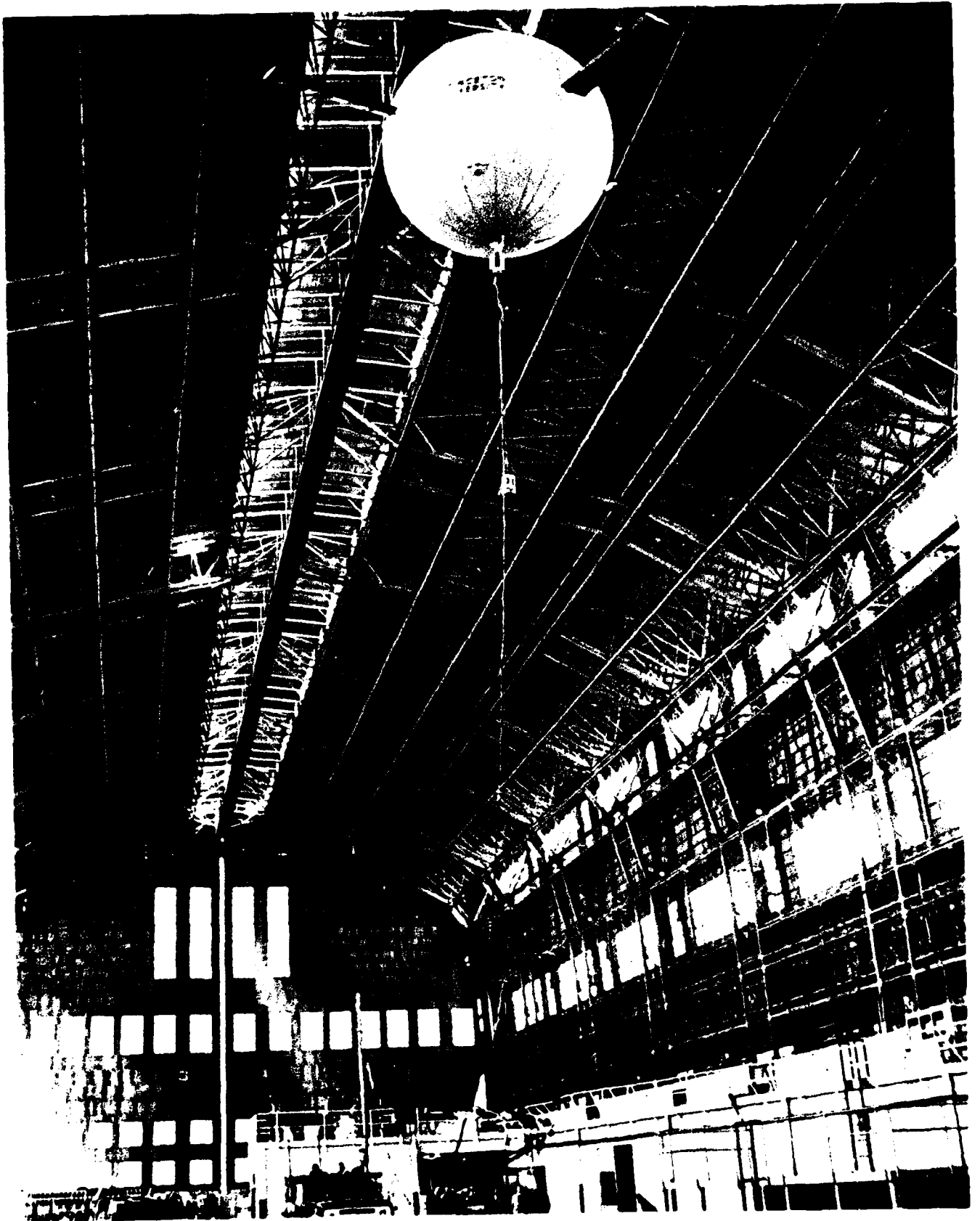


Figure 7. AEROCRANE Model in Hovering Flight.



Figure 8. Test Crew Arrangement.

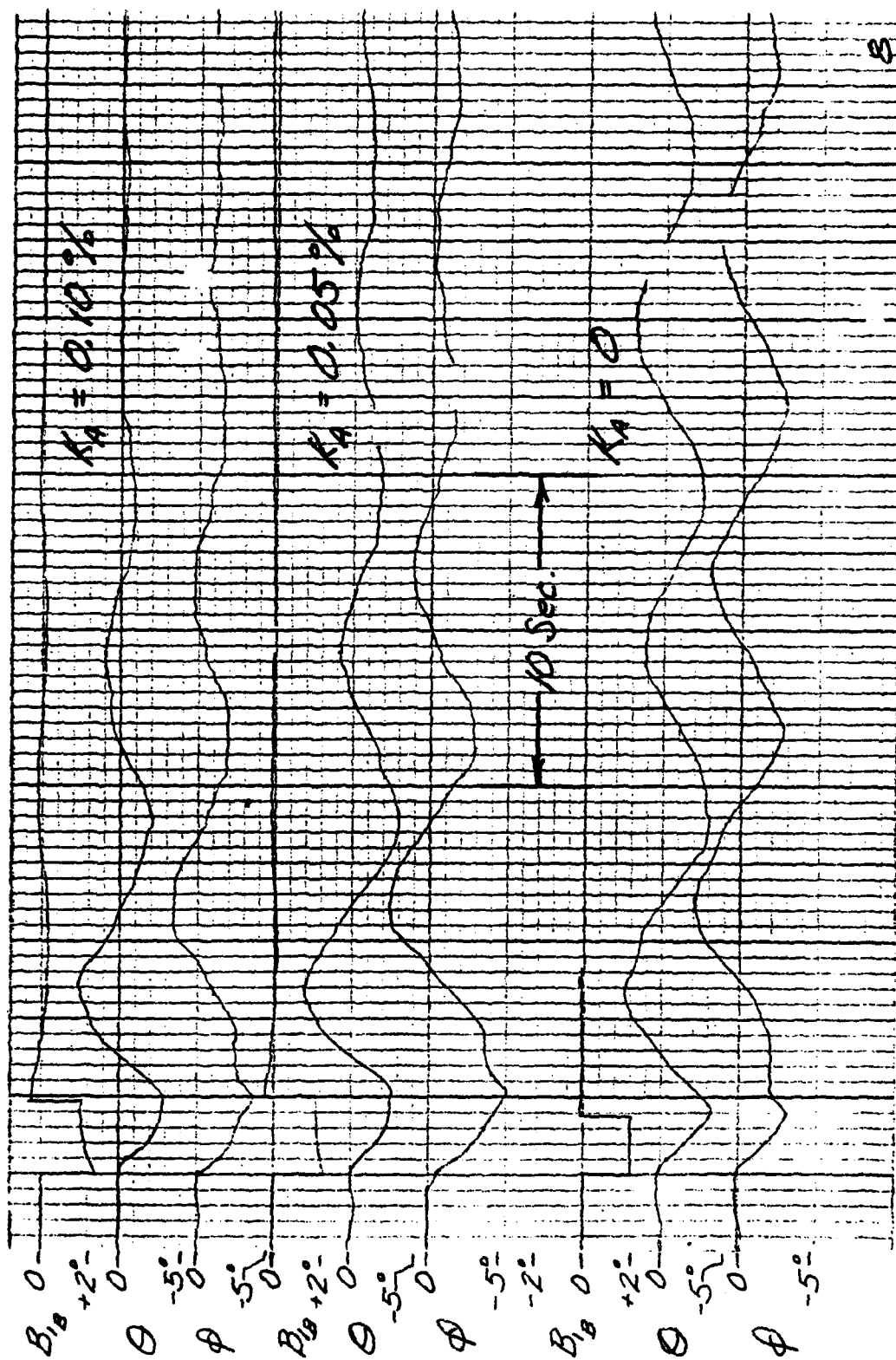
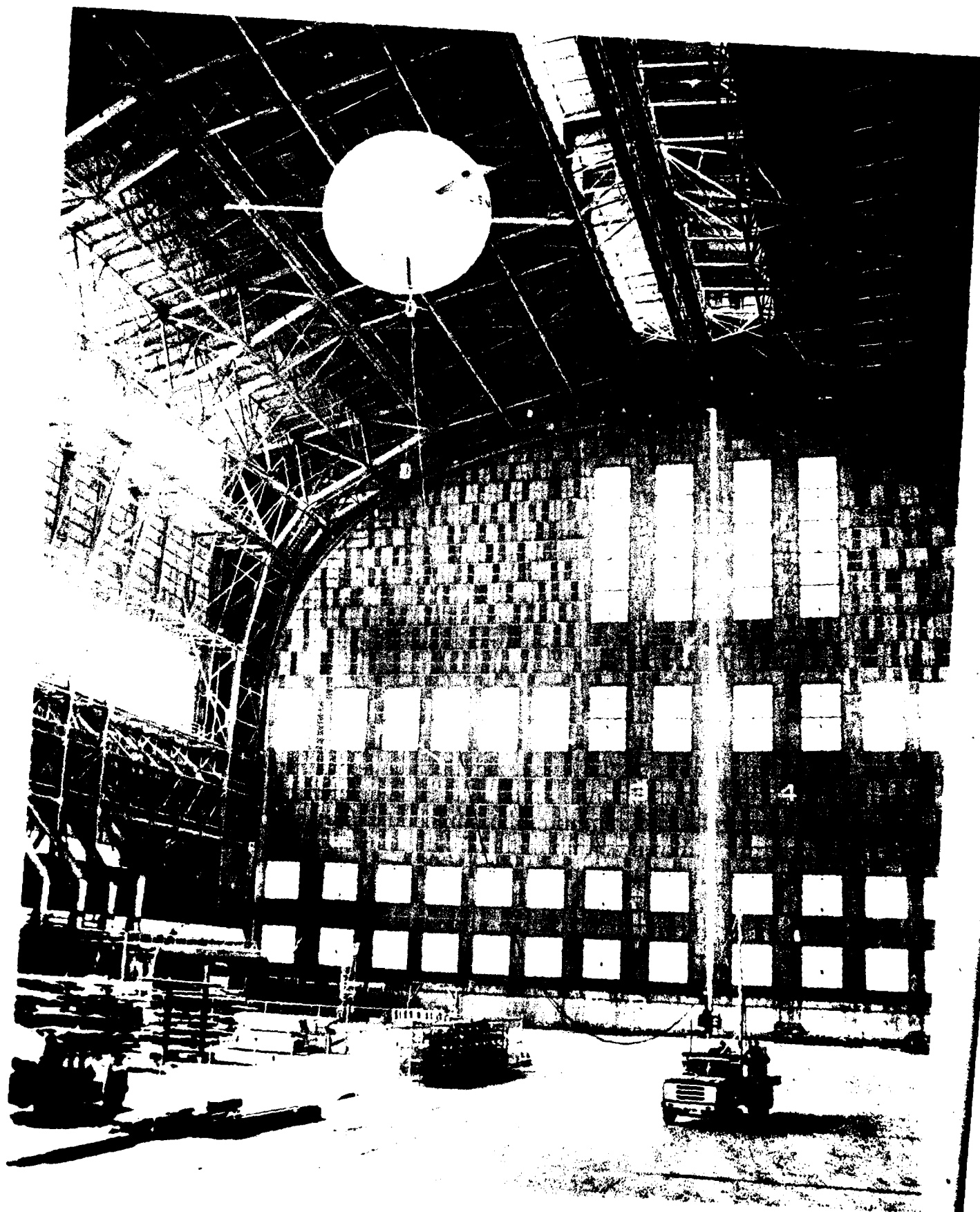


Figure 9. Hovering Transient Responses, Run No. 8.



Arrangement of Test Apparatus for Forward
Flight Experiments; Beginning Run.

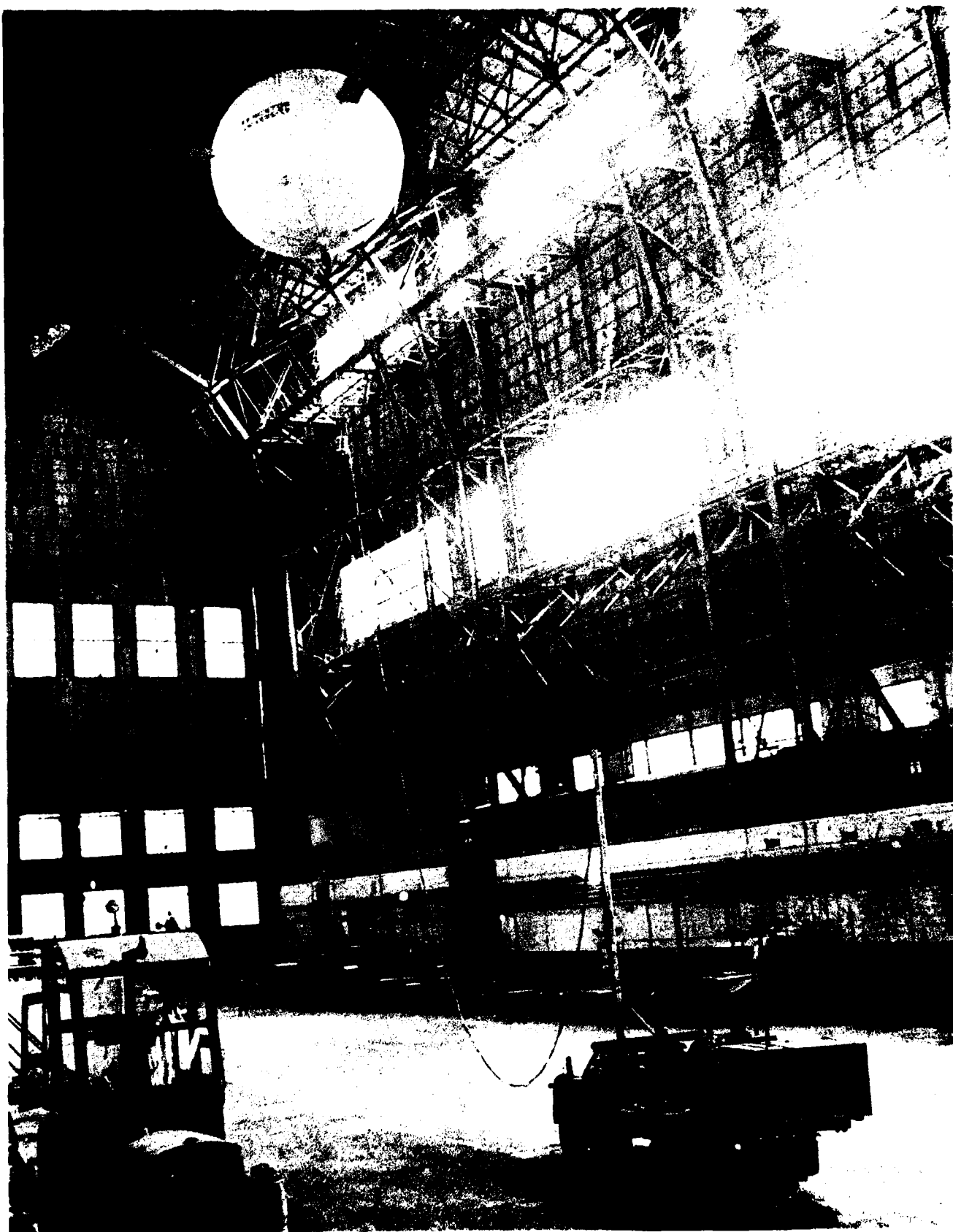


Figure 11. Arrangement of Test Apparatus for Forward Flight Experiments; End of Run.

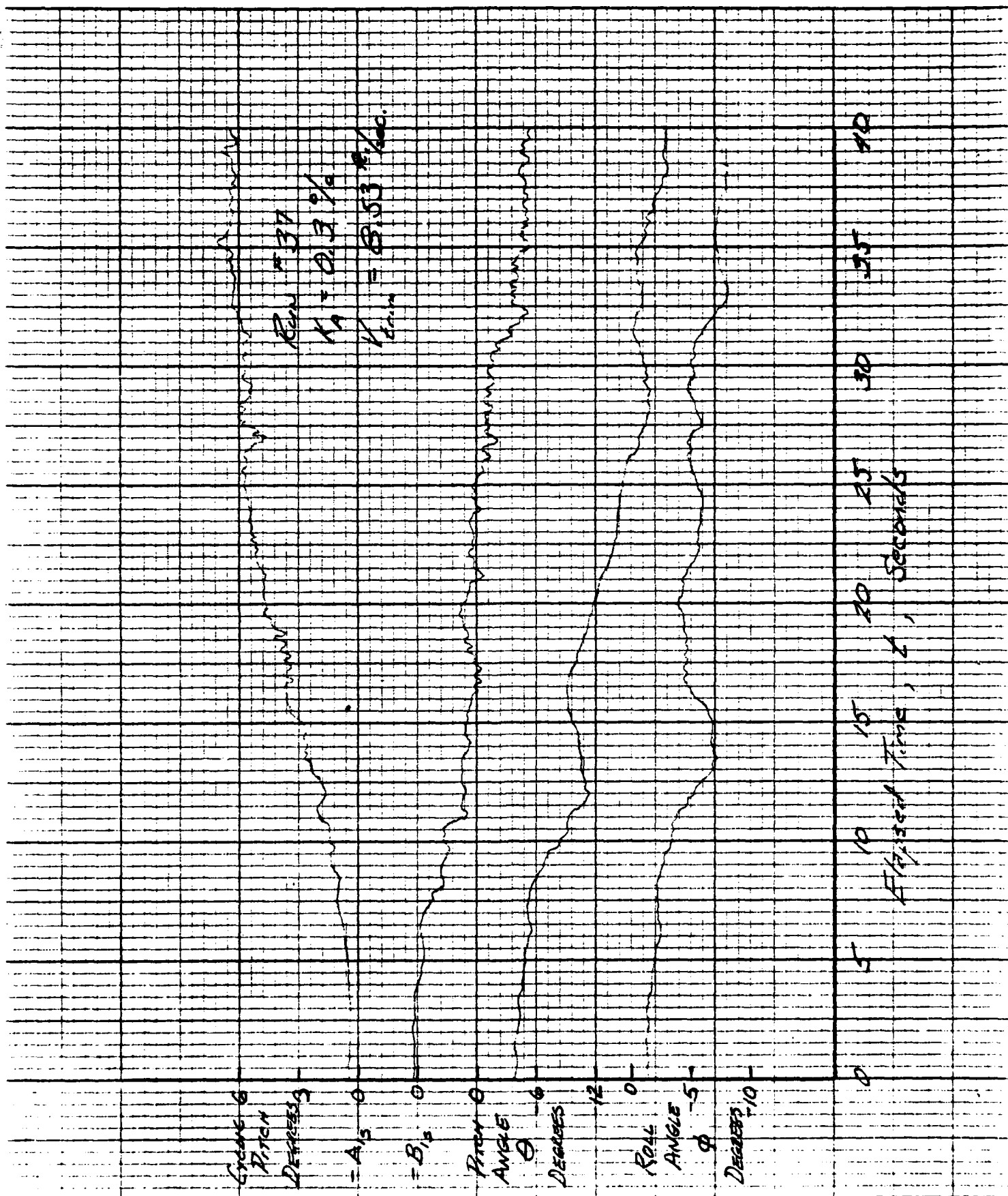


Figure 12. Typical Transition Time History.

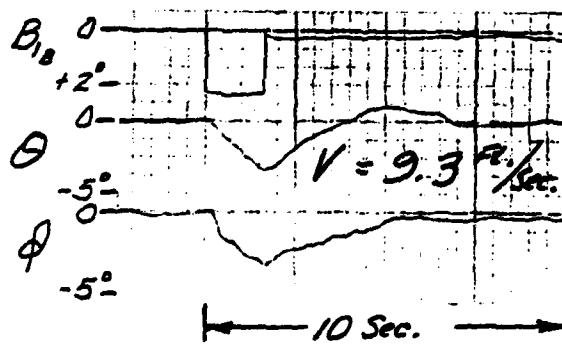
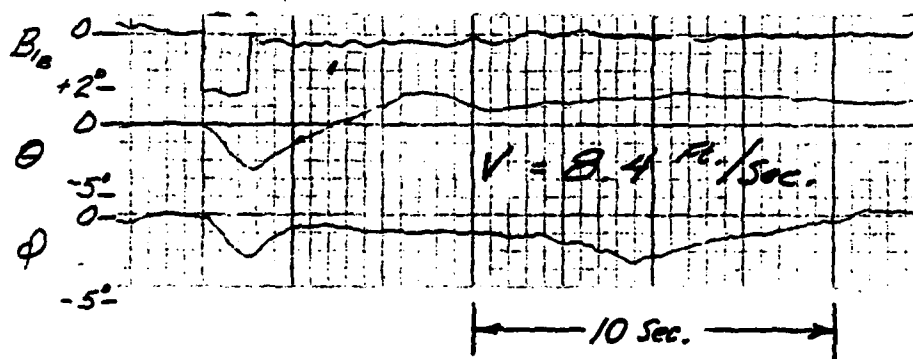
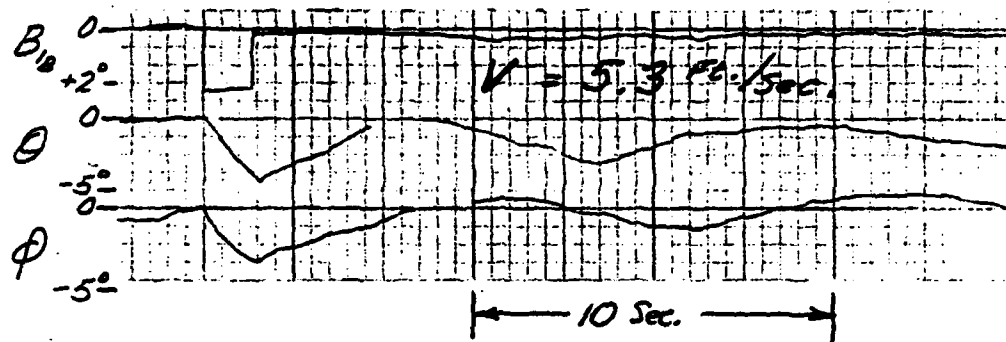
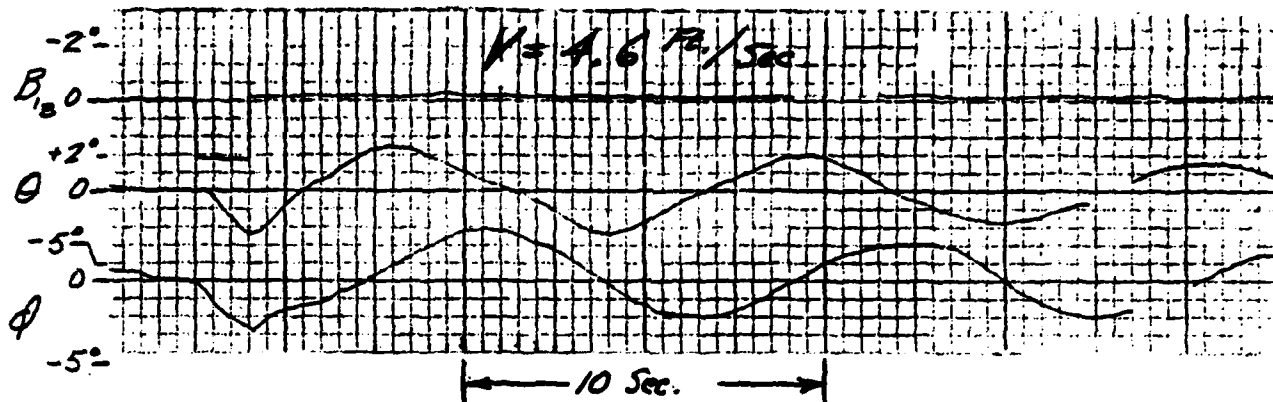


Figure 13. Typical Forward Flight Transient Response Time Histories. $K_A = 0$.

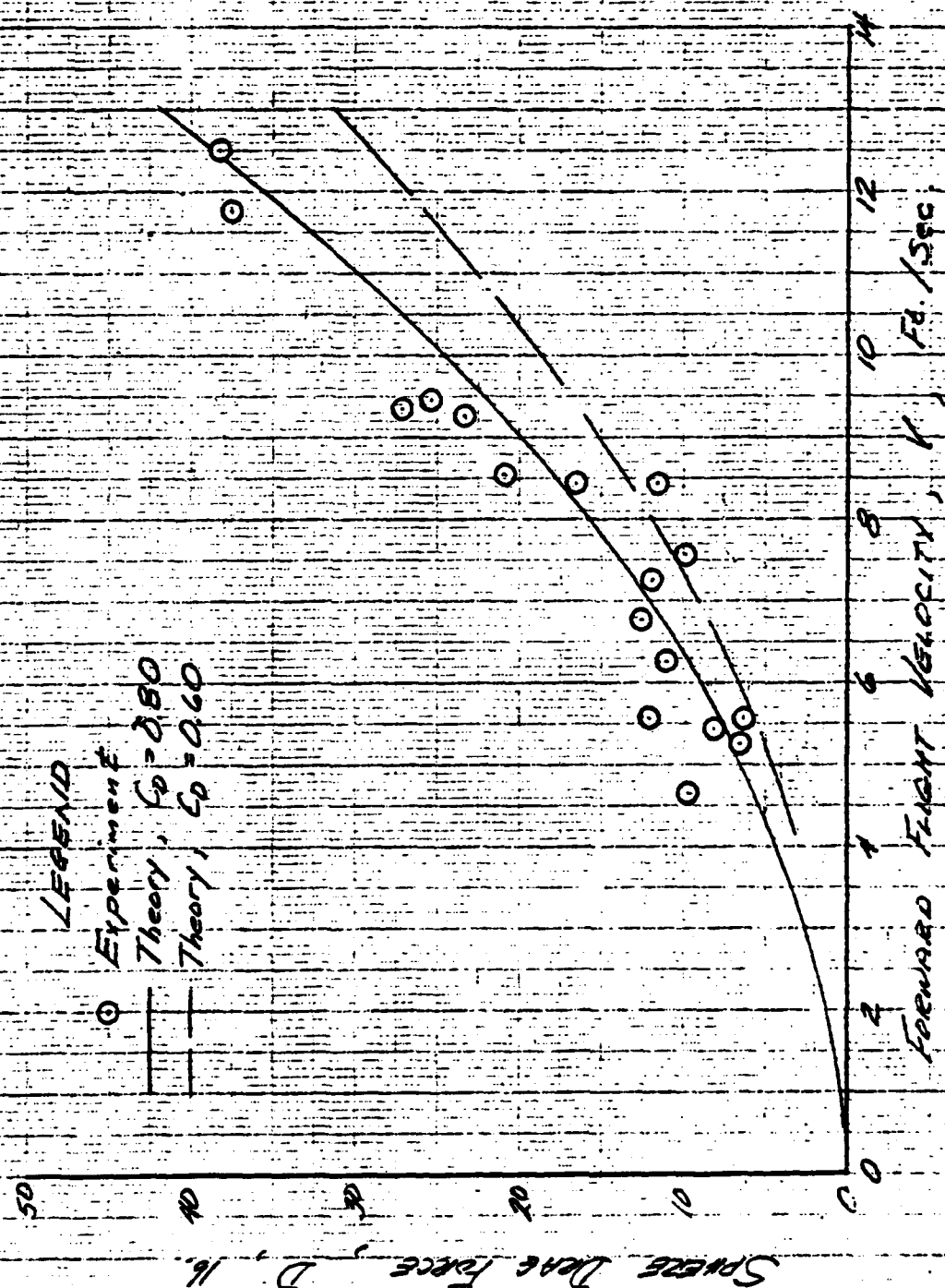


Figure 14. Trim Force Conditions, Comparison of Experiment and Theory: Sphere Drag.

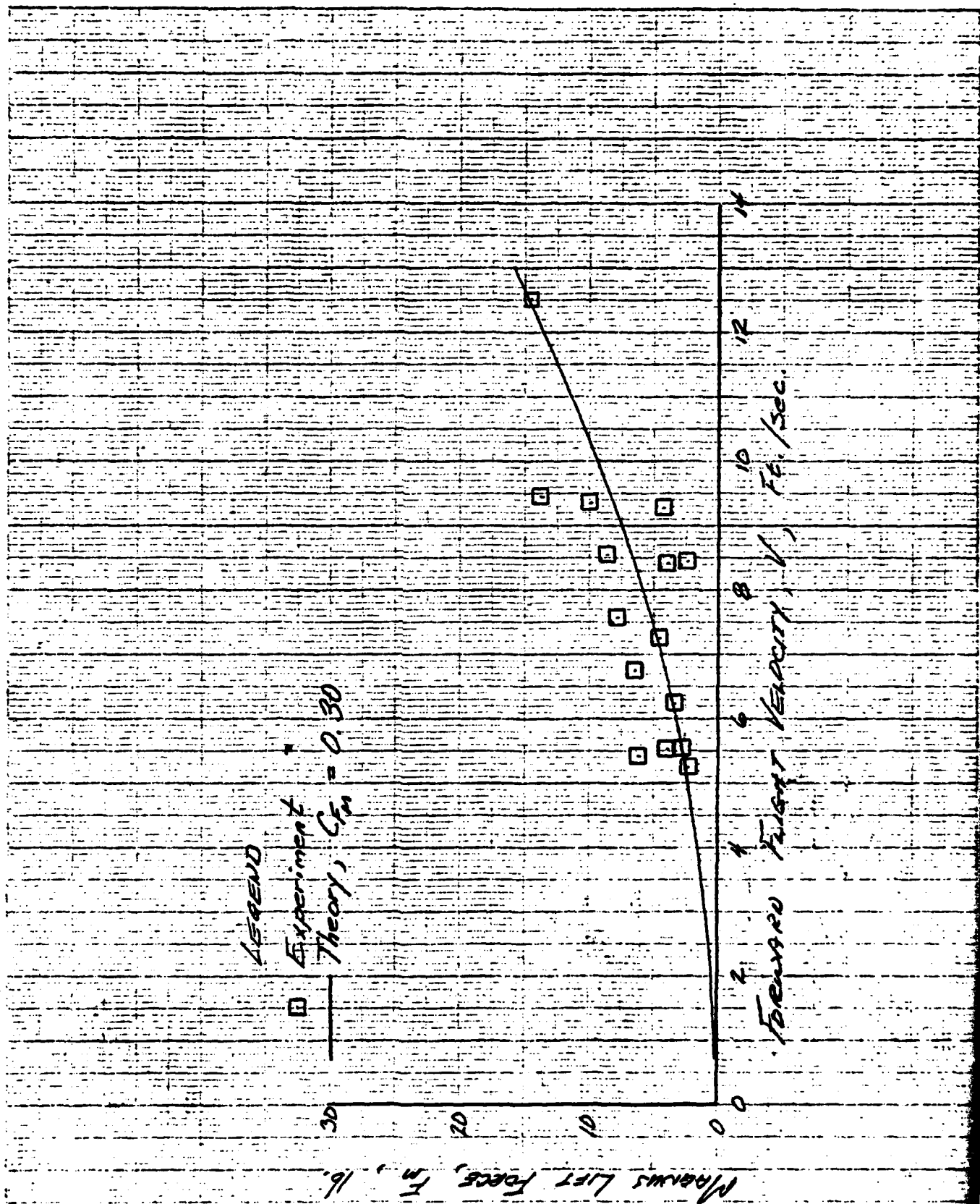


Figure 15. Trim Force Conditions, Comparison of Experiment and Theory: Magnus Lift Force.

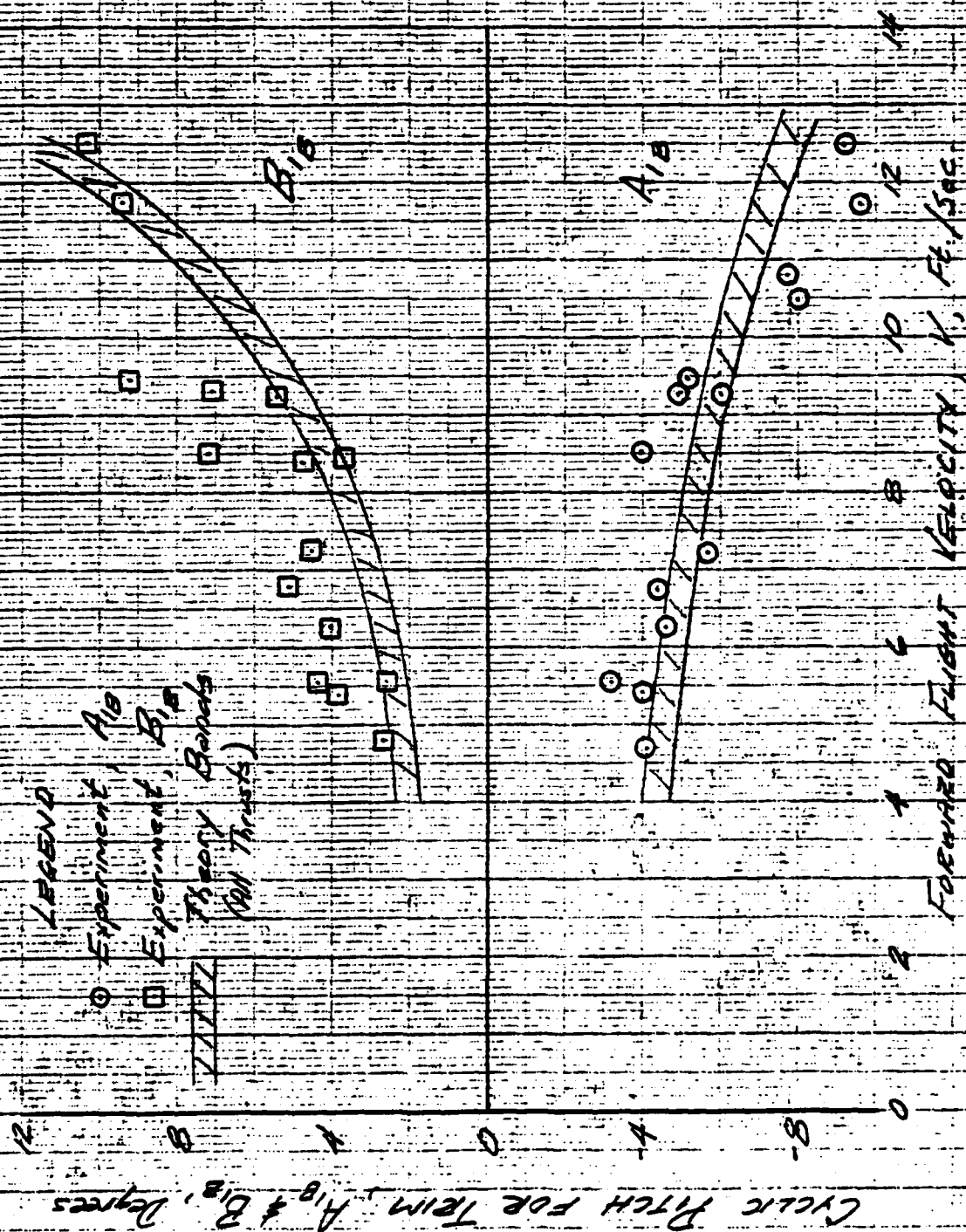


Figure-16. Trim Conditions, Comparison of Experiment and Theory: Longitudinal and Lateral Cyclic Pitch.

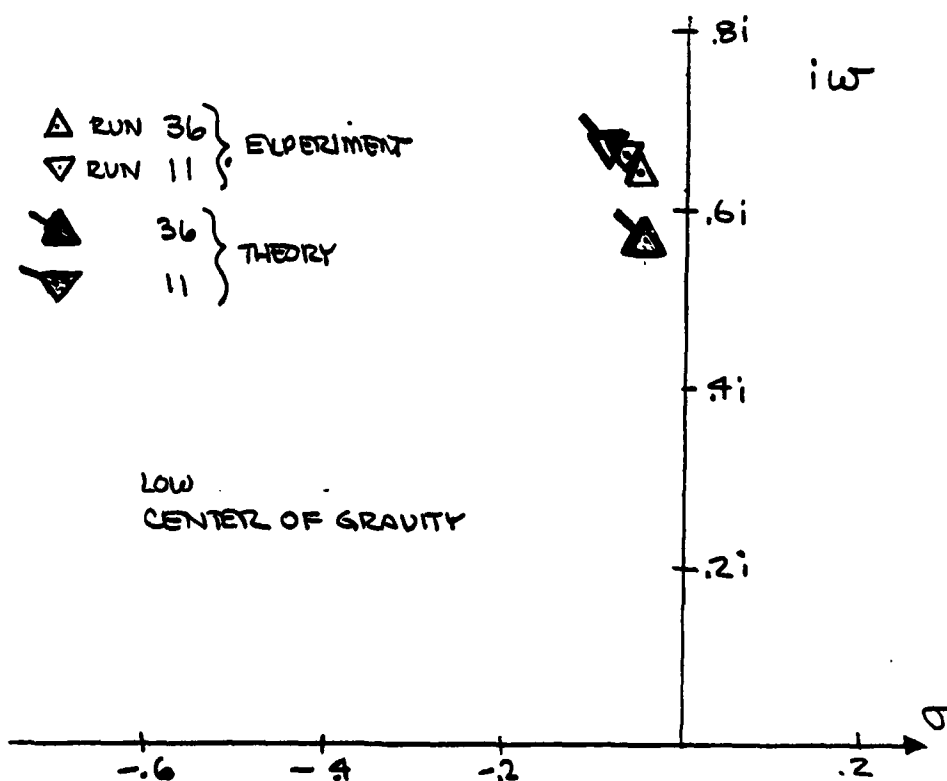
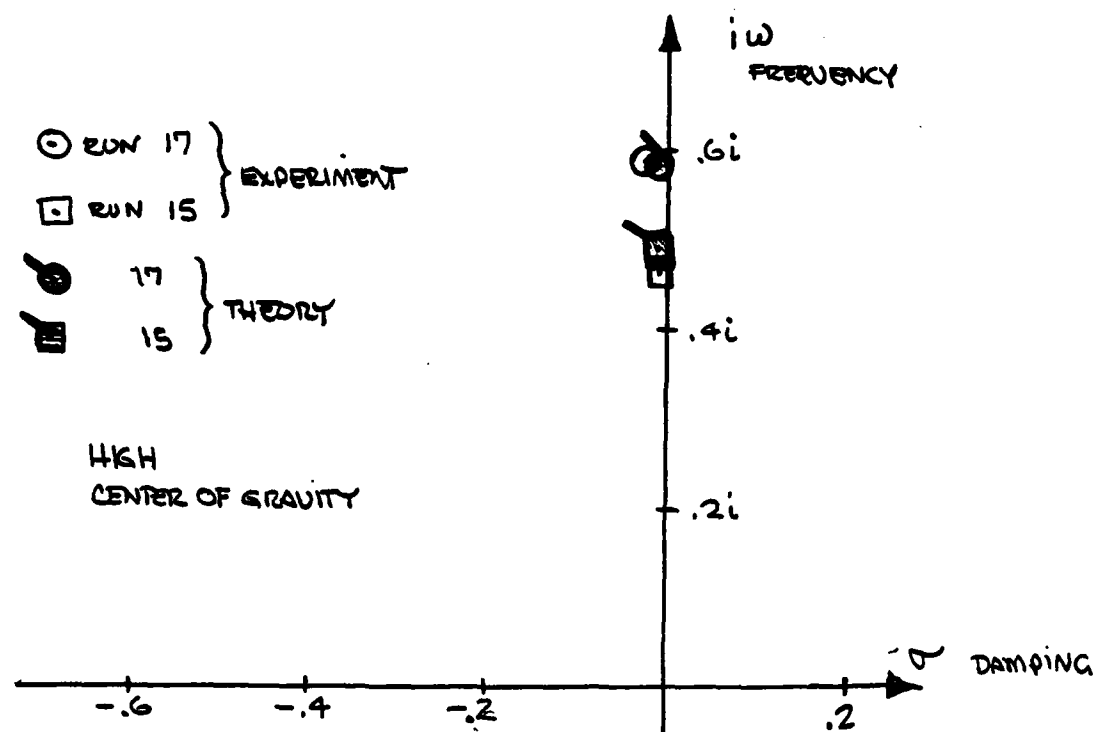


Figure 17. Period and Damping of Hovering Retrograde Oscillation, Comparison of Theory and Experiment.

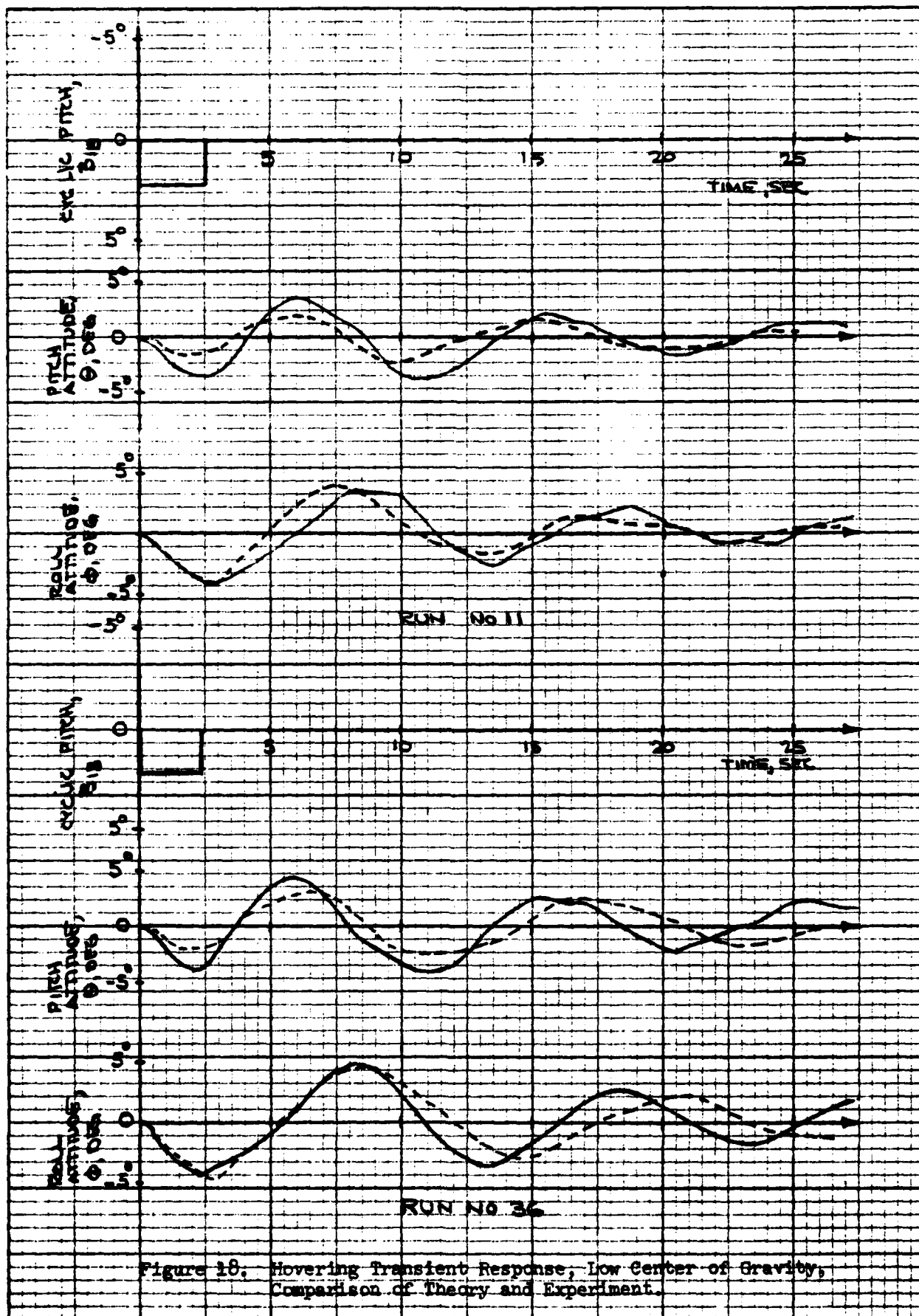


Figure 10. Hovering Transient Response, Low Center of Gravity, Comparison of Theory and Experiment.

NEWBERRY & LEPPEN CO.
1215 N. VINCENT ST.
CHICAGO, ILL.

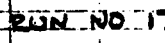


Figure 19. Hovering Transient Response, High Center of Gravity, Comparison of Theory and Experiment.

APPENDIX A

HOVERING TRANSIENT RESPONSE DATA

Figures A-1 through A-6 present hovering transient response data for the various flight conditions listed in Table II. The data in these figures are traced directly from the oscillograph records and include all higher frequencies contained in the original records. In particular, the one-per-revolution content, due in part to blade tracking irregularities, is preserved as faithfully as possible. For clarity only B_{1s} control time histories are shown. The other model controls, A_{1s} and θ_o , are constant during the time histories presented.

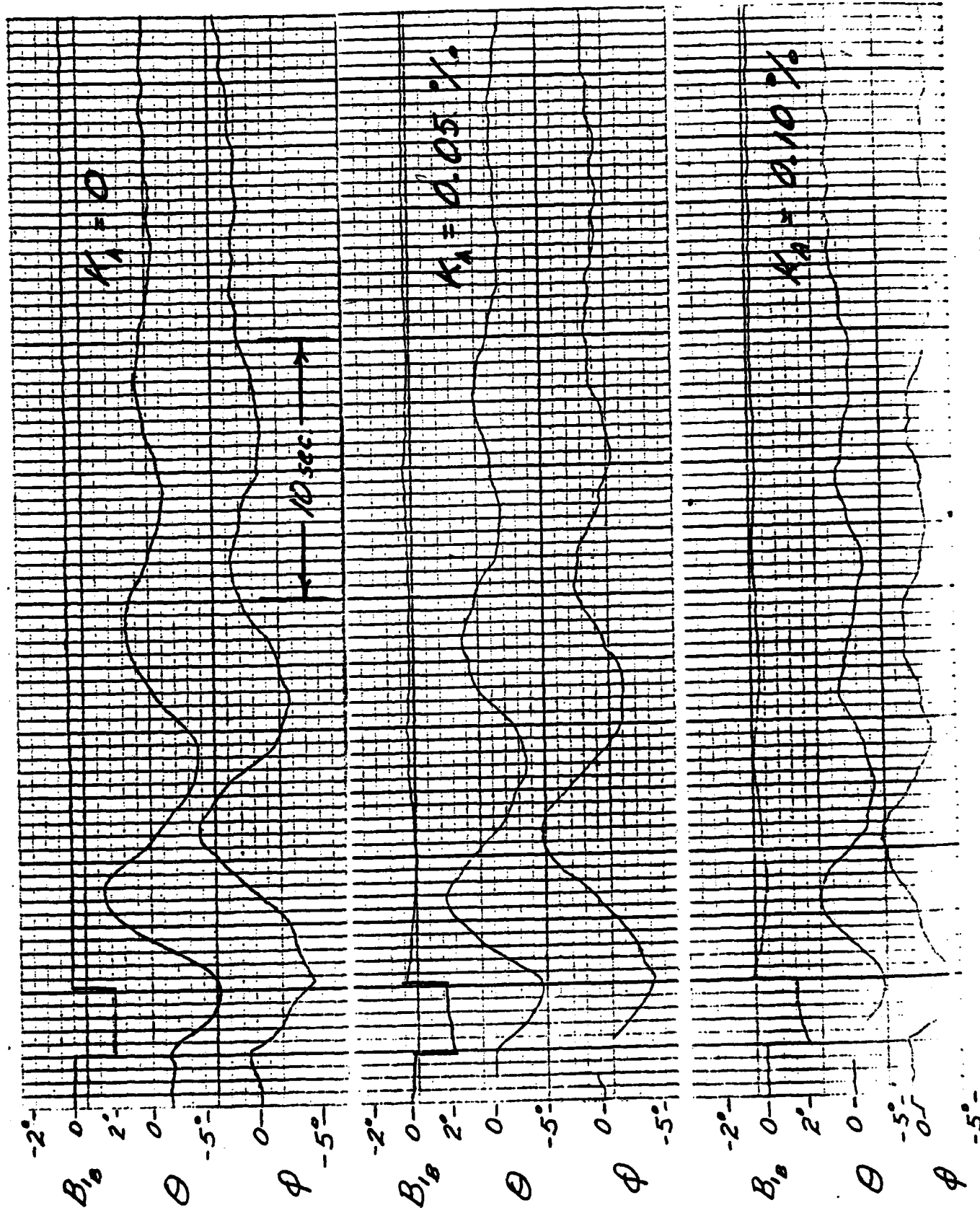


Figure A-1. Hovering Transient Responses, Run No. 10.

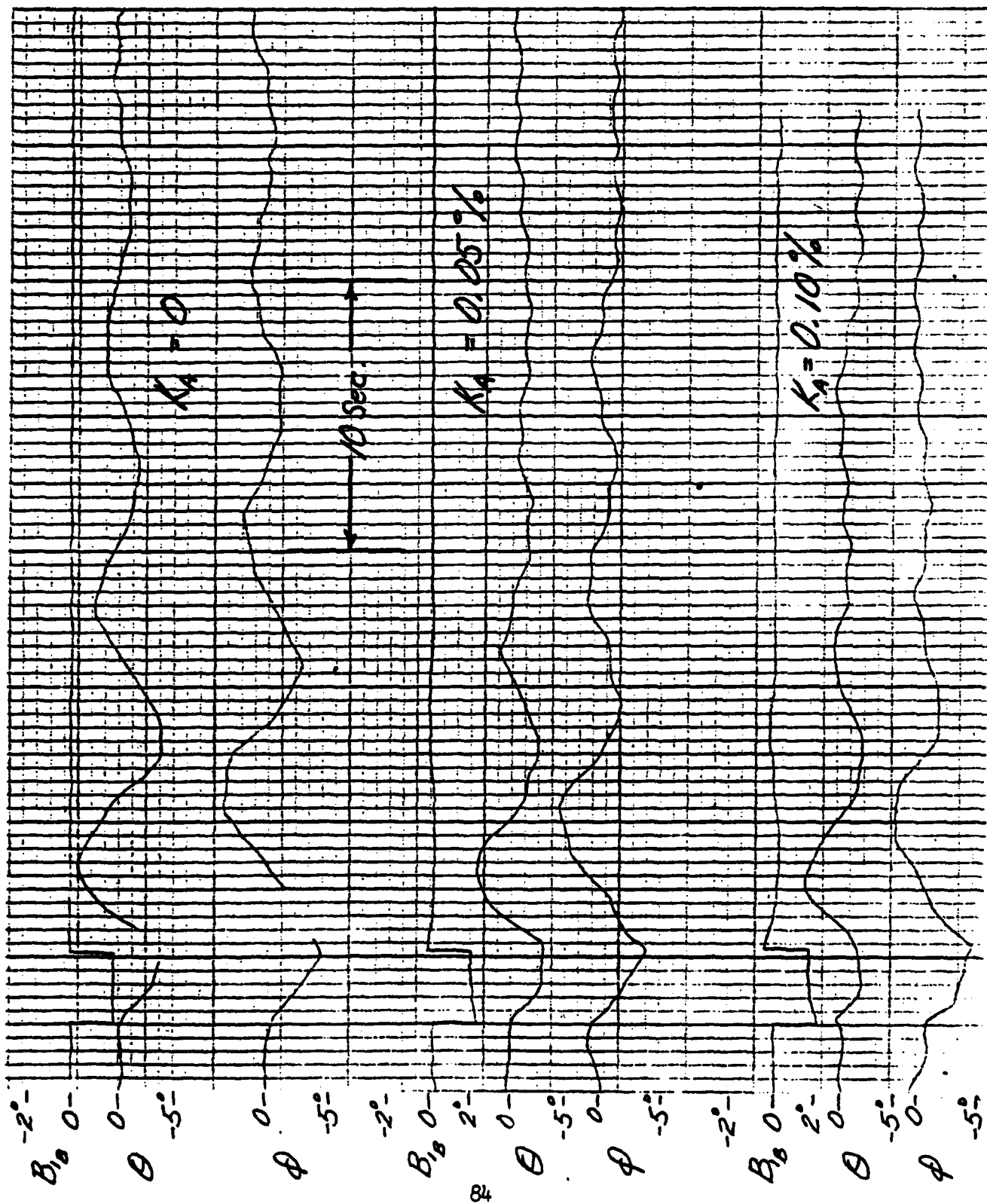


Figure A-2. Hovering Transient Responses, Run No. 11.

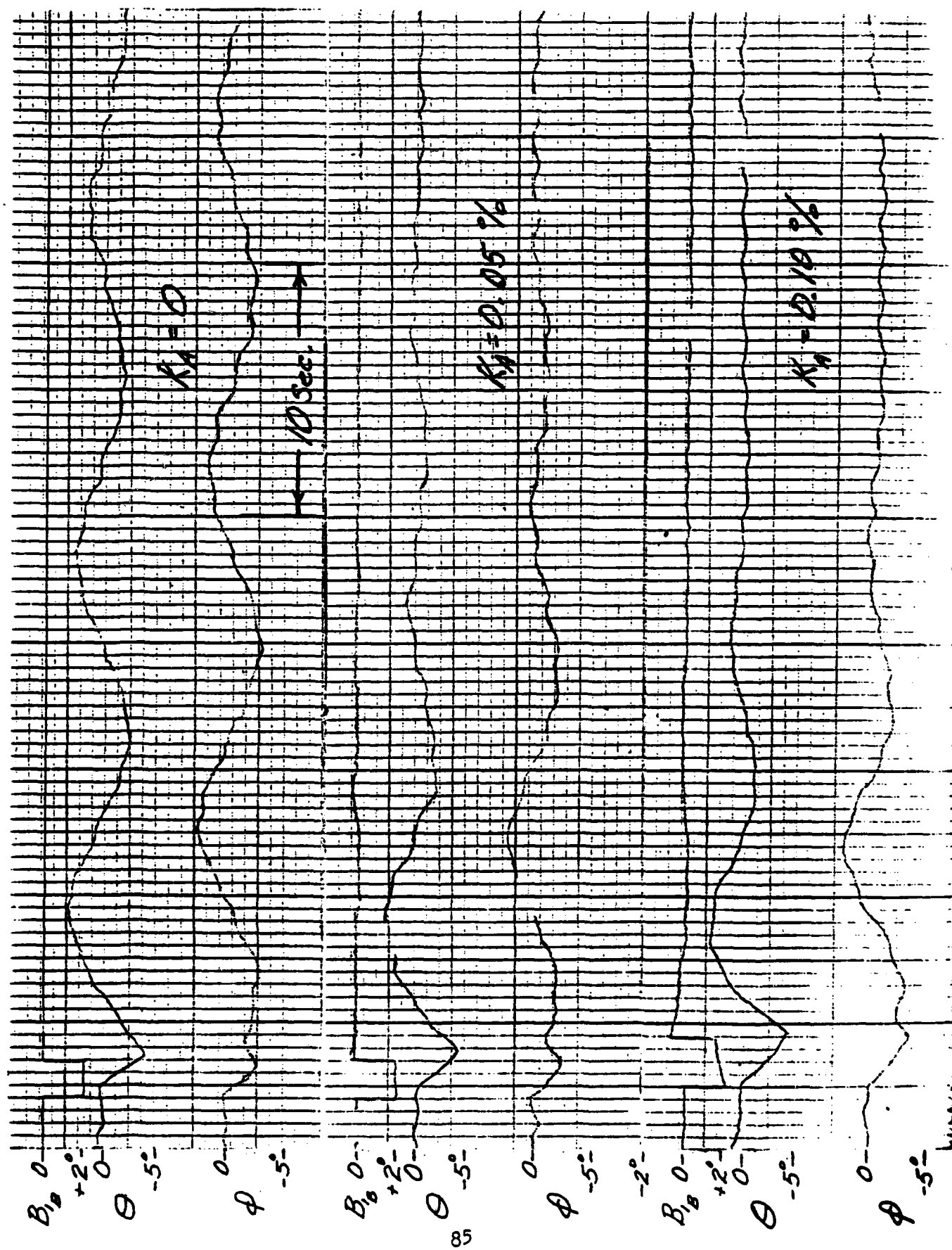


Figure A-3. Hovering Transient Responses, Run No. 15.

AD-A049 084

PRINCETON UNIV N J DEPT OF AEROSPACE AND MECHANICAL--ETC F/8 1/3
AN EXPERIMENTAL AND ANALYTICAL INVESTIGATION OF THE HOVERING AN--ETC(U)
SEP 77 W F PUTMAN; H C CURTISS N62269-76-C-0464

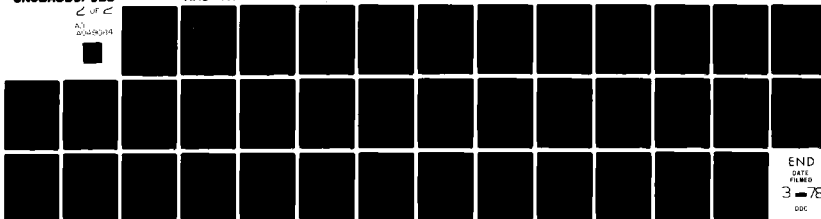
UNCLASSIFIED

AMS-TR-1351

NADC-76201-30

ML

2 of 2
AD-A049084



END
DATE
FILMED
3-78
DDC

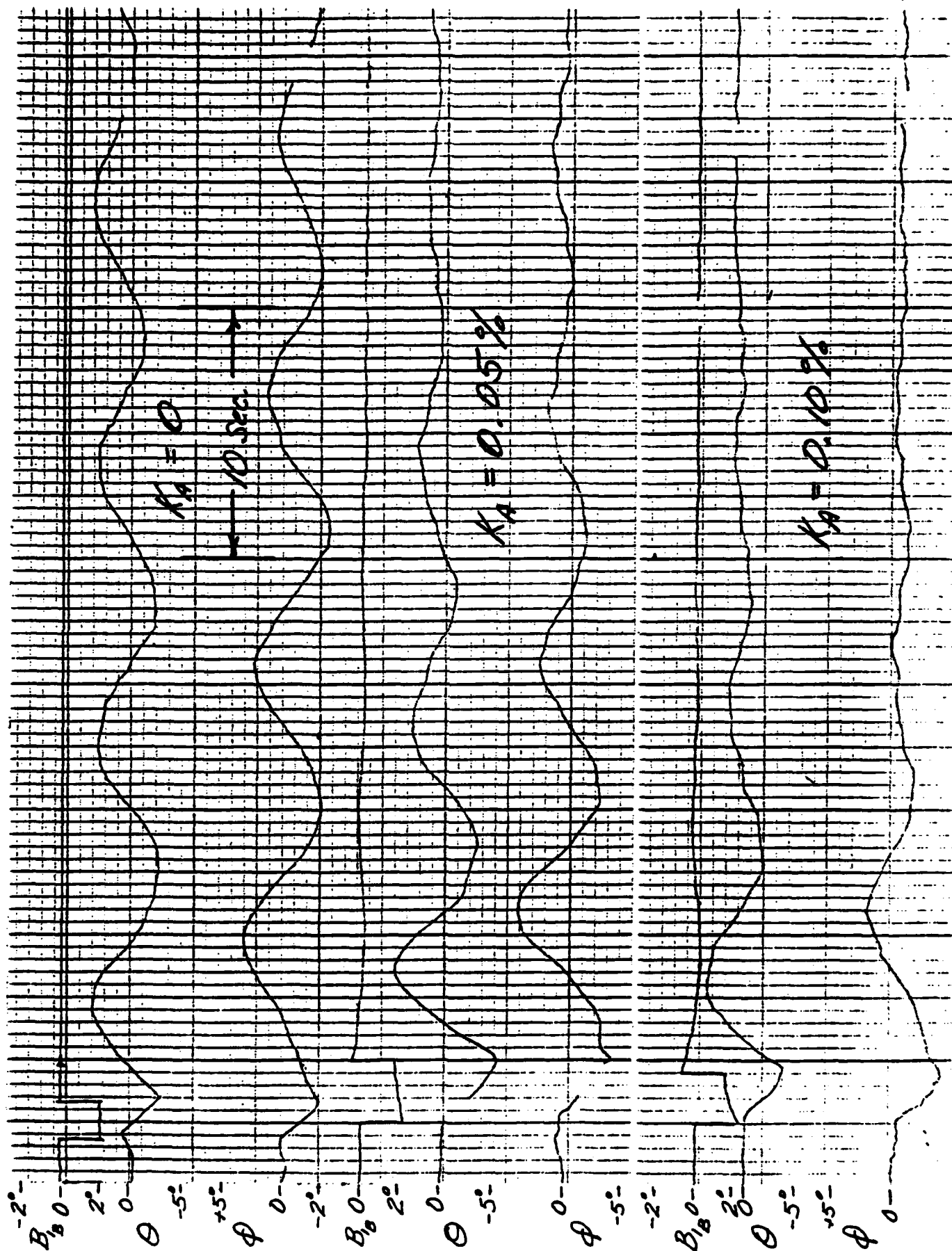


Figure A-4. Hovering Transient Responses, Run No. 17.

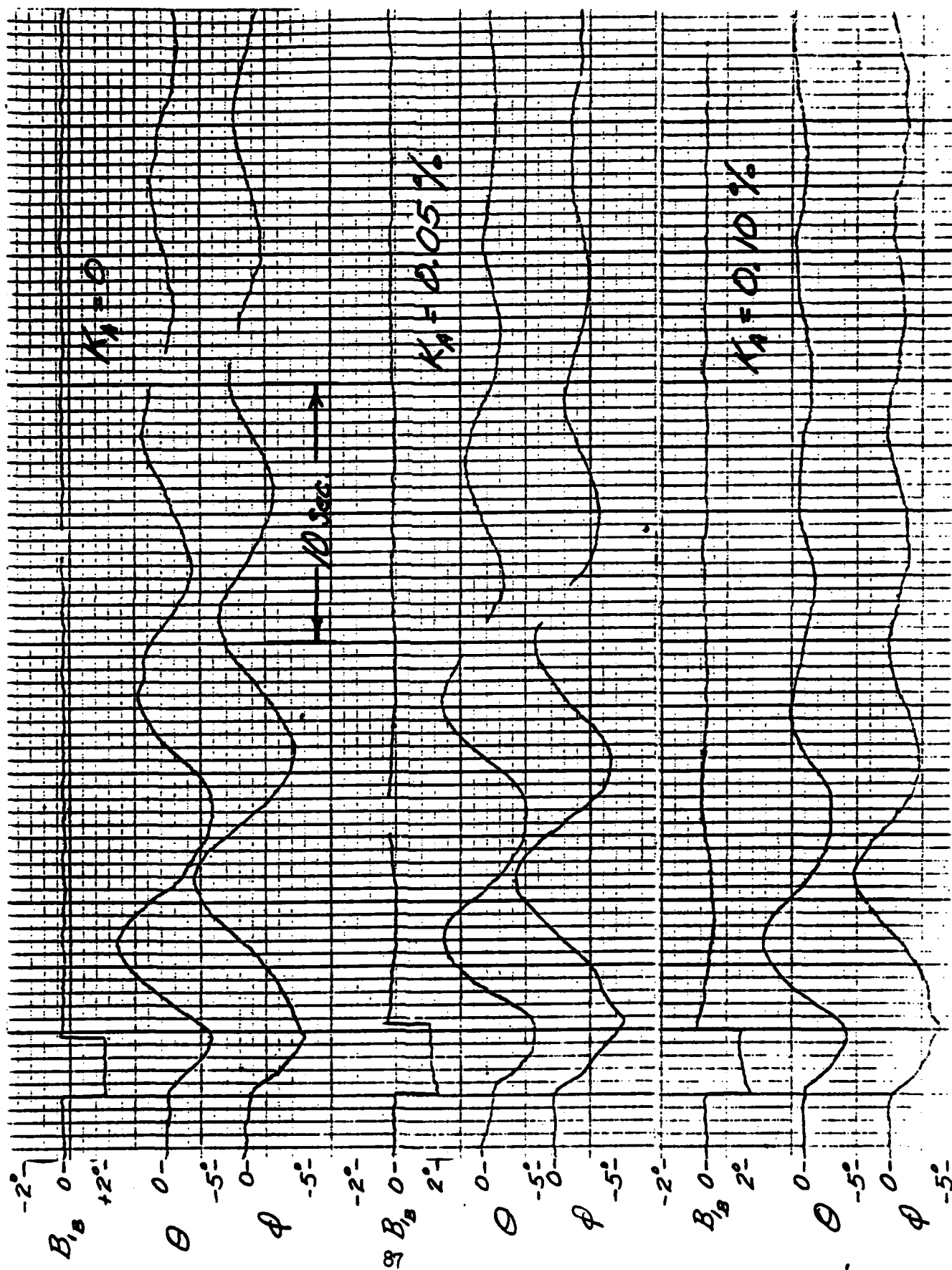


Figure A-5. Hovering Transient Responses, Run No. 36.

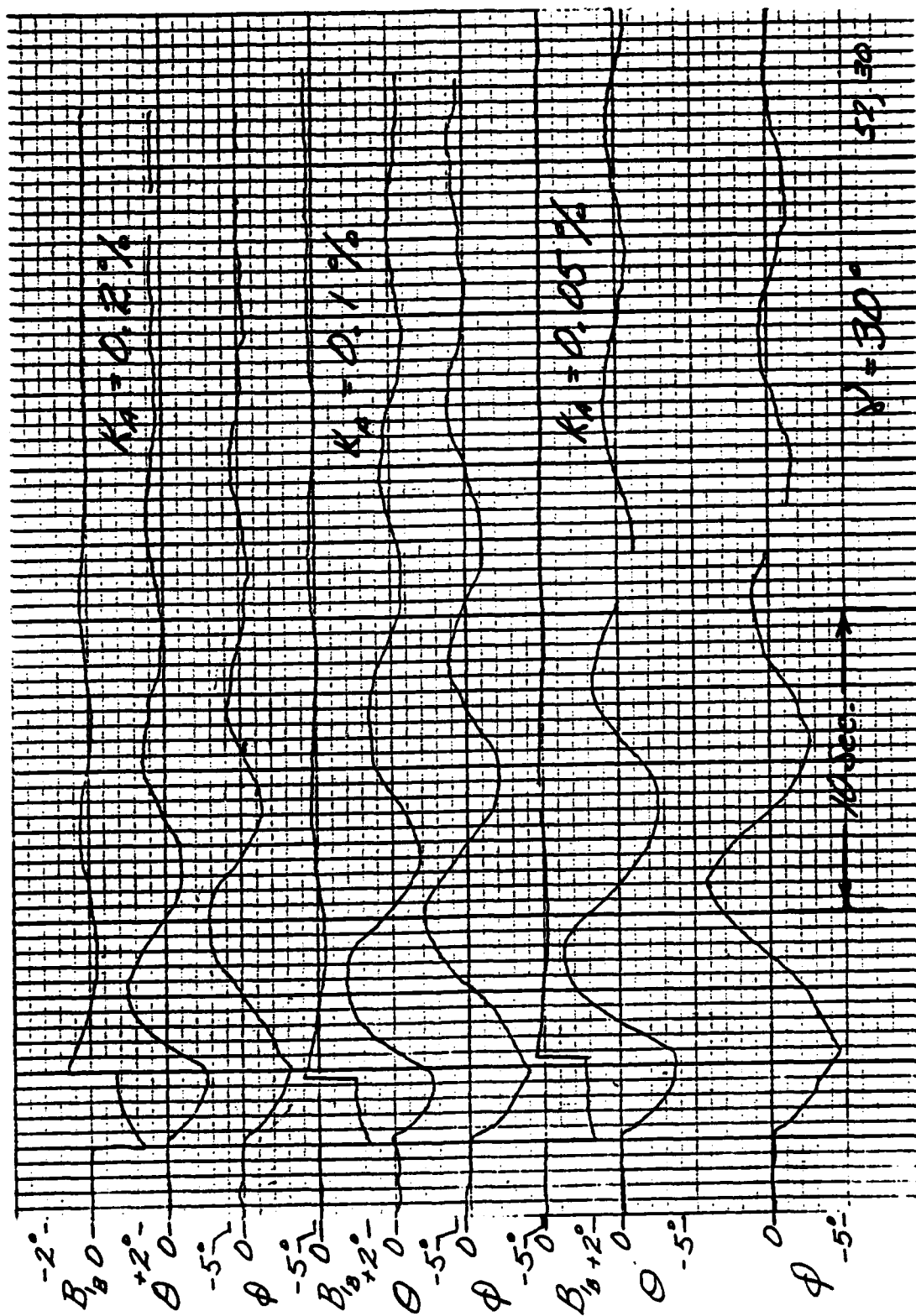


Figure A-6. Hovering Transient Responses, Run No. 52.

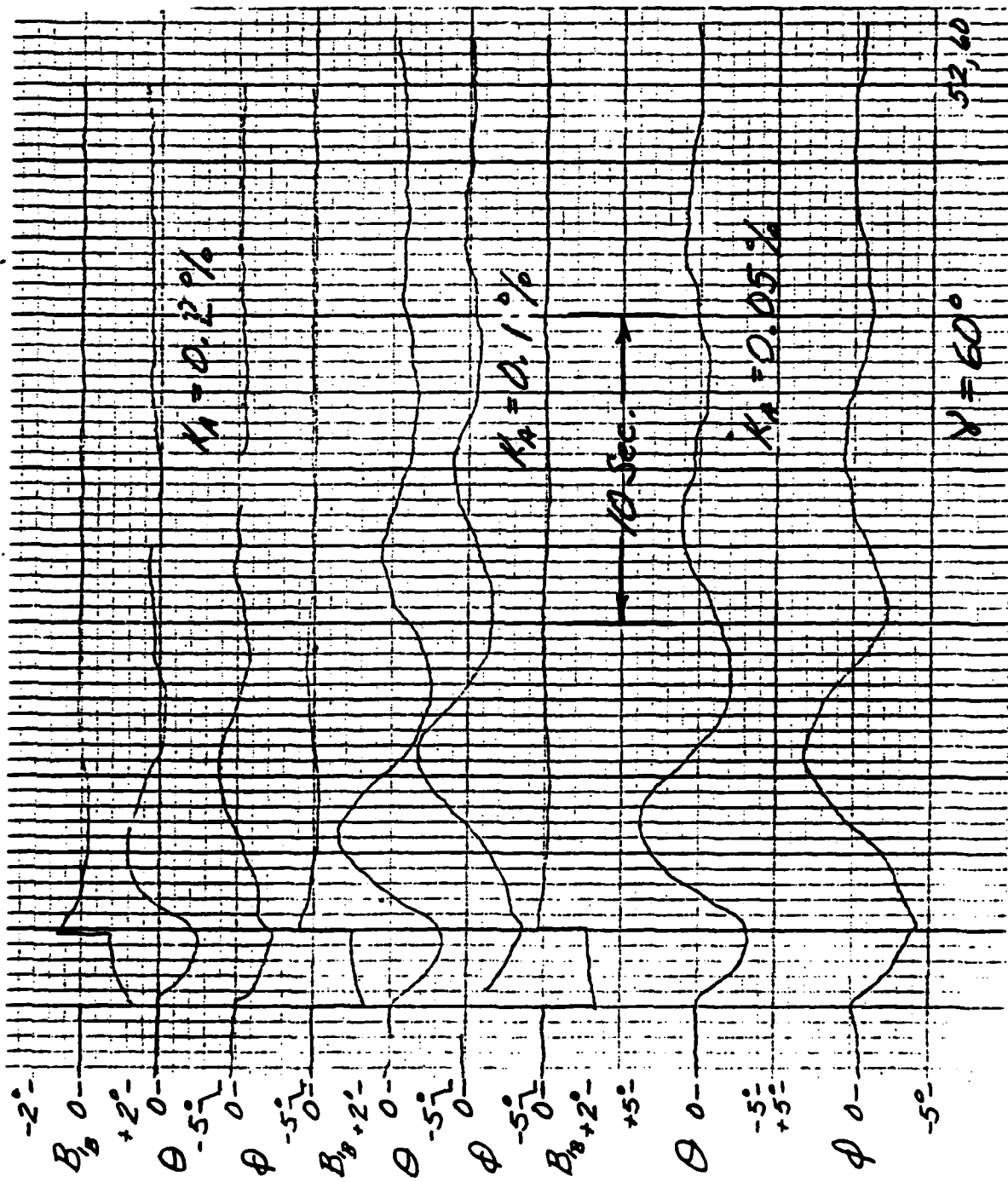


Figure A-6. Continued.

APPENDIX B

UMBILICAL CABLE CONTRIBUTIONS TO DYNAMIC STABILITY

The free-flight model of the AEROCRANE was equipped with an umbilical cable to provide power and control signals to the model and to carry data transducer signals to the ground recording instrumentation. The weight of this umbilical cable was of sufficient magnitude that its contributions to the dynamic stability of the vehicle must be included in the equations of motion. This section describes the manner in which the effects of the umbilical cable were incorporated in the equations. Only the hovering flight case is considered here.

Figure B-1 shows the configuration of the umbilical cable for hovering flight experiments. The shape of the umbilical cable is assumed to be a catenary. The lower end of the cable is in contact with the ground and assumed to remain fixed. The upper end of the cable is attached to the model and is assumed to move only in a horizontal plane. This latter assumption is consistent with the dynamic stability analysis which assumes that there is no vertical motion of the model during its transient motion.

The cable will add to the mass of the vehicle and will also produce forces and moments due to the tension in the catenary.

The effective mass of the cable is evaluated first. When the vehicle translates it will not carry the entire mass of the cable with it but rather will deform the cable into a new shape as shown in Figure B-1. It is assumed that there are no dynamics associated with the cable itself. That is, the motion of the cable is assumed to be quasi-static such that its shape is always that of a catenary. The effective mass of the cable can be determined by evaluating the kinetic energy of the cable as a function of the horizontal translation velocity of its upper end ($\Delta \dot{x}_0$).

Define the following quantities

m = running mass of cable

s = arc length of cable

x, y = horizontal and vertical coordinates to any point on the cable

$\phi(y)$ = mode shape of catenary, normalized by horizontal deflection of upper end of the cable.

Thus the equation describing the local horizontal translation of the cable is given by

$$\Delta x = \Delta x_0 \phi(y) \quad (B-1)$$

Differentiating this expression, the translational velocity of the cable, incorporating the quasi-static assumption that the shape of the cable is unaffected by motion, is given by

$$\Delta \dot{x} = \Delta \dot{x}_0 \phi(y)$$

the kinetic energy of the cable is therefore

$$KE = \frac{1}{2} m \int_0^s (\Delta \dot{x})^2 ds$$

or

$$KE = \frac{1}{2} m \Delta \dot{x}_0^2 \int_0^s \phi^2(y) ds \quad (B-2)$$

Evaluation of the integral will give the effective mass of the cable.

Now the equation for the perturbed shape of the catenary is developed such that the integral in the expression for the kinetic energy can be evaluated.

The equation of the catenary shape shown in Figure B-1 is given by

$$y = L_0 \left(\cosh \frac{x}{L_0} - 1 \right) \quad (B-3)$$

where

$$L_0 = \frac{H}{m}$$

and H = horizontal component of tension in catenary.

The assumption that the upper end of the cable moves only in a horizontal direction ($\Delta y = 0$) gives a relationship between a perturbation of the tension, H_0 (or L_0) and a perturbation of the upper end of the cable, Δx_0 . From equation (B-3)

$$\Delta y = 0 = \Delta L \left(\cosh \frac{x_0}{L_0} - 1 - \frac{x_0}{L_0} \sinh \frac{x_0}{L_0} \right) + \Delta x_0 \sinh \left[\frac{x_0}{L_0} \right] = 0 \quad (B-4)$$

Solving equation (B-3) for x

$$x = L_0 \cosh^{-1} \left[1 + \frac{y}{L_0} \right] \quad (B-5)$$

If the cable translates horizontally a small distance Δx equation (B-5) becomes

$$x + \Delta x = (L_0 + \Delta L) \cosh^{-1} \left[1 + \frac{y}{L_0 + \Delta L} \right] \quad (B-6)$$

Therefore subtracting equation (B-5) from (B-6)

$$\Delta x = (L_0 + \Delta L) \cosh^{-1} \left[1 + \frac{y}{L_0 + \Delta L} \right] - L_0 \cosh^{-1} \left[1 + \frac{y}{L_0} \right]$$

Assuming that the change in tension is small compared to the initial tension

$$\Delta x = \Delta L \left\{ \cosh^{-1} \left(1 + \frac{y}{L_0} \right) - \frac{\frac{y}{L_0}}{\sqrt{\left(\frac{y}{L_0} \right)^2 + 2 \frac{y}{L_0}}} \right\} \quad (B-7)$$

Equation (B-4) is used to eliminate ΔL from equation (B-7) so that an equation is obtained which relates the local horizontal translation of the

cable to the translation of the upper end,

$$\Delta x = \Delta x_0 \left\{ \frac{\sinh \frac{x_0}{L_0}}{\frac{x_0}{L_0} \sinh \frac{x_0}{L_0} + 1 - \cosh \frac{x_0}{L_0}} \right\} \cosh^{-1} \left(1 + \frac{y}{L_0} \right) - \frac{\frac{y}{L_0}}{\sqrt{\left(\frac{y}{L_0}\right)^2 + 2 \left(\frac{y}{L_0}\right)}} \quad (B-8)$$

Equation (B-8) thus gives the mode shape of the perturbed cable, that is, it is of the form given by equation (B-1) such that

$$\phi \left(\frac{y}{L_0} \right) = \left\{ \frac{\sinh \frac{x_0}{L_0}}{\frac{x_0}{L_0} \sinh \frac{x_0}{L_0} + 1 - \cosh \frac{x_0}{L_0}} \right\} \cosh^{-1} \left(1 + \frac{y}{L_0} \right) - \frac{\frac{y}{L_0}}{\sqrt{\left(\frac{y}{L_0}\right)^2 + 2 \left(\frac{y}{L_0}\right)}} \quad (B-9)$$

The first term in brackets is determined by the initial shape of the cable, i.e., by the horizontal distance between the end of the cable on the floor and the end of the cable attached to the model.

It is possible to find a simple approximation to equation (B-9). Figure B-2 shows that the second bracketed term in equation (B-9) is approximated very closely by

$$\frac{1}{\sqrt{2}} \sqrt{\frac{y}{L_0}} \approx \left\{ \cosh^{-1} \left(1 + \frac{y}{L_0} \right) - \frac{\frac{y}{L_0}}{\sqrt{\left(\frac{y}{L_0}\right)^2 + 2 \frac{y}{L_0}}} \right\} \quad (B-10)$$

Equation (B-9) can be further simplified by using the boundary condition at the upper end of the cable where from equation (B-1)

$$\phi\left(\frac{y_0}{L_0}\right) = 1$$

Therefore

$$\left\{ \frac{\frac{x_0}{L_0} \sinh \frac{x_0}{L_0} + 1 - \cosh \frac{x_0}{L_0}}{\sinh \frac{x_0}{L_0}} \right\} \sqrt{\frac{1}{\frac{y_0}{L_0}}} = \frac{1}{\sqrt{2}} \quad (B-11)$$

Thus the approximate mode shape is given by

$$\phi\left(\frac{y}{L_0}\right) = \frac{1}{\sqrt{\frac{y_0}{L_0}}} \sqrt{\frac{y}{L_0}} \quad (B-12)$$

Substituting equation (B-12) into (B-2), the expression for the kinetic energy becomes

$$KE = \frac{1}{2} m \Delta \dot{x}_0^2 \frac{L_0}{y_0} \int_0^s \frac{y}{L_0} ds \quad (B-13)$$

The arc length is given by the relationships for a catenary

$$s = L_0 \sinh \frac{x}{L_0} \quad (B-14)$$

Therefore using equations (B-3) and (B-14) can be integrated. The result can be expressed in terms of arc length as, noting that $m s_0 = m_c$, the total mass of the cable,

$$KE = \frac{1}{2} m_c \Delta \dot{x}_0^2 \left\{ \frac{-1 + \frac{1}{2} \left(\frac{\ln(\bar{s}_0 + \sqrt{1 + \bar{s}_0^2})}{\bar{s}_0} + \sqrt{1 + \bar{s}_0^2} \right)}{\sqrt{1 + \bar{s}_0^2} - 1} \right\} \quad (B-15)$$

where

$$\bar{s}_0 = \frac{s_0}{L_0}$$

L_0 , the ratio of the horizontal component of the tension to the running mass of the cable is found from the equation of the catenary (B-3) knowing the initial end points of the cable. For the various hovering experiments the typical height of the model (y_0) was 80 feet and the horizontal distance of the model from the point at which the cable left the ground was 25 feet (x_0). Substituting these values into equation (B-3) to determine L_0 and then using equation (B-14) it is found that,

$$\bar{s}_0 = 10.79$$

For values of \bar{s}_0 of this magnitude which were typical of all of the hovering experiments, equation (B-15) can be considerably simplified. For \bar{s}_0 greater than about 6 as shown in Figure B-2 a very good approximation to the term in brackets in equation (B-15) can be obtained and equation (B-15) can be approximated by

$$KE \approx \frac{1}{2} m_c \left\{ \frac{\frac{\bar{s}_0}{2} - 1}{\bar{s}_0 - 1} \right\} \Delta \dot{x}_0^2 \quad (B-16)$$

The effective mass of the catenary is therefore

$$m_{ce} \approx m_c \left\{ \frac{\frac{\bar{s}_0}{2} - 1}{\bar{s}_0 - 1} \right\} \quad (B-17)$$

and is approximately one-half the actual mass of the catenary. The value

one-half was used in the dynamic stability analysis since the cable mass is small relative to the mass of the vehicle, and a more refined treatment was not considered justified.

Consequently, the inertia effects of the cable are considered to be represented by a concentrated mass equal to one-half the actual mass of the cable supported (m_{ce}) located at the attachment point of the cable.

The contributions of the cable to the acceleration terms in the various equations of motion are

Horizontal Force

$$\Delta X_c = m_{ce} [\dot{u}_s + Z_A \ddot{\theta}]$$

Lateral Force

$$\Delta Y_c = m_{ce} [\dot{v}_s - Z_A \ddot{\phi}] \quad (B-18)$$

Pitching Moment

$$\Delta M_c = m_{ce} Z_A [\dot{u}_s + Z_A \ddot{\theta}]$$

Rolling Moment

$$\Delta L_c = m_{ce} Z_A [-\dot{v}_s + Z_A \ddot{\phi}]$$

The terms given by equations (B-18) are added to the dynamic stability equations to include the effect of cable inertia.

In addition to these acceleration effects the weight of the cable will produce forces and moments on the vehicle.

Figure B-3 shows the geometry involved in estimating the contributions of the cable weight to the equations of motion. It is assumed that the cable is straight when looking forward, as shown in the figure. The following notation is employed,

- T = tension in cable at attachment point
- β_x = initial slope of cable at attachment point
measured with respect to the vertical
- $\Delta\beta_x, \Delta\beta_y$ = perturbations in cable slope due to angular
rotation of model.

The equilibrium forces applied to the model due to cable tension will result in an initial pitch angle (θ_i) so that

$$\begin{aligned} X_c &= -T(\beta_x + \theta_i) \\ Y_c &= 0 \\ Z_c &= T \end{aligned} \tag{B-19}$$

The equilibrium moments due to cable tension are

$$\begin{aligned} M_c &= -T Z_A \beta_x \\ L_c &= 0 \end{aligned}$$

The perturbed forces and moments are

$$\begin{aligned} X_c + \Delta X_c &= -(T + \Delta T)(\theta_i + \theta + \beta_x + \Delta\beta_x) \\ Y_c + \Delta Y_c &= (T + \Delta T)(\phi + \Delta\beta_y) \\ M_c + \Delta M_c &= -(T + \Delta T) Z_A (\theta_i + \theta + \beta_x + \Delta\beta_x) \\ L_c + \Delta L_c &= -(T + \Delta T) Z_A (\phi + \Delta\beta_y) \end{aligned} \tag{B-20}$$

The slope of the cable can be found by differentiation of equation (B-3)

$$\frac{dy}{dx} = \sinh \frac{x}{L_0} \quad (B-21)$$

The equation of the catenary gives L_0 knowing the initial position of the cable, i.e., equation (B-3) is

$$y = L_0 \left(\cosh \frac{x}{L_0} - 1 \right) \quad (B-3)$$

Inserting typical values from the hovering experiments

$$x_0 = 25 \text{ ft}$$

$$y_0 = 80 \text{ ft}$$

Equation (B-3) gives

$$L_0 = 8.17 \text{ ft}$$

consequently

$$\frac{x_0}{L_0} = 3.07$$

$$\frac{y_0}{L_0} = 9.79$$

For these typical values the hyperbolic functions can be approximated by

$$\sinh \frac{x}{L_0} \approx \frac{1}{2} e^{\frac{x}{L_0}}$$

$$\cosh \frac{x}{L_0} \approx \frac{1}{2} e^{\frac{x}{L_0}}$$

therefore equations (B-21) and (B-3) can be approximated as

$$\frac{dy}{dx} \approx \frac{1}{2} e^{\frac{x}{L_0}} \quad (B-22)$$

$$y = L_0 \left(\frac{1}{2} e^{\frac{x}{L_0}} - 1 \right) \quad (B-23)$$

The slope given by equation (B-22) is related to the angle β_x by

$$\frac{dy}{dx} = \tan (90^\circ - \beta_x) \quad (B-24)$$

Since β_x is a small angle

$$\frac{dy}{dx} \approx \frac{1}{\beta_x}$$

From equation (B-23)

$$\beta_x \approx 2 e^{-\frac{x}{L_0}} \quad (B-25)$$

Now to find the rate of change of β_x with the movement of the end of the cable, equation (B-23) can be expressed in terms of β_x as

$$\frac{x}{y} \approx \left(\frac{\beta_x}{1 - \beta_x} \right) \ln \frac{2}{\beta_x} \quad (B-26)$$

Differentiating equation (B-26), the rate of change of β_x with x can be found. y is constant in the differentiation since it is assumed that the upper end of the cable translates horizontally only. The result is

$$\frac{d\beta_x}{dx} = \frac{1}{y_0} \left(\frac{(1 - \beta_x)^2}{\ln \frac{2}{\beta_x} - (1 - \beta_x)} \right) \quad (B-27)$$

Now from Figure B-3 it can be seen that

$$\Delta x = Z_A \Delta \theta$$

Therefore equation (B-27) can be written

$$\frac{d\beta_x}{d\theta} = \frac{Z_A}{y_0} \left(\frac{(1 - \beta_x)^2}{\ln \frac{2}{\beta_x} - (1 - \beta_x)} \right) \quad (B-28)$$

Expressed in terms of the initial horizontal position of the cable

$$\frac{d\beta_x}{d\theta} = \frac{Z_A}{x_0} \left(\frac{\beta_x (1 - \beta_x) \ln \frac{2}{\beta_x}}{\ln \frac{2}{\beta_x} - (1 - \beta_x)} \right) \quad (B-29)$$

Since β_x is assumed to be small this result may be further approximated by

$$\frac{d\beta_x}{d\theta} \approx \frac{Z_A}{x_0} \left(\frac{\beta_x \ln \frac{2}{\beta_x}}{\ln \frac{2}{\beta_x} - 1} \right) \quad (B-30)$$

Using typical values

$$x_0 = 25 \text{ ft}$$

$$Z_A = 9 \text{ ft}$$

$$y_0 = 80 \text{ ft}$$

$$L_0 = 8.17$$

Equation (B-25) gives β_x

$$\beta_x = 5.3^\circ$$

and equation (B-30) gives

$$\frac{d\beta_x}{d\theta} = 0.049$$

This rate of change of the cable angle with vehicle attitude will enter into the longitudinal equations of motion.

In the lateral case the analysis is considerably simpler since it is assumed that the cable is vertical in the initial condition. Therefore, the change in cable angle with roll is a result of the appearance of a component of the initial cable angle β_x in the lateral plane. Thus from Figure B-3

$$\Delta\beta_y = \beta_x \frac{Z_A \phi}{x_0}$$

or

$$\frac{d\beta_y}{d\phi} = \beta_x \frac{Z_A}{x_0} \quad (B-31)$$

For the typical case given above

$$\frac{d\beta_y}{d\phi} = 0.033$$

The variation in cable tension must now be evaluated. Since the cable tension must lie along the direction of the cable and the vertical component of cable tension is equal to the weight of the cable supported,

$$T = \frac{W_c}{\cos \beta_x}$$

Therefore

$$\frac{dT}{d\beta_x} = \frac{W_c}{\cos^2 \beta_x} \sin \beta_x \cong W_c \beta_x \quad (B-32)$$

and the initial tension in the cable, since β_x is a small angle is equal to the weight of the cable $T = W_c$.

Therefore equations (B-19) can be written as

$$\begin{aligned} X_c &= -W_c (\beta_x + \theta_i) \\ Y_c &= 0 \\ Z_c &= W_c \end{aligned} \quad (B-19)$$

The initial cable angle will produce a small inclination of the vehicle in hovering equilibrium. With a buoyant force, F_b , and a sling load weight W_s , the complete equation for x force equilibrium would indicate an initial pitch angle, i.e.,

$$(F_b - W_s) \theta_i - W_c (\theta_i + \beta_x) = 0$$

$$\theta_i = \frac{W_c \beta_x}{F_b - W_s - W_c}$$

Now the perturbation forces and moments can be evaluated by subtracting equations (B-19) from equation (B-20) where

$$\Delta \beta_x = \frac{d\beta_x}{d\theta} \theta \quad T = W_c$$

$$\Delta \beta_y = \frac{d\beta_y}{d\phi} \phi$$

$$\Delta T = \frac{dT}{d\beta_x} \frac{d\beta_x}{d\theta} \theta$$

The various derivatives are given by equations (B-30), (B-31) and (B-32).

Therefore

$$\Delta X_c = -W_c \left(1 + \frac{d\beta_x}{d\theta}\right) \theta - \frac{dT}{d\beta_x} \frac{d\beta_x}{d\theta} (\theta_i + \beta_x) \theta$$

$$\Delta Y_c = W_c \left(1 + \frac{d\beta_y}{d\phi}\right) \phi$$

(B-33)

$$\Delta M_c = -W_c Z_A \left(1 + \frac{d\beta_x}{d\theta}\right) \theta - z_A \frac{dT}{d\beta_x} \frac{d\beta_x}{d\theta} (\theta_i + \beta_x) \theta$$

(B-33 Con't)

$$\Delta L_c = -W_c Z_A \left(1 + \frac{d\beta_y}{d\phi}\right) \phi$$

Since $\frac{dT}{d\beta_x} \sim \beta_x$ and $\frac{d\beta_x}{d\theta} \sim \beta_x$ the second term in the horizontal force and pitching moment expressions is small and may be neglected.

Thus the cable weight contributions to the equations of motion are

$$\Delta X_c = -W_c \left(1 + \frac{d\beta_x}{d\theta}\right) \theta$$

$$\Delta Y_c = W_c \left(1 + \frac{d\beta_y}{d\phi}\right) \phi$$

(B-34)

$$\Delta M_c = -W_c Z_A \left(1 + \frac{d\beta_x}{d\theta}\right) \theta$$

$$\Delta L_c = -W_c Z_A \left(1 + \frac{d\beta_y}{d\phi}\right) \phi$$

where the cable angle derivatives are given by equation (B-30) and (B-31).

These terms given by equations (B-34) taken with the acceleration terms given by equation (B-18) thus constitute the cable contributions to the equations of motion.

Since for the typical hovering equilibrium the sample calculation presented above indicates that the derivatives $\frac{d\beta_x}{d\theta}$ and $\frac{d\beta_y}{d\phi}$ are small compared to 1 an average value equation to 0.04 was used for both of these derivatives in the dynamic stability analysis.

It may also be noted that the cable effects described in this section

give rise to position dependent forces, that is, a horizontal translation of the vehicle gives rise to a translational force from the umbilical cable.

The size of this effect may be estimated by calculating the translational frequency which would arise. That is for horizontal translation the equation of motion is

$$(m' + m_{ce}) \ddot{x} + W_c \frac{d\beta}{dx} x = 0 \quad (B-35)$$

where it has been assumed that the cable tension is equal to the weight of the cable. Thus the natural frequency arising from this effect is from equation (B-35)

$$\omega_x^2 = \frac{W_c}{(m' + m_{ce})} \frac{d\beta}{dx}$$

The the typical case described above

$$\frac{d\beta}{dx} = \frac{1}{Z_A} \frac{d\beta}{d\theta} = 0.0054$$

For the low center of gravity experiments,

$$m' = 9.13 \text{ slugs}$$

and a typical cable weight lifted is 50 lbs, giving

$$\omega_x = 0.165 \text{ rad/sec}$$

giving a period of 38 seconds which is considerably slower than the natural dynamics of the vehicle indicating that the effects are small and may be neglected.

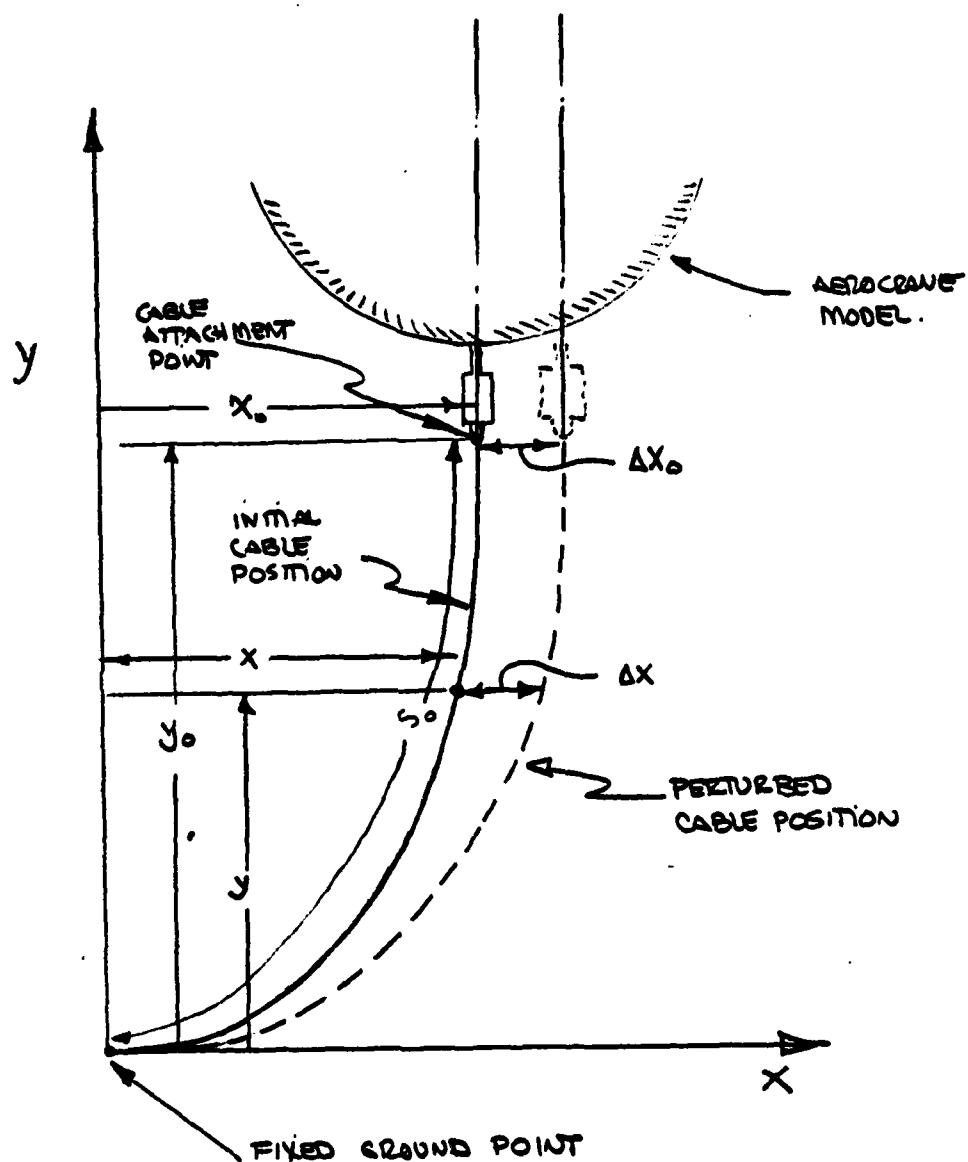
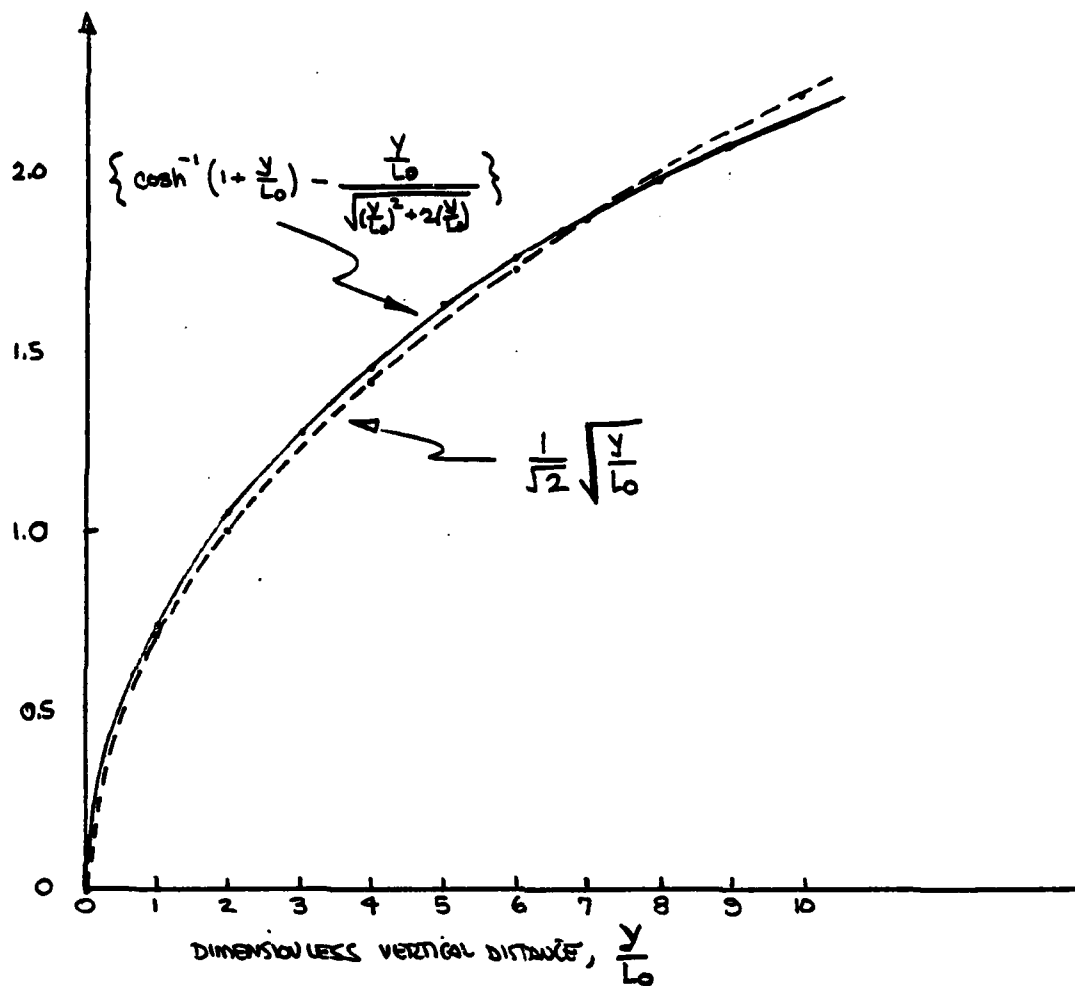


Figure B-1. Coordinates and Geometry for Cable Analysis.



COMPARISON OF EXACT AND APPROXIMATE PERTURBED MODE SHAPE

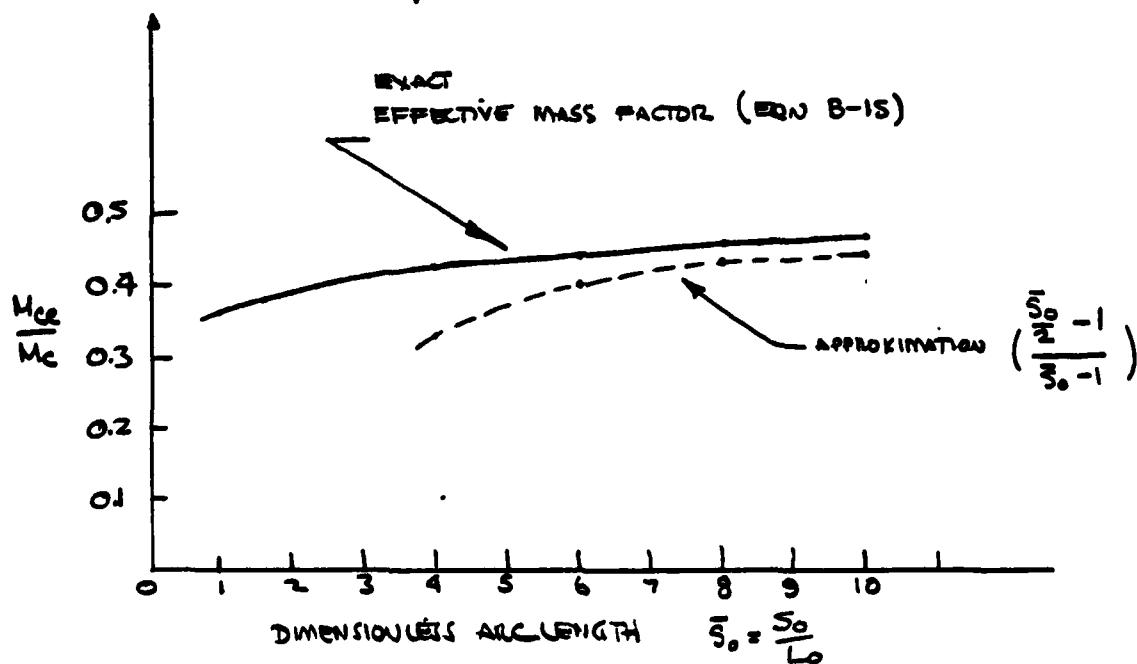


Figure B-2. Approximations Used in Cable Dynamics.

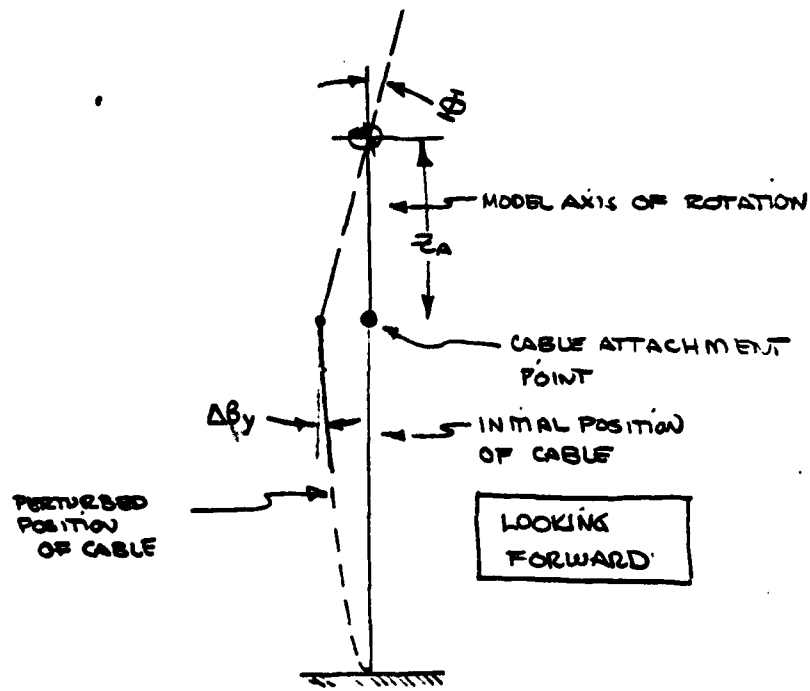
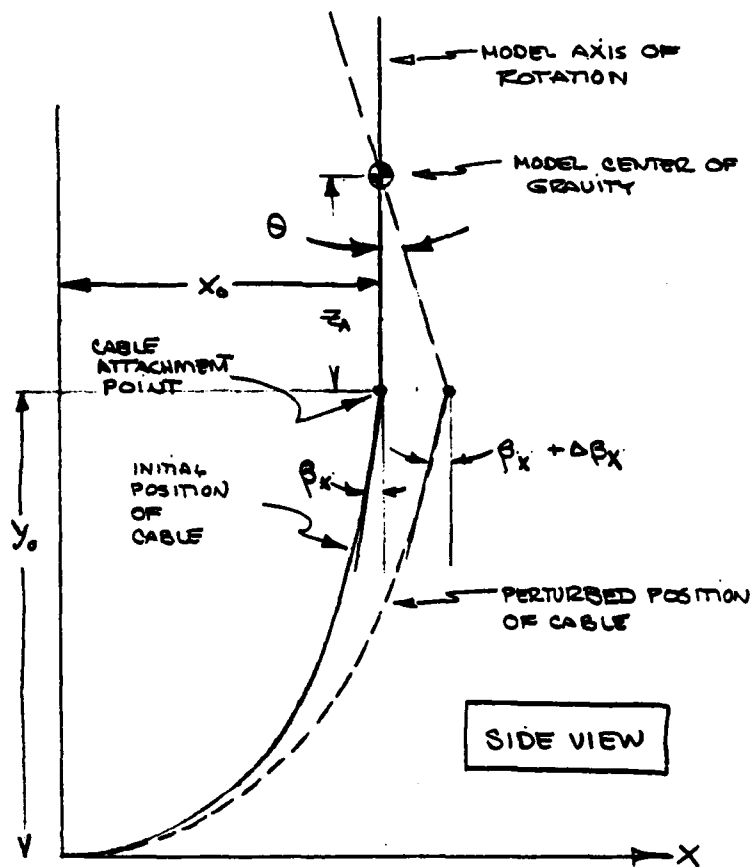


Figure B-3. Umbilical Cable Geometry in Hovering.

APPENDIX C

DETERMINATION OF AEROCRANE MODEL PHYSICAL PARAMETERS AND NUMERICAL RESULTS OF DYNAMIC STABILITY ANALYSIS

This section describes the manner in which the buoyant force and inertial properties of the AEROCRANE model were determined experimentally and also presents the numerical values employed in the stability analysis as well as the results. The calculated transient response characteristics based on the numerical values given here are discussed elsewhere in this report.

I.) Determination of Buoyant Force and Inertial Properties

Since the AEROCRANE model without sling load and umbilical cable possessed an excess of buoyancy, the following technique was used to determine the buoyant force. The sling load was placed on a scale with the model floating above supporting a length of umbilical cable, h_o . The scale reading is then related to the buoyant force by the following equation

$$[W_o + W_{sl} + 0.61 h_o] = S + F_b \quad (C-1)$$

where

W_o = weight of the basic model, lbs.

W_{sl} = weight of sling load, lbs.

S = scale reading, lbs.

F_b = buoyant force, lbs.

h_o = length of umbilical cable supported, ft.

The umbilical cable weighs 0.61 lbs. per ft. Table C-1 lists the values of the buoyant force for various hovering runs determined in this fashion. The aerodynamic thrust is determined from the equilibrium hovering altitude for the specific flight. That is,

$$T = (W_o + W_{sl} + 0.61 h_{eq}) - F_g \quad (C-2)$$

where T is the aerodynamic thrust and h_{eq} is the measured equilibrium altitude, and is also given in Table C-1. The values of thrust and buoyant force listed in Table II in the main body of this report were determined by the above technique.

The moment of inertia of the model in pitch (equal in roll) was determined measuring the natural frequency of the model oscillating in pitch with the rotor not rotating. A weight was added at the bottom of the model to increase the spacing between the center of buoyancy and the center of gravity. The separation of the center of buoyancy and the center of gravity provides a restoring moment and consequently produces a free motion which is oscillatory in character. The restoring moment characteristic was determined experimentally by hanging a weight at a blade root and measuring the angular deflection of the model corresponding to this applied moment. The equation of motion for the pitch oscillation is

$$I' \ddot{\theta} + M_\theta \theta = 0 \quad (C-3)$$

Consequently the natural frequency of the free motion is

$$\omega_n = \sqrt{\frac{M_\theta}{I'}}$$

The measured natural frequency, ω_n , and the restoring moment gradient, M_θ , measured as described above were used to determine the moment of inertia I' . Note that this procedure determines a moment of inertia which includes the influence of accelerating the air mass adjacent to the vehicle (apparent mass effects). The experimentally determined moment of inertia in pitch (equal to that in roll because of symmetry) is listed in Table C-1 as well. To obtain the configuration of runs 15 and 17 with a higher center of gravity position a fifteen pound weight was added at the upper pole of the spherical centerbody and this is reflected in an increased pitch inertia.

No direct measurement of the polar moment of inertia, I_z , is possible. Consequently this value was calculated based on knowing the size, weight, and location of all of the various components in the model. As a verification of this procedure the moment of inertia in pitch, I' , was also calculated from component contributions. The calculated value of I' was within one percent of the value determined from the oscillation tests and therefore the calculated value of I_z is assumed to be within one percent of the actual value.

Comparison of the calculated center of gravity position and the spacing between the center of gravity and center of buoyancy which can be determined from the measured restoring moment characteristics indicated that the center of buoyancy was 0.39 ft. above the plane of the rotor (the geometrical center of the centerbody if the centerbody is a perfect sphere) indicating a small distortion of the centerbody under load. This small distance was neglected in the analysis. That is, the center of buoyancy was assumed to lie in the plane of the rotor.

II.) Dynamic Stability Analysis

Using the various physical parameters of the model given in Table C-1 and the equations of motion presented in the main body of the report, the numerical values for the various coefficients in the equations of motion were calculated for runs 11, 15, 17 and 36. These values are presented in Figures C-1 through C-4. It should be noted that as can be seen by comparison of the numerical values of the elements of the damping and control matrices with the literal expressions given on pages 35 and 37 that the rotor inplane forces were neglected. Previous analyses have shown that these terms have only a minor effect on the dynamic stability and response characteristics in hover.

Table C-2 presents the eigenvalues calculated for these four hovering cases. Also presented are the corresponding period and damping ratio as well as an identification of each mode. The dynamic motion of the AEROCRANE model in hovering in the configuration flown is characterized by five oscillatory modes. Three of these modes are associated with the vehicle and two with the sling load. One of the basic modes of the vehicle is a fast motion that is well damped with a period of the order of 1.8 seconds and a damping ratio of the order of 0.5. This is basically an angular motion with its character determined primarily by the aerodynamic damping of the rotor and the gyroscopic moments. There is a lightly damped mode with a period of the order of 11 seconds and a damping ratio of 0.1 or less. This is the mode which dominates the measured transient response characteristics owing to its small damping ratio. As discussed in Reference 1, this mode may be described as a retrograde mode, that is, as a result of the polar symmetry of the vehicle this transient motion is in

fact a circling motion of the vehicle and in this mode the circling takes place opposite to the direction of rotor rotation. The remaining vehicle mode has a period of the order of 20 to 30 seconds and is well damped with a damping ratio of the order of 0.7. It can be characterized as an advancing mode as it corresponds to circling in the direction of rotor rotation. Owing to its large damping ratio the presence of this mode is not apparent in the measured or calculated transient responses. The remaining two modes are associated with the sling load motion in two directions. The period of these motion is of the order of 4 seconds and the damping ratios are very small as the sling load damping was neglected. The isolated sling load period is 4.69 seconds indicating that there is some coupling with the vehicle motion.

Comparison of the calculated transient response based on these numerical values with the experimentally measured transient response is discussed in the main body of the report.

TABLE C-1

PHYSICAL PARAMETERS OF AEROCRANE MODEL

RUN NO.	W_o lbs.	F_s lbs.	T lbs.	W_{sl} lbs.	W_c lbs.
11	177	210	89	67	55
36	177	201	64	51	37
15	192	206	52	20	46
17	192	199	84	42	49

RUN NO.	I' slug ft. ²	I_z slug ft. ²	r_o ft.	Z_A ft.	Z_{sl} ft.	Ω rad/sec
11	521	653	2.71	9.0	18	2.72
36	521	653	2.71	9.0	18	2.92
15	576	653	1.83	9.9	18	3.00
17	576	653	1.83	9.9	18	2.96

$m_A = 3.63$ slugs.

TABLE-C-2CALCULATED EIGENVALUES FOR HOVERING RUNSRUN NO. 11.

EIGENVALUES sec ⁻¹	PERIOD sec.	DAMPING RATIO	MODE
-2.275 ± 3.5751	1.76	0.536	FAST ANGULAR RESPONSE
-0.086 ± 0.6681	9.41	0.128	LIGHTLY DAMPED RETROGRADE
-0.248 ± 0.2721	23.10	0.674	WELL DAMPED ADVANCING
-0.035 ± 1.6151	3.89	0.022	SLING LOAD
-0.093 ± 1.4381	4.37	0.065	SLING LOAD

RUN NO. 15.

-2.096 ± 3.3711	1.86	0.528	FAST ANGULAR RESPONSE
-0.013 ± 0.4841	12.98	0.027	LIGHTLY DAMPED RETROGRADE
-0.208 ± 0.1931	32.55	0.733	WELL DAMPED ADVANCING
-0.004 ± 1.4111	4.45	0.003	SLING LOAD
-0.029 ± 1.3651	4.60	0.021	SLING LOAD

RUN NO. 17.

-2.300 ± 3.3441	1.88	0.567	FAST ANGULAR RESPONSE
-0.008 ± 0.5931	10.60	0.013	LIGHTLY DAMPED RETROGRADE
-0.244 ± 0.3311	18.98	0.594	WELL DAMPED ADVANCING
-0.013 ± 1.5041	4.18	0.009	SLING LOAD
-0.069 ± 1.4001	4.49	0.049	SLING LOAD

RUN NO. 36.

-2.361 ± 3.8341	1.64	0.524	FAST ANGULAR RESPONSE
-0.051 ± 0.5641	11.14	0.090	LIGHTLY DAMPED RETROGRADE
-0.229 ± 0.2101	29.90	0.737	WELL DAMPED ADVANCING
-0.015 ± 1.5381	4.08	0.010	SLING LOAD
-0.069 ± 1.4151	4.44	0.049	SLING LOAD

MASS MATRIX (M)

1.132	0	0	0	0	0.004
0	1.132	0	0	-0.004	0
1.5	0	1	0	0	-0.0555
0	1.5	0	1	0.0555	0
0	-0.235	0	0	1.094	0
0.235	0	0	0	0	1.094

DAMPING MATRIX (C)

3.13	3.409	0	0	-0.0579	0.159
-3.409	3.13	0	0	-0.159	-0.0579
0	0	0	0	0	0
0	0	0	0	0	0
0	0	0	0	0	0
0	0	0	0	0	0

SPRING MATRIX (K)

2.088	0	-1.157	0	0	0
0	2.088	0	-1.157	0	0
1.79	0	1.79	0	0	0
0	1.79	0	1.79	0	0
0	2.651	0	-7.34	0	0
-2.651	0	7.34	0	0	0

CONTROL MATRIX (F)

0	-8.52
8.52	0
0	0
0	0
0	0
0	0

Figure C-1: Numerical Values of Matrix Elements for Run No. 11.

MASS MATRIX (M)

1.13	0	0	0	0	-0.0016
0	1.13	0	0	0.0016	0
1.55	0	1	0	0	-0.0555
0	1.55	0	1	0.0555	0
0	0.096	0	0	1.079	0
-0.096	0	0	0	0	1.079

DAMPING MATRIX (C)

2.96	3.36	0	0	-0.048	0.151
-3.36	2.96	0	0	-0.151	-0.048
0	0	0	0	0	0
0	0	0	0	0	0
0	0	0	0	0	0
0	0	0	0	0	0

SPRING MATRIX (K)

1.474	0	-0.7218	0	0	0
0	1.474	0	-0.7218	0	0
1.79	0	1.79	0	0	0
0	1.79	0	1.79	0	0
0	4.58	0	-4.37	0	0
-4.58	0	4.37	0	0	0

CONTROL MATRIX (F)

0	-8.77
8.77	0
0	0
0	0
0	0
0	0

Figure C-2: Numerical Values of Matrix Elements for Run No. 17.

MASS MATRIX (M)

1.089	0	0	0	0	0.0088
0	1.089	0	0	-0.0088	0
1.5	0	1	0	0	-0.0555
0	1.5	0	1	0.0555	0
0	-0.5108	0	0	1.062	0
0.5108	0	0	0	0	1.062

DAMPING MATRIX (C)

3.03	3.66	0	0	-0.0379	0.1543
-3.66	3.03	0	0	-0.1543	-0.0379
0	0	0	0	0	0
0	0	0	0	0	0
0	0	0	0	0	0
0	0	0	0	0	0

SPRING MATRIX (K)

1.709	0	-0.881	0	0	0
0	1.709	0	-0.881	0	0
1.79	0	1.79	0	0	0
0	1.79	0	1.79	0	0
0	1.4	0	-5.59	0	0
-1.4	0	5.59	0	0	0

CONTROL MATRIX (F)

0	-8.82
8.82	0
0	0
0	0
0	0
0	0
0	0

Figure C-3: Numerical Values of Matrix Elements for Run No. 36.

MASS MATRIX (M)

1.121	0	0	0	0	-0.0007
0	1.121	0	0	0.0007	0
1.55	0	1	0	0	-0.0555
0	1.55	0	1	0.0555	0
0	0.0443	0	0	1.074	0
-0.0443	0	0	0	0	1.074

DAMPING MATRIX (C)

2.63	3.401	0	0	-0.0273	0.134
-3.401	2.63	0	0	-0.134	-0.0273
0	0	0	0	0	0
0	0	0	0	0	0
0	0	0	0	0	0
0	0	0	0	0	0

SPRING MATRIX (K)

1.476	0	-0.3437	0	0	0
0	1.476	0	-0.3437	0	0
1.79	0	1.79	0	0	0
0	1.79	0	1.79	0	0
0	3.09	0	-2.08	0	0
-3.09	0	2.08	0	0	0

CONTROL MATRIX (F)

0	-7.89
7.89	0
0	0
0	0
0	0
0	0

Figure C-4: Numerical Values of Matrix Elements for Run No. 15.

APPENDIX D

MODIFICATION OF TRIM EQUATIONS TO INCLUDE SLING LOAD AND UMBILICAL CABLE

The equations for equilibrium flight formulated in the text of the report do not include the sling load or the umbilical cable. These effects can be incorporated in the following fashion.

Since the aerodynamic forces on the sling load are negligible owing to the high density of the load and the low velocity of the experiments the equilibrium flight orientation of the sling load cable is vertical as can be seen from the steady-state solutions of the latter two of equations (65). Thus

$$\theta_L = -\theta$$

$$\phi_L = -\phi$$

Consequently, as seen from the first four of equations (65) the sling load adds to the weight in the two force equations and produces a moment about the center of gravity of the vehicle. If it is assumed that the angle that the umbilical cable makes with the vertical is negligible in forward flight, the umbilical also appears in the equilibrium equations in a similar fashion to the sling load, as may be seen from equations (67). The contributions of the umbilical from equation (67) and the sling load, from equation (65) to the force balance equations given by equation (8) are

horizontal force

$$(-m_L g - W_C) \sin \theta \cos \phi$$

side force

$$(m_L g + W_C) \sin \phi$$

vertical force

$$(m_l g + W_c) \cos \phi \cos \theta$$

Therefore for the force balance equations, to include the effects of the sling load and the umbilical cable, the term W may be interpreted as

$$W = W_o + m_l g + W_c$$

That is, it is the total weight supported by the buoyant force and aerodynamic thrust. This quantity W is referred to as the gross weight elsewhere in the report.

For inclusion in the moment equilibrium both of these weights act at their attachment point a distance Z_A below the center of gravity of the vehicle.

Thus to equations (13), the following terms must be added

pitch moment

$$Z_A [m_l g + W_c] \sin \theta \cos \phi$$

roll moment

$$-Z_A [m_l g + W_c] \sin \phi$$

Thus to summarize, to include the effects of the umbilical cable and the sling load in the trim calculations, the term W can be interpreted in the force balance equations (equation 8) as including the weight of the sling load and the umbilical cable. The moment equilibrium equations (equation 16) must be modified to include the above terms. The simpler form given by equation (18) can not be used.

DISTRIBUTION

Commander
Naval Air Systems Command
Washington, DC 20361
Attention: AIR-954 (1 copy)
AIR-03 (1 copy)
AIR-03P3 (1 copy)
AIR-03P32 (1 copy)
AIR-320 (1 copy)
AIR-5301 (1 copy)

Chief of Naval Operations
Department of the Navy
Washington, DC 20350
Attention: OP-987 (1 copy)
OP-506E (1 copy)

Commander
Naval Facilities Engineering Command
200 Stovall Street
Alexandria, VA 22332
Attention: NFAC-03 (4 copies)

Superintendent
Naval Postgraduate School
Monterey, CA 93940
Attention: Library (1 copy)

Commander
Naval Air Development Center
Warminster, PA 18974
Attention: Code 30P3 (15 copies)

Commander
David W. Taylor Naval Ship Research and
Development Center
Bethesda, MD 20034
Attention: Director, Aerodynamics Laboratory (1 copy)

Chief of Naval Research
800 North Quincy Street
Arlington, VA 22217
Attention: Mr. T. Wilson, Code 461 (1 copy)

Commander
Naval Weapons Center
China Lake, CA 93555
Attention: Aerodynamics Branch, Code 4061 (1 copy)

DISTRIBUTION: (Continued)

Commander
Air Force Flight Dynamics Laboratory
Air Force Systems Command
Wright-Patterson Air Force Base, OH 45433
Attention: Library (1 copy)

Commander
U. S. Army Aviation Systems Command
St. Louis, MO 63166
Attention: Library (1 copy)

Director
U. S. Army Air Mobility Research and Development Laboratory
Ames Research Center
Moffett Field, CA 94035
Attention: Library (1 copy)

Director
Eustis Directorate
U. S. Army Air Mobility Research and Development Laboratory
Fort Eustis, VA 23604
Attention: Library (1 copy)
Mr. Robert Smith (1 copy)

Director
Langley Research Center
National Aeronautics and Space Administration
Hampton, VA 23365
Attention: Library (1 copy)

Director
Ames Research Center
National Aeronautics and Space Administration
Moffett Field, CA 94035
Attention: Library (1 copy)
Dr. Mark Ardema (1 copy)

Director of Forest Products and Engineering Research
U. S. Department of Agriculture, Forest Service
Washington, DC 20250
(2 copies)

Secretary
Department of Transportation
400 7th Street, S.W.
Washington, DC 20590
Attention: Assistant for Aeronautical R&D (1 copy)

DISTRIBUTION: (Continued)

**Director
National Aeronautics and Space Administration
600 Independence Avenue
Washington, DC 20546
Attention: Director, Study and Analysis Office (1 copy)**

DDC (12 Copies)